Radiation dose measurement and prediction for linear slit scanning radiography

by
Benjamin Irving
IRVBEN001

SUBMITTED TO THE UNIVERSITY OF CAPE TOWN
In partial fulfilment of the requirements for the degree
MSc in Biomedical Engineering

Submitted on the 11 July 2008

Supervisors:
Dr Tania Douglas, Department of Human Biology, University of Cape Town
Professor Egbert Hering, Division of Medical Physics, Groote Schuur Hospital and University of Cape Town
Dr Gert Maree, Division of Medical Physics, Groote Schuur Hospital and University of Cape Town

Declaration

I, Benjamin John Irving, hereby declare that the work on which this dissertation is based is my original work (except where acknowledgements indicate otherwise) and that neither the whole work nor any part of it has been, is being, or is to be submitted for another degree at this or any other university.

I empower the university to reproduce for the purpose of research either the whole or any portion of the contents in any manner whatsoever.

Signature:

Signed by candidate

Date: 28/10/2008

Abstract

This study describes dose measurements made for linear slit scanning radiography (LSSR) and a dose prediction model that was developed for LSSR.

The measurement and calculation methods used for determining entrance dose and effective dose (E) in conventional X-ray imaging systems were verified for use with LSSR. Entrance dose and E were obtained for LSSR and compared to dose measurements on conventional radiography units. Entrance dose measurements were made using an ionisation chamber and dosemeter; E was calculated from these entrance dose measurements using a Monte Carlo simulator. Comparisons with data from around the world showed that for most examinations the doses obtained for LSSR were considerably lower than those of conventional radiography units for the same image quality. Reasons for the low dose obtained with LSSR include scatter reduction and the beam geometry of LSSR. These results have been published as two papers in international peer reviewed journals.

A new method to calculate entrance dose and effective dose for LSSR is described in the second part of this report. This method generates the energy spectrum for a particular set of technique factors, simulates a filter through which the beam is attenuated and then calculates entrance dose directly from this energy spectrum. The energy spectrum is then combined with previously generated organ energy absorption data for a standard sized patient to calculate effective dose to a standard sized patient. Energy imparted for different patient thicknesses can then be used to adjust the effective dose to a patient of any size. This method is performed for a large number of slit beams moving across the body in order to more effectively simulate LSSR. This also allows examinations with technique factors that vary for different parts of the anatomy to be simulated. This method was tested against measured data and Monte Carlo simulations. This model was shown to be accurate, while being specifically suited to LSSR and being considerably faster than Monte Carlo simulations.

Acknowledgements

Dr Tania Douglas, University of Cape Town, for her guidance, support and in depth reviews.

Prof Egbert Hering and Dr Gerrie Maree, Division of Medical Physics, Groote Schuur Hospital, for their advice and support with the many different dose measurements and for helping source all equipment needed.

Stef Steiner, Dr Herman Potgieter and Carlos de Sousa, Lodox Systems, for their advice, direction and explanation of the Statscan system.

Prof Kit Vaughan for his guidance, advice and inspiration on completing academic research and his advice during the Lodox meetings.

Gillian Swart, Department of Health, for providing me with access to medical physics resources available to her department and from her Masters dissertation.

Khalid Hussein, University of Cape Town, for his advice regarding image quality quantification and analysis.

Michael Evans, consultant to African Medical Imaging, for his advice on linking measuring equipment to a computer.

Prof Walter Huda, Medical University of South Carolina, for his advice on developing an effective dose prediction programme and his review of the current concepts.

Dr M Tapiovaara, Radiation and Nuclear Safety Authority Finland (STUK), for providing organ mass data used in the Monte Carlo simulator PCXMC.

Virginia Saunders, Lodox Systems, and Dr Peter Gresak, consultant to African Medical Imaging, for their anatomical and medical advice in the development of a prediction programme.

The Biomedical Engineering students for providing another perspective on difficult problems.

Contents

1 Introduction **16**
1.1 Background 16
1.2 Motivation and aims 17

2 Literature review **20**
2.1 Radiation 20
2.1.1 Introduction to electromagnetic radiation and its effects 20
2.1.2 The interaction of ionising radiation with matter 22
2.1.3 Creation and propagation of X-ray radiation 23
2.1.4 Definitions of measurement 27
2.2 Dose measurement 29
2.2.1 Equipment 29
2.2.2 Entrance dose measurement 31
2.2.3 Effective dose measurement 31
2.3 Dose Calculation 32
2.3.1 Entrance dose calculation 32
2.3.2 Effective dose calculation 34
2.4 Slit scanning radiography 35

3 Dose measurement: materials and verification **38**
3.1 Materials 38
3.1.1 PCXMC 38
3.1.2 Ionisation chamber 39
3.1.3 Radiography Units 41
3.2 Verification of methods 42
3.2.1 Verification of the dosemeter 42
3.2.2 Verification that PCXMC can be applied to LSSR 47

4 Dose measurement: measurements for paediatric and adult patients **49**
4.1 Paediatric Patients 50
4.1.1 Method 50

4.1.2 Results . . . 51
4.2 Adult patients . . . 58
4.2.1 Method . . . 58
4.2.2 Results . . . 58

5 Dose measurement: analysis **62**
5.1 Discussion of paediatric doses . . . 62
5.2 Discussion of adult doses . . . 64
5.3 Development of reasons for low doses . . . 66
5.3.1 Further derivation of geometrical reasons for low dose . . . 68

6 LSSR dose prediction: method **73**
6.1 Entrance dose modelling . . . 73
6.1.1 Entrance dose method 1: Spectrum generation model . . . 74
6.1.2 Entrance dose Method 2: Polynomial exposure fit model . . . 75
6.2 Effective dose modelling . . . 76
6.2.1 Introduction to key concepts used in the model . . . 76
6.2.2 Method of dose prediction for LSSR including ATFC . . . 83

7 LSSR dose prediction: model verification and results **88**
7.1 Comparison between entrance dose models . . . 88
7.2 Incremental effective dose comparison . . . 93
7.3 Effective dose as a function of beam energy . . . 97
7.4 Additional results . . . 99
7.4.1 Standard examinations . . . 99
7.4.2 Automatic Technique Factor Correction (ATFC) . . . 104
7.5 Advantages of the model and comparison with a similar model . . . 107
7.6 Summary and discussion . . . 109

8 Conclusion **110**

A Additional entrance dose measurements **118**

B Ionisation Chamber Documents **120**
B.1 Partial volume exposure of Radcal ionisation chambers . . . 120
B.2 PTW Ionisation chamber communication . . . 122

C Dose comparison data **124**
C.1 Entrance dose comparison data . . . 124
C.2 Effective dose comparative data . . . 126

D Code explanation **130**
D.1 Files 130
D.2 Running the programme 132

Glossary

Absorbed Dose in Air - D_A
The energy transferred from ionising radiation to air per unit mass of air.

Anode
Current flows into the anode of a device; in the X-ray tube the electrons travel from the cathode to the anode.

Antero-posterior Projection - AP
A projection with the X-ray beam passing from the front of the patient to the back.

Automatic Technique Factor Correction - ATFC
Modification of the technique factors as a slit scan progresses in order to optimise the beam for the anatomy of each region of the body.

Cathode
Current flows out of the cathode of a device; in the X-ray tube electrons travel from the cathode to the anode.

Characteristic Radiation
Local peaks in the energy spectrum due to interactions between electrons emitted from the cathode and the electrons in the atoms of the anode.

Compton Scattering
A mechanism by which part of the energy of a photon is transferred to an electron in the atom, removing the electron from the atom.

Computed Tomography - CT
Acquiring three dimensional image information using X-ray radiation.

Coulomb - C
SI derived unit of charge.

Detective Quantum Efficiency - DQE
A measure of detector performance.

Dose-area Product - DAP
Entrance surface dose multiplied by the cross sectional area exposed by the beam.

Effective Dose - E
The weighted average of the dose to each organ.

Effective DQE
A measure of system performance.

Electron Volt - eV
Unit of energy where $1\text{eV} = 1.602 \times 10^{-19}$ J.

Entrance Dose "free-in-air"
Dose in air at the patient surface excluding backscatter.

Entrance Surface Dose - ESD
Dose in air at the patient surface including backscatter.

Exposure - X
Amount of charge per unit mass produced by ionising radiation in air.

Focus-to-collimator Distance - FCD
The distance from the X-ray focal spot to the collimator.

Focus-to-skin Distance - FSD
The distance from the X-ray focal spot to the surface of the patient.

Gray - Gy
Unit of dose where 1 Gy= 1 J/kg.

Half Value Layer - HVL
The thickness of a specific material that will attenuate the intensity of the beam by half.

Hertz - Hz
SI derived unit of frequency.

International Committee for Radiological Protection - ICRP
An international advisory body on radiation protection.

Ionisation Chamber
A chamber used to measure exposure and dose.

Ionising Radiation
Electromagnetic radiation with enough energy to ionise atoms.

Joules - J
SI derived unit of energy.

Lateral Projection -
A projection where the X-ray beam passes through the side of the patient.

Monte Carlo Simulations
Used in medical physics applications to simulate the path of electrons, photons or other particles through the body during treatment or diagnosics; used to estimate risk.

PCXMC
A commercially available Monte Carlo simulator for calculation of effective dose from X-ray examinations.

Photoelectric Effect
A mechanism by which all the energy from a photon is transferred to an electron in an atom.

Photon
A quantum/particle of electromagnetic radiation.

Roentgen - R
Unit of exposure where $1\text{R} = 2.58 \times 10^{-4}$ C/ kg.

Scatter fraction
The fraction of signal detected from scattered X-rays.

Scatter-to-primary ratio - SPR
The ratio between the detected signal from scattered X-rays and primary X-rays.

Sievert - Sv
Unit of effective dose and equivalent dose where 1 Sv =1 J/kg.

Statscan
A commercially available linear slit scanning X-ray machine.

Technique Factors
Parameters that can be changed to optimise the X-ray image quality.

Thermoluminesent Dosemeters - TLDs
Crystals energised by radiation and used to measure dose.

Tube Current - mA
The current from to the flow of electrons from the cathode to the anode of the X-ray tube, typically measured in mA.

Tube Voltage - kV
The potential difference between the cathode and the anode of the X-ray tube, typically measured in kV.

Volt - V
SI derived unit of electric potential.

X-ray Spectrum
The flux of photons of each energy in the X-ray beam.

X-rays
High energy electromagnetic radiation derived from interactions outside the atomic nucleaus.

List of Figures

1.1 An X-ray image obtained using the Statscan linear slit scanning X-ray machine. 18

2.1 A simplified diagram of the X-ray tube. 24
2.2 The X-ray spectrum at 100kV and 200mA with 1mmAl filtration and 5mmAl filtration. 25
2.3 A simplified diagram of an ionisation chamber. 30
2.4 Diagram showing the difference in geometry between slit scanning and linear slit scanning radiography units for the same entrance area. . . . 36

3.1 A fitted polynomial showing the relationship between the chamber reading and the dose. 40
3.2 Statscan linear slit scanning X-ray machine. 41
3.3 The two chambers above a phantom. 44
3.4 The two chamber set up for the conventional X-ray machine. 44

4.1 Effective doses from the Statscan (minimum and maximum from the measurements obtained at both hospitals) and the Shimadzu units for common radiographic examinations. 57
4.2 Using the ionisation chamber to measure the dose at the detector. . . 59

5.1 The X-ray beam geometry and exposed volume in conventional radiography and LSSR for the same exposed entrance area. 70
5.2 The difference in X-ray beam geometry between conventional full field radiography (where the beam width increases with distance) and LSSR in the scanning direction. 70

6.1 The energy absorption coefficients for the lung as a function of photon energy and position. 80
6.2 A demonstration of the beam slice approach to modelling LSSR, where one of the slices is highlighted. 84

6.3 Energy absorption curve $\eta(\varepsilon)$ for a particular slice; the curve for the patient of interest is a weighted average of the Boone curves shown in the diagram. 85
6.4 The energy absorbed per photon bin in an example slice and the energy entering the slice per photon bin. 86
6.5 A flow diagram of the programme design for dose prediction. 87

7.1 Comparison between measured data and results of Method 1. 90
7.2 Comparison between measured data and results of Method 2. 91
7.3 Comparison between measured data and results of Method 3. 92
7.4 Effective dose per increment generated by PCXMC and the new model for the AP projection of a standard sized patient. 95
7.5 Effective dose per increment generated by PCXMC and the new model for the lateral projection of a standard sized patient. 95
7.6 Effective dose per increment generated by PCXMC and the new model for the AP projection of a patient of mass 7kg and height 75 cm. . . . 96
7.7 Effective dose per increment generated by PCXMC and the new model for the AP projection for a patient of mass 130kg and height 200 cm. 96
7.8 Effective dose calculated using PCXMC and the new model for different regions of the body, as a function of tube voltage for medium sized patients. 98
7.9 The energy spectrum for a tube voltage of 100kV, a tube current of 200mA, a slit width of 0.4mm, a scan speed of 70mm/s and an FSD of 98cm. 100
7.10 View 1 of the dose to each organ per slice simulated for a tube voltage of 100kV, a tube current of 200mA, a slit width of 0.4mm, a scan speed of 70mm/s and an FSD of 98cm. 101
7.11 View 2 of the dose to each organ per slice simulated for a tube voltage of 100kV, a tube current of 200mA, a slit width of 0.4mm, a scan speed of 70mm/s and an FSD of 98cm. 102
7.12 The effective dose for each slice of the examination for a tube voltage of 100kV, a tube current of 200mA, a slit width of 0.4mm, a scan speed of 70mm/s and an FSD of 98cm. 103
7.13 The energy spectrum of the beam for each slice of the examination for a tube current of 200mA, a slit width of 0.4mm, a scan speed of 70mm/s, an FSD of 98cm and a tube voltage ranging from 120kV to 48kV. 105
7.14 The entrance dose (free-in-air) and the dose-area product through the examination for a tube current of 200mA, a slit width of 0.4mm, a scan speed of 70mm/s, an FSD of 98cm and a tube voltage ranging from 120kV to 48kV. 105

7.15 The dose to each organ per slice simulated for a tube current of 200mA, a slit width of 0.4mm, a scan speed of 70mm/s, an FSD of 98cm and a tube voltage ranging from 120kV to 48kV. 106
7.16 The effective dose for each step of the ATFC examination for a tube current of 200mA, a slit width of 0.4mm, a scan speed of 70mm/s, an FSD of 98cm and a tube voltage ranging from 120kV to 48kV. 107

D.1 The position of each increment and positions of common landmarks . 133

List of Tables

2.1 ICRP (1991) weighting factors for each organ. 29

3.1 Radiation measurements on Siemens conventional X-ray machine for calibration of CT chamber. 45
3.2 *ESD* measurements on Lodox Statscan with CT chamber parallel to the scanning direction (FSD = 84cm). 46
3.3 *ESD* measurements on Lodox Statscan with CT chamber perpendicular to the scanning direction (FSD = 84cm). 46
3.4 Differences in effective dose between full field and iterative approach for common examinations. 48

4.1 Standard paediatric patient sizes. 50
4.2 Entrance dose and effective dose for particular scans on the Lodox Statscan Unit at Groote Schuur Hospital (Measurements were obtained by the author of this disseration and by E Hering and G Maree). . . . 53
4.3 Entrance dose and effective dose for particular scans on Lodox Statscan at Red Cross Children's Hospital (Measurements were obtained by G Maree and E Hering). 54
4.4 Entrance dose and effective dose for particular scans on CR at Red Cross Children's Hospital (Measurements were obtained by G Maree and E Hering). 55
4.5 Comparison between effective dose (μSv) from Lodox Statscan, CR and other pediatric studies from around the world. 56
4.6 Effective Doses from Lodox Statscan and Fuji CR for the Standard Trauma Imaging Protocol at Red Cross Children's Hospital. 56
4.7 2007 Statscan doses for medium-sized patients. 60
4.8 2007 Statscan doses for extra large patients. 61
4.9 Comparison of 2007 Statscan effective doses (μSv) with those from other studies. 61

5.1 Verification of 1/r rule for LSSR. 68

6.1 PCXMC organ masses for a standard patient. 81

A.1 Entrance dose measurements recorded in 2006 for all patient sizes. . . 119

C.1 Comparison between measured and predicted entrance dose for various examinations. 125

C.2 Effective dose (mSv) for each 1cm increment generated for PCXMC and the model developed in this study. 126

1 Introduction

1.1 Background

X-rays were discovered by Wilhelm Roentgen by accident when he was looking at the properties of cathode rays. The publication of his observations and the now famous image of the bones in his wife's hand started a craze in which X-ray machines were being created by scientists and laypersons across the world. Even coin operated X-ray machines were installed where interested people could insert a coin and examine the bones in their hand. There was no thought to the risk from X-ray radiation at the time, although certain people reported burns after being exposed for long periods of time (Kevles, 1997).

Later the link between radiation and cancer was firmly established. It was found that the risk of cancer is proportional to the amount of radiation exposure and certain organs are more likely to develop cancer when exposed to radiation than others (Ron, 2002). Therefore, measures were introduced to quantify the amount of radiation to which a patient is exposed. Effective dose is a particularly useful measure of risk because it takes into account the sensitivity of each organ to radiation (ICRP, 1991).

The radiation dose is often still not given enough attention when performing an examination. Slovis (2002) argues that the risks from the radiation dose are often not fully understood by radiologists or justified in terms of the image quality. It is, however, important to have a good understanding of the patient dose for each examination in

order to determine whether the scan is worth the risk or whether the dose should be reduced. Slovis (2002) also points out the responsibility of manufactures to try and lower dose while maintaining image quality, and to explain to radiologists how dose and image quality can be optimised on their system.

1.2 Motivation and aims

Lodox Systems (Johannesburg) have developed a linear slit scanning X-ray machine known as Statscan; an image acquired by Statscan is shown in Figure 1.1. Unlike conventional X-ray systems where the area of interest is exposed at once, Statscan uses a thin fan beam that travels across the patient during the examination. Statscan was designed with the intention of offering a lower dose than conventional radiography without compromising image quality.

The Statscan system is used primarily in trauma imaging. Thorough evaluation of the dose delivered by the system would allow comparisons with other X-ray imaging technologies and would highlight applications other than trauma for which this and other slit scanning systems could be adapted. Due to the newness of linear slit scanning technology, the suitability of methods used to measure dose in older X-ray imaging systems for use in LSSR has not been determined. These methods include the use of ionisation chambers and Monte Carlo simulators.

The aims of the first part of the project reported on here, were (1) verification of the suitability of available dose measurement methods for LSSR; (2) comparison of the dose delivered by Lodox Statscan to that delivered by other x-ray imaging systems; and (3) further development of the reasons for dose differences between LSSR and conventional X-ray machines.

The aim of the second part of the project was to develop a model to estimate the entrance dose and effective dose that a particular patient would receive during a specific examination using LSSR. This model was developed as a software programme that Lodox Systems will be able to incorporate into the Statscan product. The advantages of such a programme over the earlier dose calculations for standard examinations are that no tube output measurements are required to calculate the dose, the speed of calculation is greatly increased and the accuracy is increased because the programme was designed to simulate the geometry of the beam more accurately than currently available Monte Carlo simulators.

Figure 1.1: An X-ray image obtained using the Statscan linear slit scanning X-ray machine.

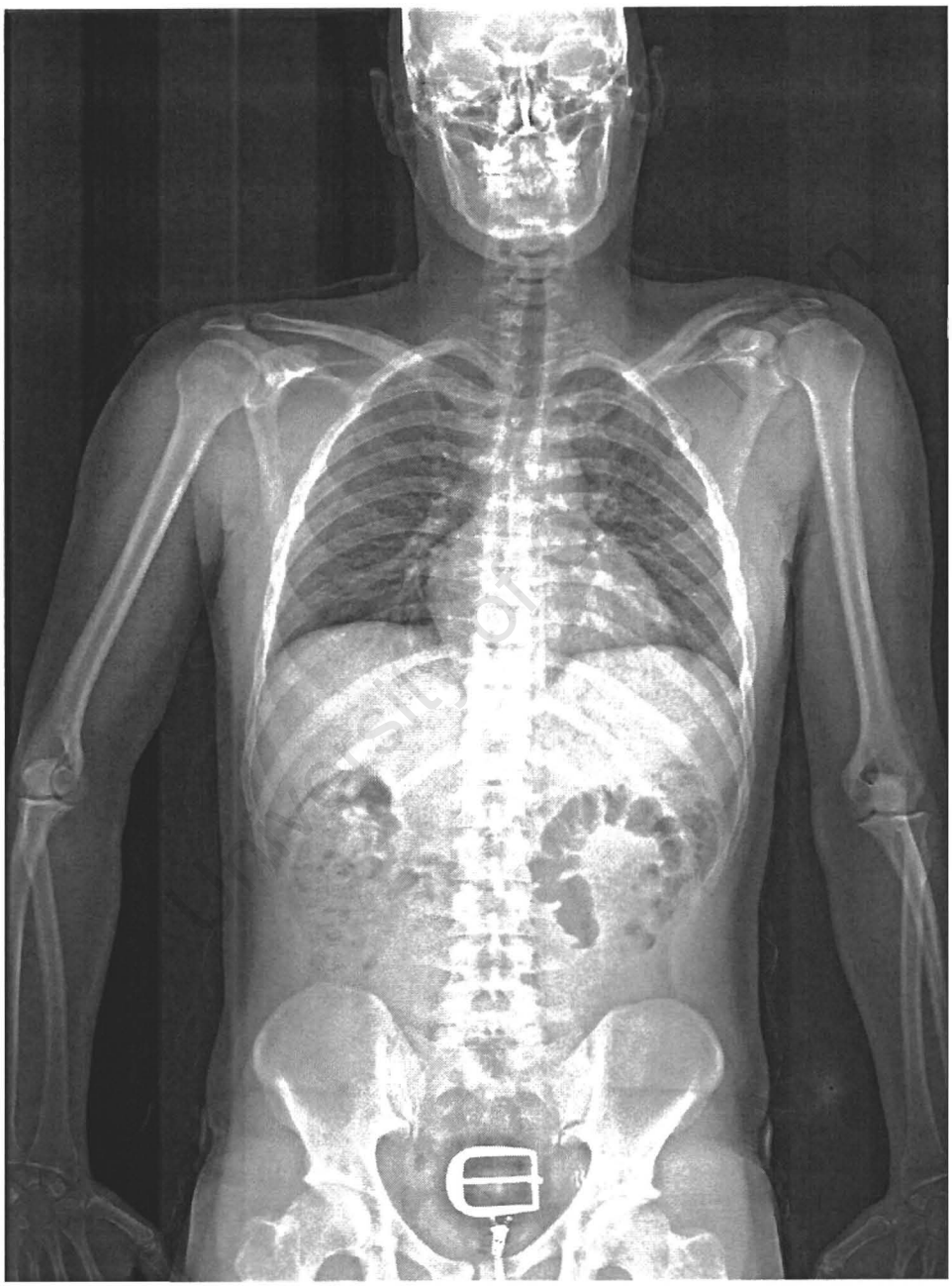

This model has been designed to divide the beam into a large number of slices and calculate each slice individually. The added advantage of such a method is that it can be used to simulate automatic technique factor correction (ATFC), which is a scan that involves adjusting the X-ray beam spectrum for each region of the body in order to optimise the image quality as the thickness and density of the patient changes. ATFC is possible because of the scanning property of linear slit scanning X-ray machines.

This report discusses the various aspects of the research. Chapter 2 outlines previous research that has contributed to the work completed in this project. The basic concepts of dose measurement and prediction are defined, including the physics of X-ray radiation, previous methods used in measurement and calculation of dose, and the concept of slit scanning radiography. Chapter 3 discusses the materials used to obtain the dose measurements and verifies that these materials can be used with LSSR. Chapter 4 outlines the methods used to measure entrance dose and calculate effective dose for standard examinations using LSSR for adult and paediatric examinations. The doses obtained are shown in this chapter and compared to other world wide studies. Chapter 5 discusses the doses obtained for adult and paediatric patients and places these doses in perspective in terms of image quality. The reasons for the dose difference between LSSR and conventional radiography are further developed in this chapter. Chapter 6 outlines a model that can be used to estimate doses for examinations using LSSR, and compares different methods that can be used as elements of this model. Chapter 7 compares the results generated from this model to the entrance doses measured in Chapter 4 and effective doses generated using a Monte Carlo program. Other useful results generated by the model are also shown in this chapter including equivalent dose for each organ and effective dose as a function of position.

The following papers on the work described in this report have been published in peer reviewed journals: *Irving B, Maree G, Hering E and Douglas T. Radiation dose from a linear slit scanning X-ray machine with full body imaging capabilities. Rad. Prot. Dosim. 2008; (in press)* and *Maree G, Irving B, and Hering E. Paediatric dose measurement in a full-body digital radiography unit. Ped. Radiol. 2007; 37:990-997.*

2 Literature review

2.1 Radiation

2.1.1 Introduction to electromagnetic radiation and its effects

Electromagnetic radiation has many different forms, from low frequency radio waves to visible light, and at high frequencies, X-ray and gamma rays (Dendy and Heaton, 1987; Pollack and Stump, 2001). Electromagnetic radiation has particle and wave properties, and a single particle is known as a photon. The frequency of the radiation is directly proportional to the energy carried in the radiation; the relationship between the energy (J) of a photon and frequency (Hz) is (Dendy and Heaton, 1987; Pollack and Stump, 2001)

$$\varepsilon = h\nu \tag{2.1}$$

where h is the Planck constant $h = 6.626 \times 10^{-34}$ J.s. ε is used to denote photon energy so that it can be differentiated from effective dose (E).

Useful units that can be used to describe energy are electron volts (eV) instead of joules (J) where $1\text{eV} = 1.602 \times 10^{-19}\text{J}$. 1 eV is the amount of kinetic energy an electron gains when accelerated through a potential difference of one volt (V), because $\text{KE} = q_e V$ where KE is the kinetic energy measured in joules (J) and $q_e = 1.602 \times 10^{-19}$ C is the charge of an electron (Pollack and Stump, 2001).

Gamma radiation generally has a higher energy than X-rays but X-ray and gamma radiation are defined over the same electromagnetic frequency range. They are named differently only because they were found under different circumstances. These terms are now used to define the source of the radiation, where X-ray radiation is from interactions outside the nucleus and gamma radiation is from nuclear reactions (Dendy and Heaton, 1987). X-ray and gamma radiation are in the frequency range of $10^{17} - 10^{22}$ Hz compared to visible light which is between 3.9×10^{14} Hz and 7.6×10^{14} Hz (Pollack and Stump, 2001). It is the high energy of X-ray and gamma rays that make them harmful to the body.

Ionising radiation has a detrimental effect on the human body because it imparts energy to atoms in the body, causing ionisation. This can lead to changes to the structure of molecules in cells which can affect the functioning of the cell. The most important effects are caused by damage to the DNA, which can lead to cell death or mutation (ICRP, 1991).

The effects of ionising radiation can be divided into two categories, namely deterministic effects and stochastic effects (ICRP, 1991). Deterministic effects occur when large quantities of cells are destroyed and affect the functioning of that tissue. Below a certain threshold this effect is negligible. Stochastic effects occur when the cells are modified by the ionising radiation. These cells are at risk of becoming cancerous or causing genetic effects, where genetic mutations are passed on to offspring (Hering, 1995; ICRP, 1991).

Sensitivity to radiation is not uniform in the body. Different organs and tissues have varying degrees of sensitivity. The lungs for example are more sensitive to radiation than the liver, leading to a higher risk of the lungs developing cancer from radiation (ICRP, 1991, 2008; Ron, 2002). Radiation dose is accumulative, so two examinations carry the same risk as one examination with the effective dose of the combined examinations (Ron, 2002).

The most commonly accepted view is that there is a linear relationship between the effective dose and the risk of cancers developing (ICRP, 1991; Ron, 2002). The linear relationship between risk and radiation exposure can be used to calculate the number of fatal malignancies from radiation. Okkalides and Fotakis (1994) calculated

the average radiation exposure to patients undergoing radiographic examinations, estimating that 6.8 million people per year undergo radiographic examinations in Greece. They calculated that roughly 300 patients per year in Greece developed fatal malignancies as a result of radiographic exposures. The estimation of deaths from low dose ionising radiation is now considered inaccurate because of the large uncertainties in the link between low dose radiation and cancer (Martin, 2007). The linear relationship view is challenged by research that indicates that there is a threshold, below which there is no effect from the radiation (Nussbaum, 1998). Other research suggests that the linear relationship is an underestimate of the risk at low doses (Nussbaum, 1998). Nussbaum (1998) argues that no matter the shape of the relationship between dose and risk, the current standards are not adequate to protect the public and that stricter measures must be put in place.

The difficulty in determining the exact relationship between risk and radiation dose is due to the complexity of measuring the risks. These risks are small and only become significant when considering a whole population (Okkalides and Fotakis, 1994). The effects of ionising radiation are also generally only apparent much later in life, making it difficult determine if the cause was ionising radiation exposure. Epidemiological studies attempt to compute the risk from ionising radiation. These studies are usually based on atom bomb survivors or patients that have been exposed to medical radiation sources (Ron, 2002). Studies using medically irradiated patients have the advantage that a good estimate can be made of the radiation that the patient was exposed to, but the disadvantage that underlying disease could influence the sensitivity to radiation (Ron, 2002).

Radiation does not only have man made sources. In fact, most of the radiation exposure to an average person comes from natural sources such as radon; less than 20% of the radiation exposure is artificial. Medical imaging, however, constitutes the largest artificial source (Ron, 2002; Watson et al., 2005).

2.1.2 The interaction of ionising radiation with matter

Photons at energies used in diagnostic radiology undergo two main interactions where energy is deposited in a material, namely the photoelectric effect and Compton scattering (Dendy and Heaton, 1987).

2.1.2.1 The photoelectric effect

The photoelectric effect involves the removal of an electron from an atom by the radiation. A photon from the X-ray beam transfers all of its energy to an electron in the inner shell of the atom. This energy is partly used to overcome the binding energy

and the remainder is converted to kinetic energy of the electron. The vacancy in the shell that is created is then filled by one of the electrons from a higher energy shell. This results in the release of a photon which has an energy equal to the difference between the energy of the two shells (Dendy and Heaton, 1987; Hering, 1995; Khan, 1994).

The probability of an interaction by the photoelectric effect decreases with increasing photon energy. There is, however, increased probability when the photon energy is just larger than the binding energy of particular shells (Khan, 1994).

2.1.2.2 Compton scattering

The Compton effect involves the interaction between a photon and an electron that is essentially free i.e. the binding energy is small compared to the energy of the photon (Khan, 1994). Unlike in the photoelectric effect where all the energy is transferred from the photon to the electron, only part of the energy is transferred and the photon is scattered. The photon loses energy in this interaction and, therefore, the frequency of the photon decreases.

This process is described by the following equation (Dendy and Heaton, 1987)

$$\Delta\varepsilon = \frac{\varepsilon^2}{m_e c^2}(1 - \cos\phi) \tag{2.2}$$

where $\Delta\varepsilon$ is the change in energy of the photon, ε is the original energy of the photon and ϕ is the angle by which the photon is scattered.

The photons and electrons released in photoelectric and Compton interactions will go on to interact with other atoms. Eventually, through a number of interactions, the energy deposited in the material will be converted to heat. Therefore, the photoelectric effect and Compton scattering result in attenuation of the X-ray beam as energy is transferred from the beam to the material it is passing through (Dendy and Heaton, 1987; Hering, 1995).

2.1.3 Creation and propagation of X-ray radiation

2.1.3.1 The X-ray tube

The X-ray tube is made up of an anode and a cathode with a large applied potential difference. Electrons hit the anode causing the emission of photons (See Figure 2.1) (Dendy and Heaton, 1987; Khan, 1994).

Figure 2.1: A simplified diagram of the X-ray tube.

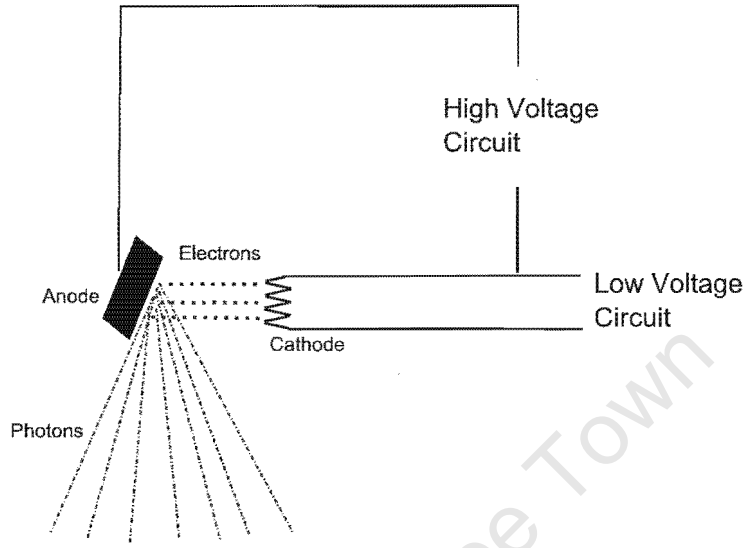

The cathode is generally made from a tungsten filament. Tungsten is used because it has a very high melting point of 3370°C. A high current (typically 6A) flows through the "low voltage circuit" (see Figure 2.1). This causes the filament to heat up and release electrons by thermionic emission. The electrons are accelerated by the potential between the anode and the cathode, and then hit the anode (Dendy and Heaton, 1987; Khan, 1994).

The atoms of the anode interact with the incoming electrons to produce the photon beam. The anode is generally made of tungsten which is chosen again because of its high melting point. During the production of X-rays most of the energy from the electrons is transferred as heat onto the anode. The efficiency of the tube in producing X-rays increases with tube voltage, but is very low. At 100kV the efficiency is less than 1%, which means that the rest of the energy is released as heat into the anode. Thus, heat removal is an essential feature of the anode. One method of heat removal is to use a rotating anode, which means that the target area is continuously being changed so that the heat is spread over a larger area. The focal spot size (i.e. the size of the area that interacts with the electron beam), is also important. The larger the spot the better the heat distribution but a larger focal spot can lead to poorer spatial resolution in the image. Changing the size of the focal spot will not affect the flux of electrons and, therefore, will not have a considerable effect on the photon flux (Dendy and Heaton, 1987; Khan, 1994).

2.1.3.2 Emission spectrum

The high energy electrons released from the cathode interact with the atomic nuclei and electron shells in the anode. The negatively charged electrons are attracted to the positively charged nuclei by the Coulombic force, which bends the electron path, accelerating the electron. Accelerated charges emit radiation and for a high enough acceleration this emitted radiation will be in the X-ray region. This interaction is known as *Bremsstrahlung* and results in an energy spectrum that has the highest flux for low energy photons and decreases linearly as the photon energy increases. The characteristic shape of the X-ray spectrum (see Figure 2.2), however, is due to much higher attenuation of the lower energies in the tube and to characteristic radiation. (Dendy and Heaton, 1987; Khan, 1994)

Figure 2.2: The X-ray spectrum at 100kV and 200mA with 1mmAl filtration and 5mmAl filtration.

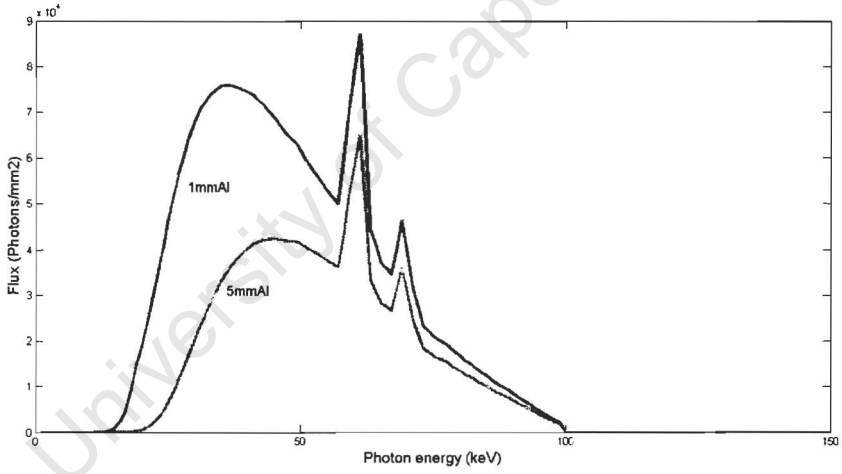

The shape of the spectrum is not a smooth curve and there are local peaks due to characteristic radiation. Characteristic radiation is caused by some of the incoming electrons knocking out electrons from particular bands in the atoms of the anode. This causes electrons from higher bands to fill the vacancy, which results in photons being emitted that are equivalent to the energy difference between the two bands, in a similar way to the photoelectric effect (Dendy and Heaton, 1987; Khan, 1994).

2.1.3.3 Technique Factors

Technique factors can be adjusted for each examination and patient size to optimise the image quality for that examination. The tube voltage and the tube current (often referred to by their units kV and mA respectively) are the technique factors that are used to modify the tube output directly. The tube voltage is the potential difference between the anode and the cathode. Increasing the tube voltage causes greater electron acceleration and leads to photons of a higher mean energy being produced. The tube current is the current caused by the flow of electrons from the cathode to the anode. The tube current is increased by increasing the current in the cathode filament (the low voltage circuit in Figure 2.1). This leads to greater heating of the filament and a higher rate of electron emission. Increasing the tube current leads to more electrons being produced and therefore a higher photon flux. The tube current, however, does not affect the shape of the energy spectrum. (Dendy and Heaton, 1987; Hering, 1995; Khan, 1994)

2.1.3.4 Attenuation

Once the X-ray radiation passes out of the tube it is attenuated by a filter placed under the beam's path. This is used to shape the beam by removing more lower energy photons than higher energy photons.

The attenuation is dependent on the energy of the photons and the particular type of material used as a filter, for example Statscan uses a 1 mm aluminium filter (Lodox, 2006). Photons passing through a material have a certain probability of interaction with the material. Assuming that if a photon interacts it will be either be absorbed or scattered away, the reduction in photons is proportional to the number of photons in the beam. Therefore, a monochromatic X-ray beam attenuates exponentially by the following equation (Khan, 1994):

$$I = I_0 e^{-\mu x} = I_0 e^{-(\frac{\mu}{\rho})\rho x} \tag{2.3}$$

where μ is the linear attenuation coefficient and x is the filter thickness. This coefficient is dependent on the density (ρ) of the material. Therefore, $(\frac{\mu}{\rho})$ is independent of density and is known as the mass attenuation coefficient. The attenuation of an energy spectrum can be calculated by applying this equation separately to defined photon energy bins which has its own attenuation coefficient (Beutel et al., 2000, pg 49). In this study, bins of width 1 keV were chosen and photons falling into a particular bin were simulated with the same attenuation coefficient.

2.1.4 Definitions of measurement

2.1.4.1 Half Value Layer

The half value layer (HVL) is defined as the thickness of a material that will attenuate the intensity of the beam by half. When considering a monochromatic beam, the intensity of the beam attenuates by

$$I = I_0 e^{-\mu x} \tag{2.4}$$

where μ is the linear attenuation coefficient for the material for a specific beam energy, and x is the thickness of the material (Dendy and Heaton, 1987; Khan, 1994).

Therefore, the HVL is related to μ by

$$HVL = \frac{\ln 2}{\mu} \tag{2.5}$$

for monochromatic spectra. For polychromatic spectra the HVL can be measured in terms of energy fluence (energy per unit area), photon fluence (number of photons per unit area) or exposure. The choice of parameter must be given because it affects the result. Exposure is most commonly used to measure HVL (Khan, 1994).

2.1.4.2 Absorbed dose in air

The absorbed dose in air (D_A) is the amount of energy that is transferred from ionising radiation to air per unit volume via interactions with the atoms in the air. This is measured in units of Gray (Gy) where 1Gy=1J/kg (Hering, 1995).

Entrance dose (free in air) is the D_A at the entrance surface distance without backscatter, where backscatter is scattered radiation from the object being exposed to radiation. Entrance surface dose (ESD) includes backscatter in the measurement (Gogas et al., 2003). Dose-area product (DAP) is ESD multiplied by the exposed cross-sectional area. DAP is a useful quantity in radiography because it is related to the flux of the beam and is therefore constant at any distance from the X-ray source (Yakoumakis et al., 2001).

2.1.4.3 Exposure

As discussed in Section 2.1.2, ionising radiation ionises atoms and results in the creation of negatively and positively charged ions. Exposure (X) is defined as the total

amount of charge per unit mass that is produced by the interaction of the ionising radiation with a volume of air and is measured in C/kg or the older unit roentgen (R) where 1R = 2.58×10^{-4} C/kg. This includes electrons produced by secondary reactions. An example of a secondary reaction is in Compton scattering where the released electron has enough energy to ionise other atoms. These secondary electrons need to be included in any measurement (Dendy and Heaton, 1987; Hering, 1995).

D_A can be estimated from the charge imparted. Empirically it has been found that the conversion is:

$$\mathrm{D_A(Gy)} = 0.00876\ \mathrm{X(R)} \tag{2.6}$$

$$= 0.00876/2.58 \times 10^{-4} = 34\ \mathrm{X(C/kg)} \tag{2.7}$$

where D_A is the dose in air in Gray and X is the exposure in either roentgen (R) or (C/kg) (Beutel et al., 2000; Khan, 1994). What this formula means is that on average it takes 34 joules of energy to create one Coulomb of charge in air.

2.1.4.4 Effective dose

Effective dose (E), as defined by the ICRP (1991), is the weighted average of the equivalent dose to each organ

$$E = \sum_T w_T H_T \tag{2.8}$$

where the equivalent dose (H_T) in the case of photons is the average dose absorbed in a particular organ or tissue, and the tissue weighting factor (w_T) reflects the sensitivity of each organ to radiation (w_T are shown in Table 2.1) (ICRP, 1991). The unit of measurement used for both E and H_T is the Sievert (Sv) where 1Sv = 1J/kg. E is used as an indicator of risk. From epidemiological studies a risk factor of a fatal cancer developing has been estimated in terms of E to be 0.05/Sv (ICRP, 1991). There are, however, large uncertainties in the relationship between risk and E. Martin (2007) reports that the actual risk could be higher or lower by a factor of 5 for an individual. The ICRP (1991) recommends a maximum exposure of 1mSv per year for the general public. This limitation does not include necessary medical procedures. The ICRP has recently published new recommendations (ICRP, 2008) which includes modifications to the w_T that have been used in this report including a change of w_T for the gonads from 0.2 to 0.08, and the addition of extra organs to the calculation of E.

Table 2.1: ICRP (1991) weighting factors for each organ.

Ovaries	0.20
Testes	0.20
Active bone marrow	0.12
Lungs	0.12
Colon	0.12
Stomach	0.12
Liver	0.05
Thyroid	0.05
Oesophagus	0.05
Breasts	0.05
Urinary Bladder	0.05
Bone Surface	0.01
Skin	0.01
Remainder [a b]	0.05

[a]The remainder organs are the adrenals, brain, kidneys, pancreas, small intestine, spleen, thymus, uterus and muscle.

[b]If one of the remainder organs receives a radiation dose that is higher then all other weighted organs then that organ is weighted by 0.025 and the rest of the remainder organs will receive a weight of 0.025.

2.2 Dose measurement

2.2.1 Equipment

Dose is most commonly measured using an ionisation chamber or thermoluminescent dosemeters (TLDs), with or without a phantom present.

2.2.1.1 Ionisation chambers

A simple explanation of an ionisation chamber is that it is a chamber containing negatively and positively charged plates, which are separated by air. The ionising radiation enters the chamber and ionises the air molecules by the photoelectric effect and Compton scattering. The negatively charged electrons move to the positive plate and the positively charged ions move to the negative plate and receive electrons. This creates a current through the wire supplying the two plates, which can be measured and used to calculate D_A (Dendy and Heaton, 1987; Hering, 1995), as shown in Figure 2.3.

Figure 2.3: A simplified diagram of an ionisation chamber.

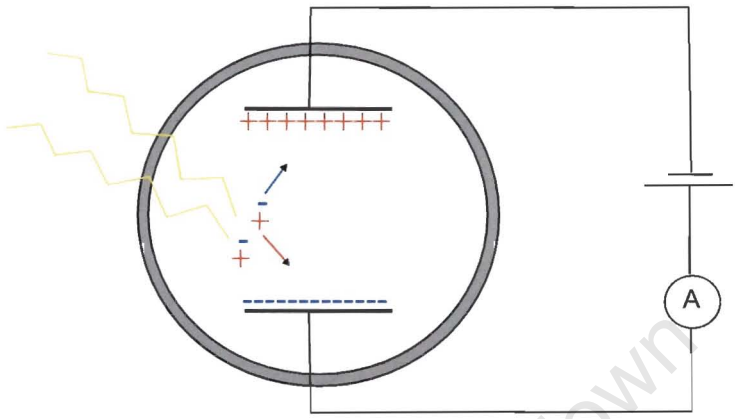

The measurement, however, requires that all secondary electrons are also measured (as discussed in Section 2.1.4). These secondary interactions must therefore occur within the volume of the chamber. This is achieved by using a free-air ionisation chamber (Hering, 1995). Only a small volume of a free-air ionisation chamber is exposed to radiation. The rest of the chamber must then be large enough for the secondary electrons to ionise the air. This total charge is then divided by the mass of the directly exposed air to calculate X. This makes the chamber large and difficult to use but is the most accurate type of chamber (Dendy and Heaton, 1987; Hering, 1995). Alternatively, an air-wall chamber can be used. This chamber has a wall that has a radiographically equivalent atomic number to air (i.e. the ratio of the various interactions occurring remains the same). However, the wall is much denser than air and, therefore, simulates a larger volume of air. The wall must be at least as thick as the range of the secondary electrons (Hering, 1995). The whole volume is exposed during an examination. Only the charge in the chamber is measured and, therefore, as long as the walls are thicker than the range of secondary electrons, the flux of secondary radiation entering the chamber will equal that leaving the chamber; the measurement includes both primary and secondary radiation.

2.2.1.2 Thermoluminescent dosimetry

Thermoluminescent dosemeters (TLDs) are made up of crystals that are modified when exposed to radiation, resulting in electrons in the crystals being energised and moving out of the ground state band. After the TLDs have been exposed, some of the electrons remain trapped in an upper energy band. These TLDs can then be heated which results in the electrons returning to the ground state band and light being emitted. This light can be measured and is proportional to the amount of radiation

the crystal was exposed to (Dendy and Heaton, 1987; Hering, 1995).

2.2.1.3 Phantom

Anthropomorphic phantoms are human-like models that consist of materials that are radiographically equivalent to the tissues in the body. Natural human bone is often used to create the material for the phantom skeleton and artificial materials are used to simulate the other organs and tissues. The Rando anthropomorphic phantom (Alderson Research Laboratories) used in this study has holes throughout the phantom, in which TLD's can be inserted (Theocharopoulos et al., 2002).

Mathematical phantoms have also been developed that specify the coordinates and shape of organs and tissues in the body. These can be used along with Monte Carlo simulators to calculate the dose to the patient (Servomaa and Tapiovaara, 1998).

2.2.2 Entrance dose measurement

Entrance dose (free in air) and exposure are commonly measured using an ionisation chamber placed at the focus-to-skin distance (FSD) for the required examination (Samei et al., 2004). FSD is the distance from the X-ray focal spot to the surface of the patient.

Measurement of ESD is similar except that the ionisation chamber or TLDs used are placed on a phantom or a patient (Compagnone et al., 2005, 2006; Papadimitriou et al., 2001). The phantom or patient is used to include backscatter in the measurement. Papadimitriou et al. (2001) and Gogas et al. (2003) used TLDs at the centre of the beam attached to patients undergoing X-ray examinations to measure ESD. Papadimitriou et al. (2001) calibrated the TLDs against ionisation chambers "free-in-air" while Gogas et al. (2003) used an ionisation chamber above 15cm thick Plexiglas to simulate backscatter in the calibration. Compagnone et al. (2005, 2006) used an ionisation chamber placed on the surface of a phantom and at the centre of the beam to measure ESD.

2.2.3 Effective dose measurement

Effective dose cannot be measured directly but the most direct method is to measure individual organ doses using TLDs. TLDs are inserted into an anthropomorphic phantom in the positions of the organs (Samei et al., 2005; Theocharopoulos et al., 2002). Thus, the dose received by the organ will be measured by the TLDs when the phantom is exposed to radiation during the examination of interest. To increase measurement accuracy of TLDs, Theocharopoulos et al. (2002) exposed them 50 times

for each examination.

TLDs are generally calibrated against an ionisation chamber to obtain D_A. The D_A for a particular organ is calculated by averaging the measurements of D_A made by TLDs inserted in that organ (Samei et al., 2004; Theocharopoulos et al., 2002). The tissue dose can then be calculated from the D_A measured for that tissue (Theocharopoulos et al., 2002)

$$D_{tissue\,i} = D_A \left(\frac{\mu}{\rho}\right)_{tissue\,i} / \left(\frac{\mu}{\rho}\right)_{air} \tag{2.9}$$

where $\left(\frac{\mu}{\rho}\right)$ is the mass attenuation coefficient (see Section 2.1.3.4). Theocharopoulos et al. (2002) used three different mass energy absorption coefficients to distinguish between bone, soft tissue and muscle.

Finally, the effective dose is calculated as the weighted average of the dose to each organ using the tissue weighting factors (w_T) discussed in section 2.1.4.4.

2.3 Dose Calculation

2.3.1 Entrance dose calculation

Many methods are used to calculate the tube output (which includes entrance dose (free-in-air), kerma, ESD, DAP and X) instead of making direct measurements. Most of these relationships are empirical or semi-empirical, meaning they are at least partly based on previously measured data. A common method for measuring the tube output, fits a function to measured entrance dose data from a specific radiographic unit (Aroua et al., 2002a; Harpen, 1996) and is then used to calculate other entrances doses. Other methods include the calculation of the energy spectrum which is then used to calculate the entrance dose (Boone and Seibert, 1997). Three methods are described below.

2.3.1.1 Function fit

Simple relationships have been derived between the technique factors and the tube output. These relationships usually include one or two constants that are found by fitting a function to the tube output from a particular X-ray machine (Aroua et al., 2002a; Harpen, 1996).

The common elements of these relationships are that

$$\text{Tube output} \propto mA \tag{2.10}$$

$$\propto s \tag{2.11}$$

$$\propto kV^{\rho}; \quad \rho \approx 2-3 \tag{2.12}$$

where s is the exposure time, mA is the tube current and kV is the tube voltage.

The following relationship is used by Harpen (1996)

$$X = \alpha(kV)^{\beta} mAs \tag{2.13}$$

where exposure (X) is related to the technique factors by two constants (α and β). Exposure can then be converted to entrance dose (see Section 2.1.4.3) or the constants can be fitted directly to entrance dose.Another example is given by Aroua et al. (2002a,b).

$$ESD = \alpha \frac{mAs}{F} \frac{kV^2}{FSD^2} \tag{2.14}$$

where the filtration (F) and FSD are included and one constant (α) is fitted. Other fixed constants are included in the equation but these can all be included in α.

2.3.1.2 Polynomial fit

The relationship between kV, filtration and exposure/mAs was fitted to a polynomial by Boone and Seibert (1997) at an FSD of 1m:

$$mR/mAs = a_0 + a_1 kV^1 + a_2 kV^2 + a_3 kV^3 \tag{2.15}$$

where the constants a_0, a_1, a_2 and a_3 have been calculated for four different filtrations. This relationship fits a polynomial to various kV and filtrations and is therefore more accurate than methods that use simple relationships between the tube output and technique factors. This method is, however, not fitted to each X-ray unit and, therefore, the unit being modelled must have a similar tube to the machine used in the Boone and Seibert (1997) study .

2.3.1.3 Energy spectrum

Boone and Seibert (1997) also created a semi-empirical model for the calculation of X-ray spectra from a tungsten anode X-ray tube:

$$\text{if} \quad \varepsilon \leq kV, \quad \Phi[\varepsilon] = \sum_{i=0}^{n} a_i[\varepsilon] kV^i \tag{2.16}$$

$$\text{else} \quad \Phi[\varepsilon] = 0 \tag{2.17}$$

where the coefficients $a_i[\varepsilon]$ are energy dependent. These are available via an ftp site (Beutel et al., 2000, pg 43) as four coefficients (i.e. n=4) for each photon energy between 1keV and 150keV in increments of 1keV, and have been tested for tube voltages between 30kV - 140 kV. A typical spectrum produced is shown in Figure 2.2.

This formula allows the energy spectrum to be calculated for a given tube voltage, which in turn can be used to calculate the tube output. This method has been used previously to model entrance dose for LSSR (Scheelke, 2005).

It is interesting to see from Equation 2.16 that keV $\leq$ kV i.e. the energy of the X-ray photons in keV will never be higher than the tube voltage (measured in kV). This is because the an electron volt (eV) is defined such that if a electron is accelerated in a 1V potential then the electron will have an energy of 1 eV (See Section 2.1.1). Therefore, as the electrons collide with the anode, they will have an energy in keV equal to the kV potential. If all the energy from a accelerated electron is transferred to a particular photon then keV = kV otherwise keV < kV(Beutel et al., 2000).

2.3.2 Effective dose calculation

As discussed in Section 2.1.4.4, effective dose (E) is dependent on the characteristics of the X-ray beam, the patient size and shape, and the type of examination. Unlike the tube output such as entrance dose (free in air), which does not take the patient into account, E requires a measurement of individual organ doses. This makes E complicated and time consuming to measure accurately.

Methods have been derived to estimate E. The most common method is by Monte Carlo simulation. Photons interact with material in various ways (See Section 2.1.2) and these interactions as well as the directions and energies of any emitted photons and electrons have various probabilities associated with them. Monte Carlo calculations simulate the paths of a large number of photons by generating random variables to simulate the probability of each interaction occurring (Servomaa and Tapiovaara, 1998). Using a mathematical phantom and the interaction cross sections associated with each tissue, the amount of energy absorbed by each organ can be calculated and from this the effective dose can be calculated.

Various Monte Carlo simulators exist. PCXMC is a commercially available Monte Carlo simulator for standard radiographic procedures and has been used in many studies (Hansen et al., 2003; Papadimitriou et al., 2001; Schultz et al., 2003). The Health Protection Agency (HPA) (formerly the National Radiation Protection Board (NRPB)) released NRPB-R262 and NRPB-R279 containing conversion coefficients

between entrance dose and effective dose (Hart et al., 1994, 1996). These conversion coefficients were generated by Monte Carlo simulation and have also been used in various studies (Compagnone et al., 2005, 2006; Gogas et al., 2003). Other Monte Carlo programmes include MCNP, the general Monte Carlo simulation code (Schultz et al., 2003; Servomaa and Tapiovaara, 1998).

2.4 Slit scanning radiography

Slit or slot scanning radiography is a technique that uses a thin fan beam of X-rays moving across the patient in order to acquire an image. This technique results in a lower scatter than conventional radiography (Barnes et al., 1985, 1994; Potgieter et al., 2005; Samei et al., 2004, 2005) but has a much lower tube output efficiency because the beam is highly collimated, usually to less than 1cm.

The difference between *slit* and *slot* has been defined in different ways in various studies. Shikhaliev et al. (2005) describe slit scanning as having a detector with one row of pixels in the scanning direction while slot scanning has multiple rows of pixels. Barnes et al. (1994), however, state that the two terms are often used interchangeably but defines them in terms of the thickness of the collimator, where a collimator of thickness less than 1.5mm is called a slit and over 1.5mm is called a slot. Other studies such as that of Samei et al. (2005) do not distinguish between the two. In this study, the term slit scanning is used to describe a radiography unit with a highly collimated moving fan beam.

A typical slit scanning unit is described by Samei et al. (2004, 2005). In the slit scanning system that they evaluate, a moving collimator with a width of 1cm is used to create and direct the fan beam during the scan (as shown in Figure 2.4). This set-up leads to the same geometry as conventional radiography but offers much lower scatter because of the narrow detector and narrow fan beam.

Linear slit scanning involves moving the X-ray tube linearly during the examination. This means that the beam is always perpendicular to the patient and results in no image magnification in the scanning direction (as shown in Figure 2.4). This set up results in a lower dose compared to conventional radiography. The reasons for this are developed in Section 5.3.

Figure 2.4: Diagram showing the difference in geometry between slit scanning and linear slit scanning radiography units for the same entrance area.

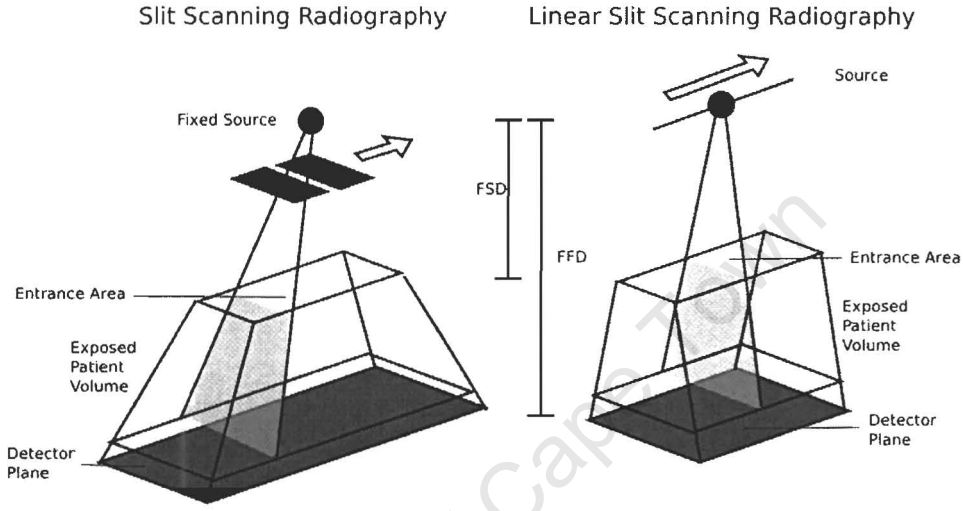

It is important to know the length of time that each point on the entrance area is exposed. On a conventional X-ray machine this is the length of time that the X-ray beam is present during the examination. For slit scanning radiography an effective exposure time can be calculated taking into account the speed of the scan and the width of the beam at the patient skin distance.

The effective exposure time is:

$$\text{exposure time} = \frac{\text{beam width}}{\text{scan speed}} \tag{2.18}$$

Therefore, for linear slit scanning the beam width can be calculated from the collimator width to give the following (making the simplification that the X-rays are being emitted from a point source) (Scheelke, 2005).

$$s = \frac{\text{FSD}}{\text{FCD}} \frac{\text{collimator width}}{\text{scan speed}} \tag{2.19}$$

where FSD is the focus-to-skin distance, FCD is the focus-to-collimator distance, *collimator width* is the width of the collimator in the scanning direction and *scan speed* is the speed of the fan beam during the scan.

As discussed earlier (Section 2.1.3.3), the X-ray beam must be optimised for each examination to give the best image quality. However, slit scanning and linear slit scanning offer an additional improvement. Unlike conventional radiography where the whole image is acquired at once, for slit scanning the beam moves across the patient. This means the beam can be optimised for each section of the examination by adjusting the technique factors as the scan progresses. This procedure is known as automated technique factor control (ATFC) and is discussed further in Chapter 6.

dependent on temperature and pressure outside the chamber. The ionisation chamber is calibrated to the standard temperature and pressure and so a correction factor must be included to take into account the change in air density. The temperature and pressure must be measured and used to calculate the correction factor (Khan, 1994).

$$C = \left(\frac{1013.25\,\text{hPa}}{\text{P}}\right)\left(\frac{T}{293\,\text{K}}\right) \tag{3.1}$$

where P is the pressure and T is the temperature.

There is also a relationship between the photon energy and the ratio of dose/reading for the PMMA chamber, as shown in Figure 3.1. This relationship is based on data provided by PTW Freiburg and has been previously used by the Division of Medical Physics, Groote Schuur Hospital (G Maree, Groote Schuur Hospital, personal communication, 2006). Therefore, for each examination, the effective energy of the beam must be calculated from the tube voltage. This is then used with the fitted polynomial to obtain the dose/reading correction factor.

Figure 3.1: A fitted polynomial showing the relationship between the chamber reading and the dose.

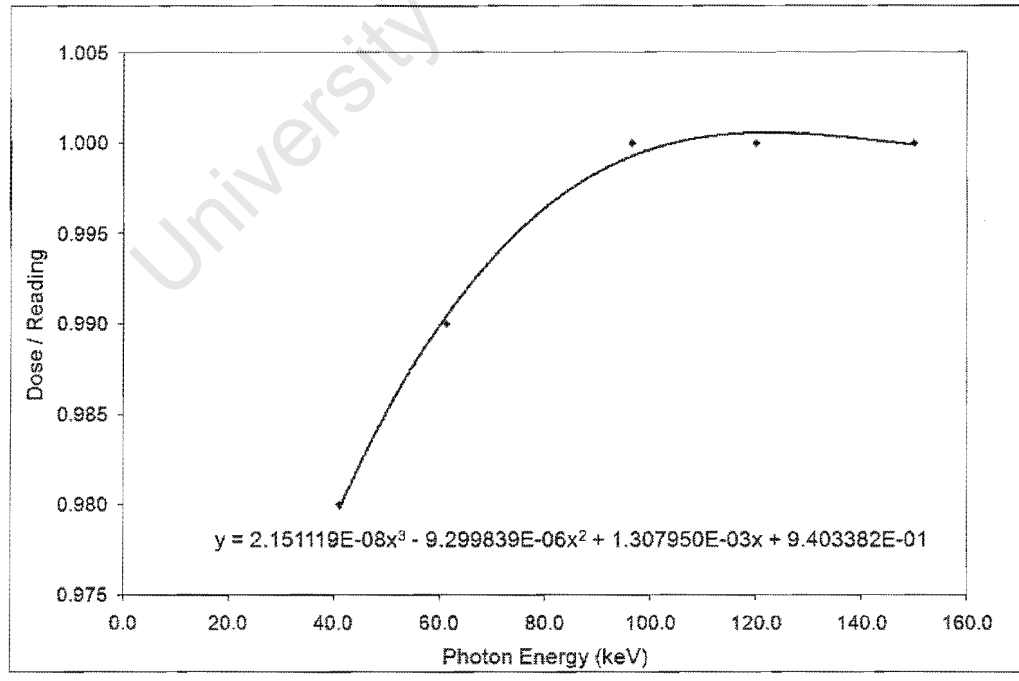

3.1.3 Radiography Units

3.1.3.1 The Lodox Statscan linear slit-scanning radiography unit

Lodox Systems (Johannesburg, South Africa) have developed low dose trauma digital X-ray equipment (Statscan) with full-body scanning capabilities (Beningfield et al., 2003).

Statscan (Figure 3.2) uses a rotating anode X-ray tube (1mm of aluminium equivalent inherent filtration and 1mm added aluminium filtration) mounted on a C-arm. A collimated fan-beam of X-rays is emitted via an adjustable collimator of width 0.4mm or 1.0mm. Fixed to the other end of the C-arm is the X-ray detector unit, comprising scintillator arrays optically linked to charge-coupled devices (CCDs). The fundamental pixel size of the detectors is 60μm, with a maximum image size of 12283 $\times$ 8000 pixels. Fourteen bits of contrast resolution can be recorded and a spatial resolution of between 1.04 lp/mm and 5.0 lp/mm can be selected.

Figure 3.2: Statscan linear slit scanning X-ray machine.

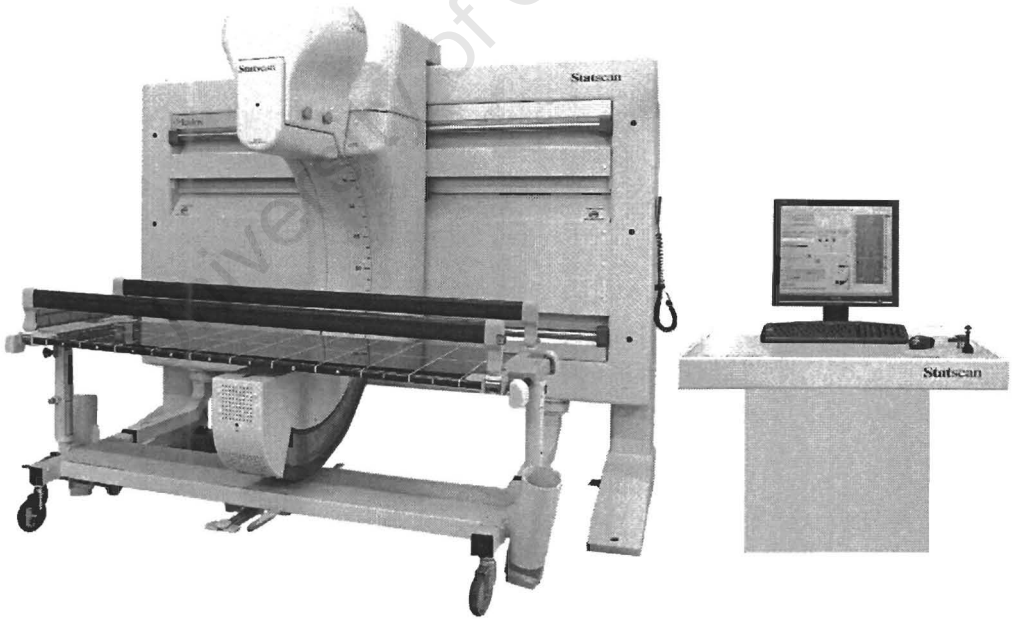

The C-arm can rotate axially around the patient to any angle up to 100° allowing scans at different angles, e.g. lateral and antero-posterior (AP). During a scan, the C-arm travels along the table length at speeds ranging between 35 and 140 mm/s. Full-body scans are completed in less than 13 seconds; the diagnostic image is available for viewing less than 15 seconds after the end of a scan (Lodox, 2006). The user interface allows the selection of patient size (paediatric, small, medium, large and extra large) and type of scan; the collimator width and technique factors are automatically selected (Beningfield et al., 2003; Miller et al., 2004). The technique factors have been selected by Lodox Systems with the intention of optimising image quality and dose. The images can either be viewed on a high luminance two megapixel monitor or printed onto film.

3.1.3.2 The Shimadzu conventional radiography unit with Fuji computed radiography system

The Shimadzu radiography unit (Shimadzu Medical Systems, Kyoto, Japan) is a conventional radiography unit and is used in conjunction with a film-free Fuji computed radiography system (Fuji Photo Film Company, Tokyo, Japan). The Shimadzu radiography unit (model R-20J) at the Red Cross Children's Hospital uses a Shimadzu tube (Circlex 0.6/1.2P324DK-1000SF) manufactured in February 2004. The radiography unit contains 1.5 mm of aluminium equivalent inherent filtration and 1 mm added aluminium filtration. The Fuji FCR 5000 computed radiography system uses phosphor-screen imaging plates to record the image. The image is then read by a film digitiser that stores the image in the computer database. The system has a 12-bit grey-scale resolution at 5 lp/mm, and a pixel size of 100 μm (Pitcher et al., 2008). The image is viewed on a 19-inch 2-megapixel monitor. The technique factors for each scan, such as the tube voltage, are given on charts for the radiographer to follow. These charts have three patient age categories: 3 years, 6 years and 10 years.

3.2 Verification of methods

3.2.1 Verification of the dosemeter

There has been discussion about whether conventional ionisation chambers can be used with LSSR because with LSSR the entire ionisation chamber is not exposed at the same time. PTW Freiburg and Radcal Corporation have stated that all their chambers used in conventional radiography can be used with linear slit scanning devices as long as the beam moves over the entire chamber and the technique factors are not changed during the scan (see Appendix B.2 and B.1). This section describes

measurements that were performed to verify experimentally that conventional ionisation chambers could be used with LSSR.

3.2.1.1 Method

Entrance surface dose (*ESD*) was measured using the 30 cm^3 PTW PMMA ionisation chamber (discussed in Section 3.1.2) and a PTW CT ionisation chamber (Type 30009) on the Statscan linear slit scanning X-ray machine on 1 August 2007. Firstly, calibration factors between the two chambers were found using a Siemens conventional X-ray machine. These calibration factors was used to calculate the *ESD* from charge imparted in the CT chamber. The CT chamber is designed for CT measurements, has a sensitive length of 10cm, and can be partially exposed. It will, therefore, measure dose accurately on linear slit scanning X-ray machines. The *ESD* from the CT chamber on Statscan was then compared to the *ESD* from the PMMA chamber on Statscan to determine whether the PMMA chamber could also be used with Statscan.

The Siemens X-ray machine and Statscan linear slit scanning X-ray machine at Groote Schuur Hospital were used in this study. Statscan and Siemens have a total filtration of 2mmAleq and 2.5mmAleq respectively.

The CT and PMMA chambers were positioned above a phantom pelvis with a FSD of 84 cm (see Figures 3.3 and 3.4). A number of X-ray examinations were taken at 70 kV and 100 kV on both the Siemens X-ray machine and Lodox Statscan. The PMMA ionisation chamber with dosemeter gave a dose in mGy while the CT chamber gave a charge measurement in nC. Both chambers were fully exposed during each examination. On Statscan this meant that both chambers were scanned over completely during the examination. Measurements were taken on Statscan with the CT chamber both parallel and perpendicular to the scan direction. The dose from the PMMA ionisation chamber was corrected for temperature, pressure and kV sensitivity. A calibration factor between the two chambers (i.e. the ratio of the dose measured with the PMMA chamber and the charge measured with the CT chamber) was found at 70 kV and 100 kV on the Siemens X-ray machine. This was used to calibrate the CT chamber and thus, calculate ESD from the measured charge on Statscan.

Figure 3.3: The two chambers above a phantom.

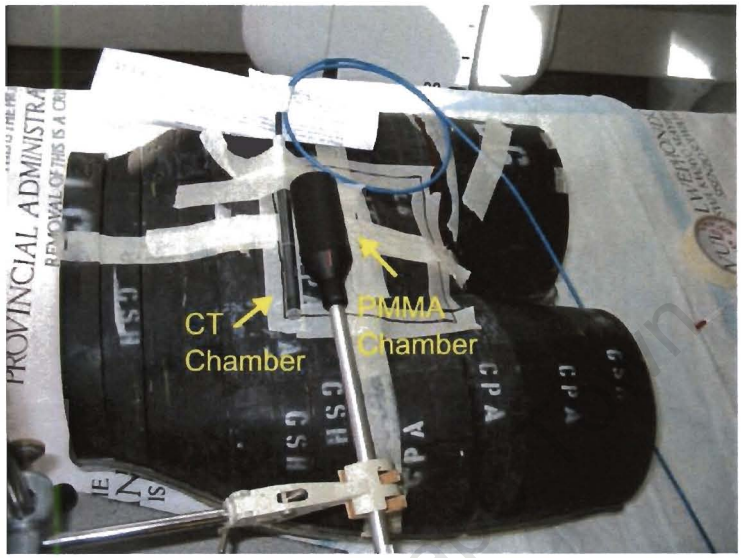

Figure 3.4: The two chamber set up for the conventional X-ray machine.

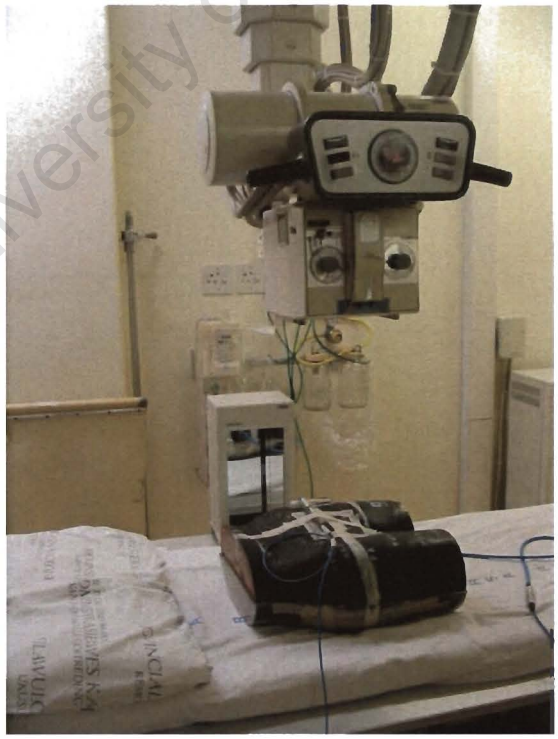

3.2.1.2 Results

Table 3.1 shows the *ESD* measured with the PMMA chamber, the charge measured with the CT chamber and the calibration factors between the two chambers at 70 kV and 100kV on the Siemens X-ray machine. The calibration factors at 70 kV and 100 kV were 9.99 Gy/μC and 9.65 Gy/μC respectively and were used to calculate the *ESD* from the CT chamber on Statscan. Tables 3.2 and 3.3 show the measured *ESD* on Statscan using the PMMA and CT chambers where the *ESD* for the CT chamber uses the Calibration factor derived in Table 3.1. The *ESD* difference between the measurement with the CT chamber and the PMMA chamber on Statscan was between 1% and 4%.

Table 3.1: Radiation measurements on Siemens conventional X-ray machine for calibration of CT chamber.

kV	mAs	PMMA chamber (mGy)	CT chamber (nC)	Calibration factor Gy/μC
70	200	12.73	1.275	9.99
70	320	20.37	2.039	9.99
100	100	14.70	1.524	9.65
100	100	14.71	1.524	9.65

Table 3.2: *ESD* measurements on Lodox Statscan with CT chamber parallel to the scanning direction (FSD = 84cm).

kV	mA	Slit width (mm)	Focal spot	Speed (mm/s)	PMMA chamber ESD (uGy)	CT chamber charge (pC)	CT chamber ESD (uGy)	ESD difference
70	100	0.4	S	70	95.61	9.89	98.80	3%
70	100	0.4	S	70	96.20	9.99	99.83	4%
70	100	1.0	L	70	246.36	25.74	257.08	4%
100	100	0.4	S	70	189.93	20.51	197.88	4%
100	100	0.4	S	70	189.93	20.46	197.38	4%
100	100	1.0	L	70	483.39	52.25	504.19	4%

Table 3.3: *ESD* measurements on Lodox Statscan with CT chamber perpendicular to the scanning direction (FSD = 84cm).

kV	mA	Slit width (mm)	Focal spot	Speed (mm/s)	PMMA chamber ESD (uGy)	CT chamber charge (pC)	CT chamber ESD (uGy)	ESD difference
70	100	0.4	S	70	100.30	10.31	102.93	3%
70	100	1.0	L	70	251.05	24.96	249.32	1%
100	100	0.4	S	70	198.21	21.03	202.87	2%
100	100	1.0	L	70	489.90	50.34	485.70	1%

3.2.1.3 Discussion

The agreement between *ESD* found using the PMMA ionisation chamber and the CT ionisation chamber on Statscan indicates that the PMMA ionisation chamber can also be used with linear slit scanning technology as long as the ionisation chamber is scanned over completely during the examination and none of the technique factors are changed during the scan. This confirms what has been stated by PTW Freiburg and Radcal Corporation. The dose difference between the two chambers on Statscan of less than 4% can be explained by the Siemens conventional X-ray machine having 0.5mm Aleq more filtration than Statscan. The results from this study show that ionisation chambers used to measure entrance surface dose in conventional radiography can also be used to measure dose on linear slit scanning X-ray machines.

3.2.2 Verification that PCXMC can be applied to LSSR

PCXMC is used for the calculation of E because LSSR geometry only has a small effect on the conversion coefficients between entrance dose and effective dose. As shown in Figure 5.1, if the dose-area product (DAP) entering the patient is the same for both conventional radiography and LSSR, the DAP will be the same at any distance. However, the beam area of LSSR only grows perpendicularly to the scanning direction. Thus, the same energy will be imparted by conventional radiography over a slightly larger volume than by LSSR, and there will only be a small difference in E (for the same entrance dose), affected only by a tissue weighting difference for organs present in the slightly larger area irradiated in conventional radiography.

This has been verified by running simulations on PCXMC comparing conventional full field calculations to summed slice increments at a fixed distance. Previously, the scan area for Abdomen AP was divided into 186 increments of dimension 0.2×38 cm^2 at a fixed FSD to simulate LSSR. This was compared to the same area exposed by a conventional radiographic unit. The dose for the conventional unit and slit-scanning unit were 8.17 mSv and 8.20 mSv, respectively, using an arbitrary entrance dose; a difference of 0.31% (G Maree, Groote Schuur Hospital, personal communication, 2006).

Further simulations during this project using common examinations and beam slice widths of 0.2 cm and 0.8 cm have revealed that the errors are larger than previously predicted but still small. Figure 3.4 shows the doses obtained for full field examinations and doses obtained for the same examinations when divided into increments. An arbitrary but very high entrance dose of 10mGy was used in all these simulations. This was done because E is calculated as being proportional to entrance

dose. However, by using a high entrance dose, more significant figures are obtained to the dose values of small iterations. This makes the comparison more accurate. An FSD of 90cm was used for these comparisons. These results were simulated using the Monte Carlo simulator PCXMC and by writing a key logging script in the programme Autohotkey that would repeat simulations to obtain individual simulations for each increment of the beam. The results recorded for these examinations show deviations of between -5.8% and 5.3% for 0.2 cm increments and between -3.7% and 2.2% for 0.8cm increments. Thus, PCXMC can be used for the calculation of effective from measured entrance doses in LSSR.

Table 3.4: Differences in effective dose between full field and iterative approach for common examinations.

			Effective Dose				
Scan type	Beam height (cm)	Z coordinate (cm)	Full field (mSv)	Slit 0.2 (mSv)	Difference %	Slit 0.8 (mSv)	Difference %
Chest AP	30.0	56.4	2.29	2.19	-4.2	2.23	-2.5
Abdomen AP	37.6	17.0	3.34	3.46	3.6	3.39	1.5
Pelvis AP	28.2	12.3	2.45	2.58	5.3	2.50	2.2
Skull AP	19.4	83.5	0.25	0.23	-5.8	0.24	-3.7
Top of skull to bottom of pelvis AP	94.0	47.0	6.31	6.32	0.1	6.37	1.0

Once these methods were verified, they could be used to measure dose for adult and paediatric patients. The method of measuring entrance dose and calculation of effective dose for adult and paediatric patients is discussed in Chapter 4.

4

Dose measurement: measurements for paediatric and adult patients

The chapter contains extracts from two articles published in peer-reviewed journals and included in the Appendix. For the first article, *Maree G, Irving B, and Hering E. Paediatric dose measurement in a full-body digital radiography unit. Ped. Radiol. 2007; 37:990-997*, B Irving, the author of this dissertation, was responsible for writing the paper and for all discussions and comparisons within the paper. The dose measurements used in this paper were performed by G Maree, B Irving and E Hering. The tables in this chapter state which data was not obtained by the author of this dissertation. The second article is: *Irving B, Maree G, Hering E and Douglas T. Radiation dose from a linear slit scanning X-ray machine with full body imaging capabilities. Rad. Prot. Dosim. 2008; (in press).* B Irving was responsible for the writing of this article, as well as the calculations, discussion and the measurements. These tasks were performed with the guidance of the other authors.

This chapter discusses entrance dose and effective dose calculations made for standard X-ray examinations on the linear slit scanning radiography unit (LSSR), Statscan. Entrance dose (free in air) was measured for LSSR using an ionisation chamber and dosemeter, and effective dose was calculated from the entrance dose using PCXMC. The dose measurements on Statscan were then compared to measurements performed on a computed radiography (CR) unit as well as dose measurements from around the world (Compagnone et al., 2005; Geleijns et al., 2000; Gogas et al., 2003; Mohamadain et al., 2004).

4.1 Paediatric Patients

4.1.1 Method

Three radiography units were evaluated in this study, the Lodox Statscan unit in the trauma ward of Groote Schuur Hospital, and the Lodox Statscan unit and the Shimadzu radiography unit in the emergency unit of the Red Cross War Memorial Children's Hospital. Groote Schuur Hospital and the Red Cross Children's Hospital are both situated in Cape Town, South Africa. The Radiography Department at the Red Cross Children's Hospital is dedicated to children and a lot of work has been done to optimise the technique factors on the Statscan unit for the best image quality. Unlike Groote Schuur Hospital, which has only one paediatric age setting, the Red Cross Children's Hospital has two paediatric settings: *infant* and *paediatric*. The infant setting has a fan beam collimation of 0.3 mm while the paediatric setting has a collimation of 0.4 mm. In this study, effective doses were calculated for two paediatric age groups, 1 year old and 5 years old. Standard sizes were chosen for each age group (see Table 4.1). The paediatric setting was used for the 5-year-olds and the infant setting was used for the 1-year-olds. The height, weight and age shown in Table 4.1 are required as input to the PCXMC Monte Carlo program. The effective dose was calculated for 11 of the different projections available on the Statscan unit: AP full-body, AP chest (lung), lateral chest (lung), AP abdomen, lateral abdomen lumbar, AP pelvis, lateral pelvis, AP skull, lateral skull and lateral cervical spine. For the Shimadzu unit, the effective dose was calculated for nine different projections: AP chest (lung), AP erect chest, lateral erect chest, AP abdomen, AP pelvis, AP skull, lateral skull, Townes skull and lateral cervical spine.

Table 4.1: Standard paediatric patient sizes.

Age group (years)	Height (cm)	Weight (kg)
1	64	7
5	109	20

In order to calculate the effective doses, the entrance dose was measured for each of the scans. In most cases two measurements were taken for each examination (Tables 4.2 and 4.4). The entrance dose (free-in-air) was measured using the PTW-UNIDOS dose meter and the PTW cylindrical ionisation chamber discussed in Section 3.1.2.

The ionisation chamber was attached to a stand 105 cm above the ground in the centre of the X-ray beam. The height was chosen to approximate the height of skin entrance of a patient lying on the bed. Each type of scan was selected on the panel of the Statscan unit, which automatically selected the specific technique factors for the scan, and a scan was taken over the ionisation chamber. After the measurements had been taken, small corrections were made to the entrance dose to take into account the variation in skin entrance height for each section of the body. Corrections were also made to take into account temperature, pressure and kV sensitivity of the ionisation chamber, as discussed in Section 3.1.2.

The dimensions of the mathematical phantoms of PCXMC were used to determine the field size of each examination. Various organs are indicated on the mathematical phantoms, and served as landmarks to determine the field size of various patient sizes. The field size, entrance dose, technique factors and FSD were entered into PCXMC for each scan. The PCXMC Monte Carlo simulation was run to obtain the effective dose.

4.1.2 Results

Tables 4.2, 4.3 and 4.4 summarise the technique factors, measured entrance dose in air, field size and calculated effective dose for each scan. Measurements 1 and 2 in Tables 4.2 and 4.4 are entrance dose readings without correction, and the corrected average values are the averages of measurements 1 and 2 corrected for the sensitivity of the ionisation chamber. Table 4.2 includes the complete set of readings and settings at Groote Schuur Hospital, while Table 4.3 shows only the important details of the measurements taken at the Red Cross Children's Hospital. The same methods were used at both hospitals. Entrance dose measurements were taken at Groote Schuur on 1 September 2005, 14 August 2006 and 12 December 2006, and at the Red Cross Children's hospital on 6 October 2005 (Statscan unit) and on 20 October 2005 (Shimadzu unit). The standard deviations of the entrance dose measurements were in the range of 0 to 0.6%. Lodox makes regular adjustments to the technique factors on their units in order to try and improve image quality. Thus, between 2005 and 2006 some of the technique factors were changed resulting in different dose measurements for the same examination (as shown in Table 4.2). A range was included in Table 4.5 to show the trend in entrance dose for particular scans on the Statscan unit. Table 4.5 shows the highest and lowest dose measured for particular scans on the Statscan unit for 5-year-olds, as well as doses measured for the same examinations around the world. Figure 4.1 represents the effective doses shown in Table 4.5 for the Statscan and Shimadzu units graphically, and clearly shows the lower dose obtained from the Statscan unit.

The effective doses for the standard trauma imaging protocol used at the Red Cross Children's Hospital are shown in Table 4.6. The staff at the Red Cross Children's Hospital have judged that it is sufficient to use the AP full-body and lateral cervical spine on the Statscan unit, or the AP chest, AP pelvis and lateral cervical spine on the Shimadzu unit. The effective doses for the examinations in Table 4.6 are included in Tables 4.3 and 4.4. A slit width of 0.3mm was used for examinations simulating a patient of age 1 and a slit width of 0.4mm was used for simulations of examinations to 5 year old patients.

Table 4.2: Entrance dose and effective dose for particular scans on the Lodox Statscan Unit at Groote Schuur Hospital (Measurements were obtained by the author of this disseration and by E Hering and G Maree).

Examination	Age (years)	kVp	Focal spot	mA	Scan speed	SSD (cm)	Fieldsize (cm) X	Fieldsize (cm) Z	Entrance Dose (μGy) Measurement 1	Entrance Dose (μGy) Measurement 2	Entrance Dose (μGy) Corrected Average	Effective dose (μSv)
140 Body AP[a]	5	80	S	100	140	98.00	22.00	109.00	41.40	41.49	40.83	29.39
140 Body AP [b]	5	80	L	160	140	98.00	22.00	109.00	68.62	-	69.17	51.79
Chest (lung) AP[a]	5	100	S	64	140	99.30	20.00	20.50	40.87	40.98	40.51	12.32
Chest (lung) AP[b]	5	60	S	64	70	99.30	20.00	20.50	30.02	-	29.65	5.22
Chest (lung) LAT[a]	5	110	S	100	140	72.40	15.50	18.70	101.40	101.40	100.57	16.56
Chest (lung) LAT[c]	5	100	S	64	70	72.4	15.50	18.70	107.21	107.23	108.44	14.88
Abdomen AP[a]	5	80	S	125	140	98.00	20.80	21.50	51.12	51.44	50.52	15.95
Abdomen AP[b]	5	80	S	80	70	98.00	20.80	21.50	70.03	-	69.68	22.60
Abdomen Lum LAT[a]	5	100	S	200	70	72.40	14.50	22.00	170.40	171.00	168.95	27.64
Abdomen lum LAT[c]	5	90	S	200	70	72.40	14.50	22	272.79	272.51	275.11	45.11
Pelvis AP[a]	5	80	S	125	140	98.00	22.00	16.30	51.81	52.01	51.14	13.63
pelvis AP[b]	5	80	S	64	70	98.00	22.00	16.30	52.97	-	52.7	12.97
Pelvis/Hip LAT[a]	5	100	S	160	140	72.40	13.80	16.00	140.50	140.40	139.01	17.37
Pelvis/Hip LAT[c]	5	90	S	64	70	72.40	13.80	16	89.93	89.75	90.65	8.38
Skull AP[a]	5	90	S	200	140	93.50	13.50	16.50	111.20	111.20	109.81	2.59
Skull AP[b]	5	90	S	125	70	93.50	13.50	16.50	130.62	-	130.34	2.99
Skull LAT[a]	5	80	S	200	140	80.40	17.50	17.00	104.20	104.20	102.65	2.45
Skull LAT[c]	5	80	S	125	70	80.4	17.50	17.00	124.91	125.15	125.8	2.97
C Spine LAT[a]	5	70	S	200	140	72.40	10.30	10.30	93.68	93.47	91.93	0.97
C Spine LAT[c]	5	70	S	125	70	72.40	10.30	10.30	108.69	108.5	0.1089	1.20
Full Spine Lat[a]	5	100	S	125	70	72.40	10.20	45.00	222.70	223.80	220.96	37.03
Full Spine LAT[c]	5	100	S	125	70	72.40	10.20	45	205.61	205.75	208.01	34.85

[a]Entrance Dose (free-in-air) readings taken on 1 September 2005
[b]Entrance Dose (free-in-air) readings taken on 14 August 2006
[c]Entrance Dose (free-in-air) readings taken on 12 December 2006

Table 4.3: Entrance dose and effective dose for particular scans on Lodox Statscan at Red Cross Children's Hospital (Measurements were obtained by G Maree and E Hering).

Examination	Age (years)	kVp	mA	Scan speed	SSD (cm)	Entrance Dose (μGy)	Effective dose (μSv)
Full Body AP	1	90	160	140	98.00	81.84	66.71
Full Body AP	5	90	160	140	98.00	104.03	82.02
Chest (lung) AP supine	1	100	80	140	99.30	47.09	14.24
Chest (lung) AP supine	5	100	80	140	99.30	59.94	18.11
Chest (lung) LAT	1	110	125	140	72.40	117.13	23.78
Chest (lung) LAT	5	110	125	140	72.40	149.28	24.95
Abdomen AP	1	80	160	140	98.00	66.27	23.67
Abdomen AP	5	80	160	140	98.00	84.67	26.46
Abdomen Lumbar LAT	1	100	250	140	72.40	200.02	44.98
Abdomen Lumbar LAT	5	100	250	140	72.40	254.14	42.33
Pelvis AP	1	80	160	140	98.00	66.47	18.95
Pelvis AP	5	80	160	140	98.00	84.44	23.08
Pelvis / Hip LAT	1	100	200	140	72.40	160.52	27.88
Pelvis / Hip LAT	5	100	200	140	72.40	204.14	25.60
Skull AP	1	90	250	140	93.50	133.46	5.84
Skull AP	5	90	250	140	93.50	169.84	4.06
Skull LAT	1	80	250	140	80.40	122.93	5.63
Skull LAT	5	80	250	140	80.40	156.65	3.77
C Spine LAT	1	80	160	70	72.40	176.00	2.98
C Spine LAT	5	80	160	70	72.40	223.63	2.82
Full Spine LAT	1	100	160	70	72.40	256.67	55.76
Full Spine LAT	5	100	160	70	72.40	326.21	61.33

Table 4.4: Entrance dose and effective dose for particular scans on CR at Red Cross Children's Hospital (Measurements were obtained by G Maree and E Hering).

Examination	Age (years)	kVp	mAs	Focus-to-probe distance (cm)	FFD (cm)	FSD (cm)	Fieldsize (cm)		Entrance Dose (μGy)			Effective dose (μSv)
							X	Z	Measurement 1	Measurement 2	Corrected Average	
Chest Lung AP	1	54	4	100.00	120.00	100.32	13.30	13.00	110.99	111.98	109.78	20.24
Chest Lung AP	5	58	4	100.00	120.00	97.08	20.00	20.50	145.79	145.79	143.78	24.90
Erect Chest AP	1	63	4	100.00	120.00	103.32	13.30	13.00	151.19	151.76	149.64	30.32
Erect Chest AP	5	66	4	100.00	120.00	100.08	18.50	20.50	175.12	175.52	173.36	33.64
Erect Chest LAT	1	73	4	100.00	120.00	101.26	11.50	12.00	203.64	203.15	201.53	30.15
Erect Chest AP	5	76	4	100.00	120.00	95.48	15.50	18.70	241.65	-	239.64	29.44
Abdomen AP	1	55	20	74.00	100.00	80.32	14.70	14.00	831.67	-	819.29	215.90
Erect Chest AP	5	57	25	74.00	100.00	77.08	20.80	21.50	1294.96	-	1276.62	286.40
Pelvis AP	1	52	20	74.00	100.00	80.32	15.80	10.60	754.26	-	742.17	154.41
Pelvis AP	5	55	25	74.00	100.00	77.08	22.00	16.30	1120.76	-	1104.07	206.65
Skull AP	1	63	20	74.00	100.00	77.74	12.00	12.50	1254.04	1254.94	1239.27	30.83
Skull AP	5	66	25	74.00	100.00	74.02	13.50	16.50	1880.98	-	1859.93	30.41
Skull Lat	1	57	20	74.00	100.00	81.25	14.50	12.80	929.87	-	916.70	25.67
Skull Lat	5	57	25	74.00	100.00	76.25	17.50	17.00	1326.13	-	1307.35	22.21
Skull Townes	1	66	20	74.00	100.00	89.77	11.00	12.00	1014.60	-	1003.25	33.73
Skull Townes	5	70	25	74.00	100.00	85.47	14.20	16.00	1553.91	-	1538.37	24.49
C spine LAT	1	50	12	74.00	100.00	81.25	8.00	8.00	428.02	-	420.82	3.69
C spine LAT	5	52	12	74.00	100.00	76.25	10.30	10.30	533.46	-	524.91	3.36

Table 4.5: Comparison between effective dose (μSv) from Lodox Statscan, CR and other pediatric studies from around the world.

	This Study		References			
Examination	Lodox	Shimadzu	a	b	c	d
Age	5	5	5	5	1-5	3-7
Full Body AP	29.4-82.0	-	-	-	-	-
Chest (lung) AP/PA	5.2-18.1(AP)	24.9(AP)	5±2(PA)	7(PA)	12(AP/PA)	16(AP/PA)
Chest (lung) LAT	14.9-24.9	-	10±5	-	-	-
Abdomen AP	15.9-26.5	286.4	102±22	43	-	-
Abdomen Lumbar LAT	27.6-45.1	-	-	-	-	-
Pelvis AP	13.0-23.1	206.6	76±30	26	-	49
Skull AP	2.6-4.1	30.4	15±5	-	-	11
Skull Lat	2.4-3.8	22.2	12±4	-	-	7
C Spine Lat	0.97-2.8	3.4	-	-	-	-
Full Spine LAT	34.9-61.3	-	-	-	-	-

[a]Compagnone et al. (2005)
[b]Geleijns et al. (2000)
[c]Mohamadain et al. (2004)
[d]Gogas et al. (2003)

Table 4.6: Effective Doses from Lodox Statscan and Fuji CR for the Standard Trauma Imaging Protocol at Red Cross Children's Hospital.

Examination	Effective Dose (μSv)	
Age	1	5
Lodox		
Full Body AP	66.7	82.0
C Spine LAT	3.0	2.8
Total	69.7	84.8
Fuji CR		
Chest AP	20.2	24.9
Pelvis AP	154.4	206.6
C Spine LAT	3.7	3.4
Total	178.3	234.9

Figure 4.1: Effective doses from the Statscan (minimum and maximum from the measurements obtained at both hospitals) and the Shimadzu units for common radiographic examinations.

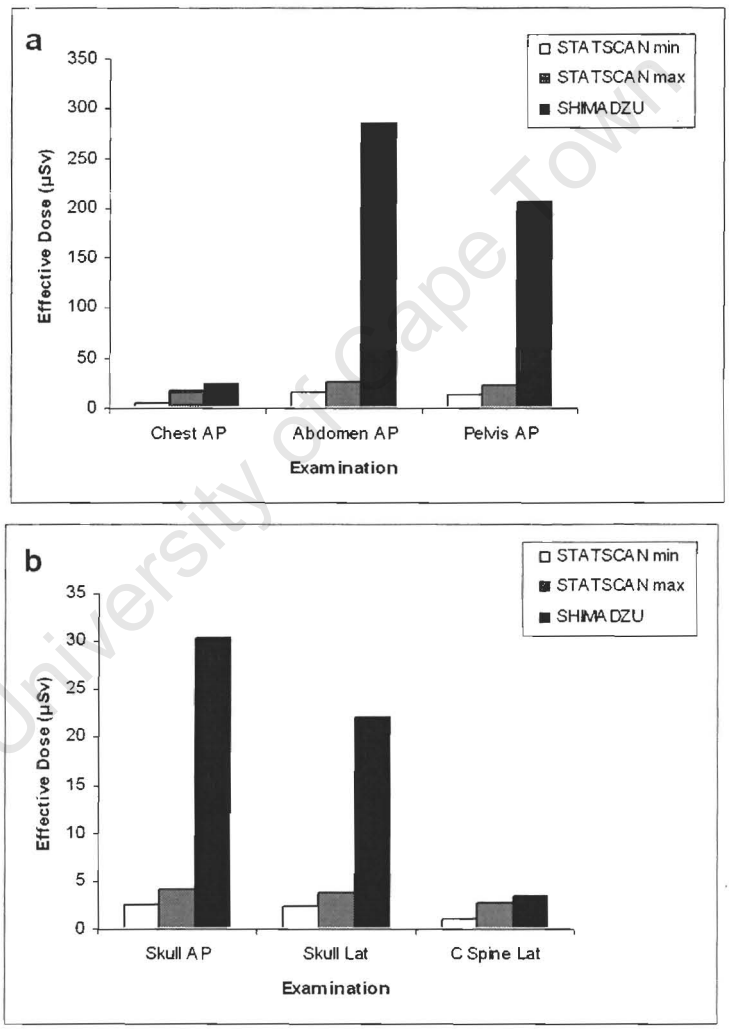

4.2 Adult patients

4.2.1 Method

Entrance dose (free-in-air) (D_A without backscatter at the patient surface distance) was measured using a PTW-UNIDOS dosemeter and ionisation chamber for a range of examinations to adult patients; Chest (AP and Lateral), Abdomen (AP and Lateral), Pelvis (AP and Lateral), Skull (AP and Lateral), Cervical Spine (Lateral), Full Spine (Lateral) and Full Body (AP). The doses were corrected for temperature, pressure and kV sensitivity of the ionisation chamber and FSD, as discussed in Section 3.1.2.

The uncertainty in the entrance dose measurements was estimated by taking 5 readings for each of the following: medium-sized patient: Chest (AP) and Pelvis (AP), and extra-large patient: Abdomen (Lateral) and Skull (AP).

The dose in air was also measured 3.5 cm above the detector (126.5 cm from tube source), with no phantom present, using the same procedure used to measure entrance dose, and for the Chest AP, Abdomen AP and Pelvis AP examinations with an Alderson Rando tissue equivalent anthropomorphic phantom present (see Figure 4.2). The scan width used in the phantom measurements was 8.5cm.

As examinations of large patients are increasing, doses to extra large patients have also been included in this study. Increased exposure parameters are required for these examinations which can result in a considerable increase in patient dose. The height and weight of a medium-sized patient are assumed to be 174 cm and 71 kg, and of an extra large patient, 200 cm and 130 kg. The technique factors used for each scan are those set by Lodox and used by Groote Schuur Hospital for each patient size.

Entrance dose was converted to E using the Monte Carlo simulator PCXMC (see Section 3.1.1) where the scan field size was calculated using the internal organs as landmarks.

4.2.2 Results

Statscan measurements including entrance dose (free-in-air), the dose in air at the detector and effective dose (E), for medium sized and extra large patients are tabulated (Tables 4.7 and 4.8). An estimate of the uncertainty in the measurement of entrance dose at the 95% confidence level was less than $\pm 0.32\%$ and the standard deviation was less than $\pm 0.26\%$.

Figure 4.2: Using the ionisation chamber to measure the dose at the detector.

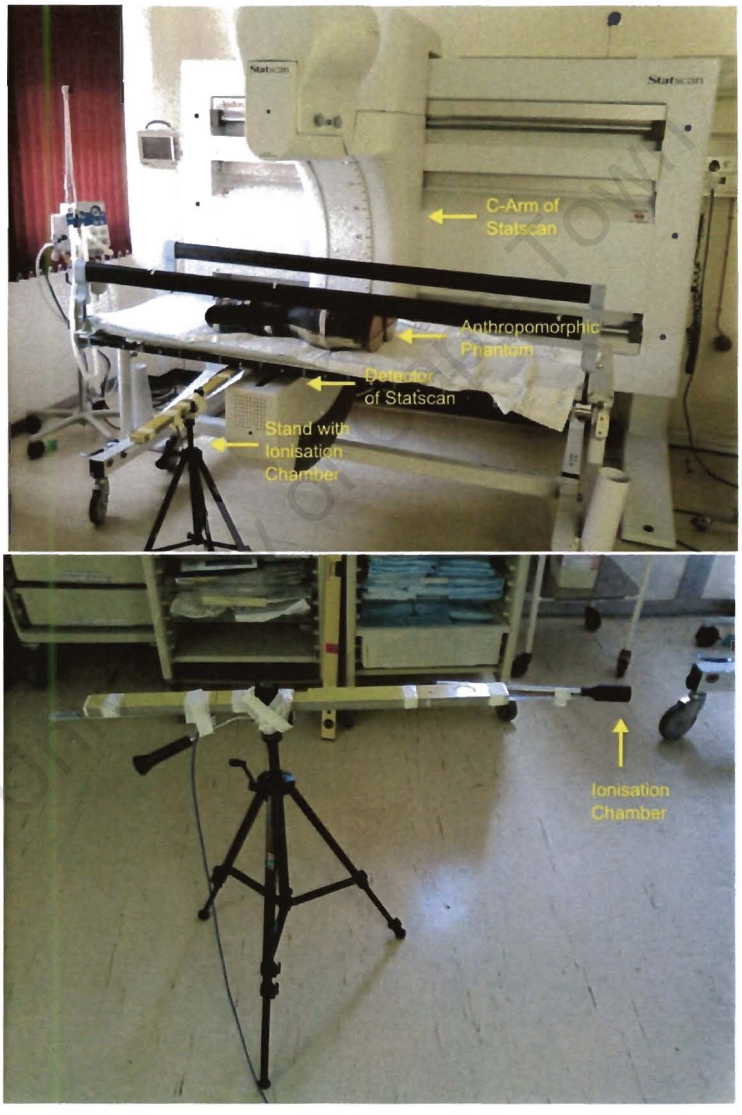

Table 4.9 compares the Statscan doses with those reported by the Health Protection Agency (HPA) (previously the National Radiological Protection Board (NRPB))(Hart and Wall, 2002) and the United Nations Scientific Committee on the Effects of Atomic Radiation (UNSCEAR2000) (United Nations Scientific Committee on the Effects of Atomic Radiation, 2000), and from other world wide studies (Begum, 2001; Compagnone et al., 2005; Papadimitriou et al., 2001). The UNSCEAR doses are those reported for the UK population.

The dose measurements with a phantom present includes scatter that does not reach the detector as a result of the detector moving with the beam while the dose meter was stationary. The measurements included in Tables 4.7 and 4.8 and the calculation of effective dose are not affected because no phantom is used in these measurements. The air doses above the detector with a standard sized anthropomorphic phantom present are 6 μGy for Chest AP, 10 μGy for Abdomen AP and 5 μGy for Pelvis AP.

This chapter presented the methods used to calculate dose for adult and paediatric patients and the results obtained. Further entrance dose measurements for all patient sizes available on Statscan are included in Appendix A. The following chapter discusses the meaning and implications of these results as well as further verifying the methods used in this study.

Table 4.7: 2007 Statscan doses for medium-sized patients.

Procedure Name	Tube Voltage (kV)	Slit width (mm)	Focal spot	Tube Current (mA)	Scan speed (mm/s)	FSD (cm)	Field size X (cm)	Field size Y (cm)	Air dose at detector (mGy)	Entrance dose (mGy)	E (uSv)
Full body AP	110	0.4	S	160	140	98.00	37.00	174.00	0.089	0.12	99
Chest AP	100	0.4	S	80	70	99.30	33.50	30.00	0.077	0.099	22
Chest PA*	100	0.4	S	80	70	99.30	33.50	30.00	0.077	0.099	15
Chest Lat	120	0.4	S	125	70	72.40	19.00	30.00	0.16	0.28	28
Abdomen AP	100	0.4	S	200	70	98.00	35.00	37.50	0.19	0.24	80
Abdomen Lat	110	1.0	L	200	35	72.40	19.00	34.00	1.1	1.9	160
Pelvis AP	100	0.4	S	200	70	98.00	36.50	28.20	0.19	0.25	60
Pelvis Lat	110	0.4	S	200	70	72.40	20.50	27.00	0.23	0.39	26
Skull AP	110	0.4	S	160	70	93.50	15.90	19.50	0.18	0.24	6.9
Skull Lat	100	0.4	S	160	70	80.40	18.50	20.00	0.15	0.24	6.5
C Spine Lat	90	0.4	S	160	70	72.40	11.50	14.00	0.13	0.22	2.1
Full Spine Lat	135	1.0	L	200	70	72.40	12.20	71.00	0.75	1.3	190

*Chest PA is not used at Groote Schuur Hospital due to trauma setting but is available on Statscan

Table 4.8: 2007 Statscan doses for extra large patients.

Procedure Name	Tube Voltage (kV)	Slit width (mm)	Focal spot	Tube Current (mA)	Scan speed (mm/s)	FSD (cm)	Field size X (cm)	Field size Z (cm)	Entrance dose (mGy)	E (uSv)
Full body AP	145	0.4	L	200	140	95.00	45.50	200.00	0.24	220
Chest AP	140	0.4	S	160	70	95.00	39.50	35.00	0.36	90
Chest PA*	140	0.4	S	160	70	95.00	39.50	35.00	0.36	56
Chest Lat	140	1.0	L	125	70	68.00	23.00	34.50	0.94	80
Abdomen AP	120	1.0	L	200	70	95.00	42.00	42.50	0.83	260
Abdomen Lat	130	1.0	L	200	35	68.00	25.00	37.00	2.6	190
Pelvis AP	120	1.0	L	200	70	95.00	45.00	32.50	0.82	200
Pelvis Lat	130	1.0	L	200	70	68.00	20.00	30.00	1.3	67
Skull AP	120	0.4	L	200	70	93.50	19.60	22.20	0.35	8.6
Skull Lat	110	0.4	L	200	70	80.40	25.00	22.30	0.35	8.9
C Spine Lat	110	1.0	L	200	70	68.00	14.50	14.60	0.99	9.5
Full Spine Lat	145	1.0	L	200	70	68.00	14.20	79.00	1.5	170

*Chest PA is not used at Groote Schuur Hospital due to trauma setting but is available on Statscan

Table 4.9: Comparison of 2007 Statscan effective doses (μSv) with those from other studies.

Examination	Statscan (2007)	UNSCEAR (UK) (2000)[a]	NRPB (UK) (2002)[b]	Italy (2005)[c]	Greece (2001)[d]	Bangladesh (2001)[e]
Chest PA	15	20	16	23 ± 8	40	62.2 ± 52.3
Chest Lat	28	40	-	47 ± 26	-	-
Abdomen AP	80	700	760	321 ± 107	-	-
Pelvis AP	60	660	670	386 ± 90	480	626.9 ± 208.9
Skull AP	6.9	30	-	20 ± 6	-	32.6 ± 28.8
Skull Lat	6.5	10	-	11 ± 3	-	24.9 ± 22.2
Full Body AP	99	-	-	-	-	-

[a] United Nations Scientific Committee on the Effects of Atomic Radiation (2000)
[b] Hart and Wall (2002)
[c] Compagnone et al. (2005)
[d] Papadimitriou et al. (2001)
[e] Begum (2001)

5

Dose measurement: analysis

This chapter discusses the measurements taken for adult and paediatric patients and develops reasons for the low doses obtained with LSSR.

This chapter contains extracts from the papers: *Maree G, Irving B, and Hering E. Paediatric dose measurement in a full-body digital radiography unit. Ped. Radiol. 2007; 37:990-997* and *Irving B, Maree G, Hering E and Douglas T. Radiation dose from a linear slit scanning X-ray machine with full body imaging capabilities. Radiat. Prot. Dosim. 2008; (in press).*

5.1 Discussion of paediatric doses

Comparisons were made between E and entrance dose measured for LSSR and conventional full-field X-ray machines for paediatric patients. These measurements were also compared to other worldwide studies (see Chapter 4).

It is clear from Table 4.5 and Figure 4.1 that, in general, the effective doses measured from the Statscan unit were considerably lower than those measured on the Shimadzu unit at the Red Cross Children's Hospital, as well as other recent effective dose measurements from around the world. The most accurate comparison can be made between the Statscan and Shimadzu units because the same field sizes, Monte Carlo simulator and apparatus were used, while other studies compared used different methods of obtaining effective dose.

The low dose from the Statscan unit is highlighted in Figure 4.1. The effective dose range measured on the Statscan unit for the AP skull examination was 2.6 to 4.1 μSv while that on the Shimadzu unit was 30.4 μSv; in other recently published studies the values are in the range 11 to 15 μSv (Table 4.5). The effective doses from chest scans on the Statscan unit, however, were not lower than in other studies. The AP chest examination on the Statscan unit had an effective dose range of 5.2 to 18.1 μSv, lower than the effective dose measured on the Shimadzu unit of 24.9 μSv, but in the same range as in recent international studies in which the values ranged from 5$\pm$2 μSv (Compagnone et al., 2005) to 16 μSv (Gogas et al., 2003). The effective doses on the Statscan unit for the AP abdomen and AP pelvis examinations, on the other hand, were considerably lower than the results in most of the other studies and were roughly 10% of the doses from the same examinations using the Shimadzu unit. The Statscan unit offers a full-body scan. For 5-year-old children the effective doses measured for the full-body scan were in the range 29.4 to 82.0 μSv, depending on technique factors set on the unit. The effective doses from full-body scans have not been measured in other studies in children. However, the effective dose from a full-body scan on the Statscan unit falls into the same range as those of pelvic and abdomen scans on other radiography units (Table 4.5). The ICRP (1991) has set a maximum radiation dose of 1 mSv per year for the general public. Although this does not include medical exposures, the total dose from ten full-body Statscan scans in a year does not exceed this limit.

The calculated effective doses for the standard trauma imaging protocol at the Red Cross Children's Hospital are shown in Table 4.6. The effective dose from the Statscan unit was less than half the dose from the Shimadzu unit. Thus, the Statscan unit has the potential to considerably reduce the radiation dose to children with trauma.

The Statscan unit is aimed at trauma patients; an AP projection for the chest is used because the patient cannot be turned. For a 5-year-old child the AP chest examination dose was found to be in the range of 5.2 to 18.1 μSv (see Table 4.5) using the Monte Carlo simulator PCXMC. If the same technique factors and entrance dose are used, but the projection is changed to PA, the dose range is between 3.4 and 12.2 μSv. Thus, there is a dose saving of over 30% by using the PA instead of AP projection for chest examination. The comparative studies shown in Table 4.5 used PA chest projections or a combination of PA and AP chest projections, reducing dose. This also explains why dose reduction for chest examinations was less than for other scans on the Statscan unit and this means that the Statscan offers more dose reduction for non-trauma patients.

In order for effective dose values to hold any weight, an image quality comparison

between the radiography units needs to be made. A comprehensive study by Pitcher et al. (2008) compared the Shimadzu unit with the Fuji computed radiography system and the Statscan unit for children with trauma at the Red Cross Children's Hospital. A total of 23 children with trauma were imaged, and the image quality, diagnostic equivalence and clinical efficiency of the Statscan unit were independently evaluated by consultant paediatric radiologists. Pitcher et al. (2008) concluded there was good diagnostic equivalence between the image quality on the Statscan unit and computed radiography systems, and noted that the Statscan unit was superior for imaging of the trachea and main bronchi. They also noted that imaging on the Statscan unit was on average 13% faster, and offered improved efficiency by the use of full-body scanning.

Thus, the doses from most of the standard radiographic examinations are considerably lower than those from the computed radiography system at the Red Cross Children's Hospital and other studies worldwide. This Section therefore shows the potential of linear slit-scanning radiography systems to reduce dose for standard radiographic examinations in children.

5.2 Discussion of adult doses

The previous section discussed the dose measurements obtained for paediatric patients. This section extends the discussion to the adult doses.

As discussed earlier, any dose comparison between two radiography units requires an image comparison to be made. In the case of paediatric patients the image comparison was made by a parallel study by Pitcher et al. (2008) comparing the two X-ray machines used for the dose measurements. The adult doses were not compared directly to those of another unit but were compared to published dose data. A study comparing the image quality from Statscan to that of conventional radiography units for adult patients was carried out at Groote Schuur Hospital (Beningfield et al., 2003). Two radiologists used a seven-point comparative scale to compare the digital images from Statscan with conventional radiographs, for common diagnostic X-ray examinations of 26 patients. These scores ranged from -3 to 3 depending on whether the image quality on Statscan was inferior or superior to conventional radiography. the mean of the measurements was taken for each region. The best imaged region on Statscan was the mediastinum with a mean equivalence score of 0.346 (SD = 0.49) and the weakest was for the bony detail (trabeculae) with a mean equivalence score of -0.654 (SD = 0.81). The study concluded that Statscan showed both clinical and radiographic promise. A follow-up study in the USA and South Africa by Boffard

et al. (2006) compared the quality of images between Statscan and conventional radiography units. Radiologists and trauma surgeons analysed images from 115 adult trauma patients. The study concluded that the same amount of information was obtained from Statscan and conventional radiography images and that for the AP plane Statscan images can replace conventional images (Boffard et al., 2006). Further evaluation has also demonstrated Statscan's utility in the adult and the paediatric trauma settings (Douglas et al., 2008; van As et al., 2006).

At Groote Schuur Hospital, Statscan is used in a trauma setting where patients cannot be turned and an AP instead of a PA projection is used for imaging the chest; a PA projection can be used on Statscan for patients that can be turned. Using a Chest PA instead of a Chest AP on Statscan reduces E by 32% for a medium patient and by 38% for an extra large patient (see Table 4.7 and Table 4.8). Chest PA should, therefore, be used wherever possible on Statscan.

Table 4.9 shows that, for most examinations, the doses from Statscan are considerably lower than those obtained by UNSCEAR (United Nations Scientific Committee on the Effects of Atomic Radiation, 2000), the NRPB (Hart and Wall, 2002) and other published studies (Begum, 2001; Compagnone et al., 2005; Papadimitriou et al., 2001). Examinations that usually have a high dose using conventional X-ray machines are particularly low by comparison. One example is the AP Pelvis examination; E from Statscan is 9% of the UNSCEAR dose. Thus, more than ten AP Pelvis X-rays can be taken for the same dose as one X-ray on a conventional X-ray machine. A more tangible comparison is that of a return flight from Johannesburg to London which has an effective dose of roughly 75 μSv (Watson et al., 2005) compared to a Statscan Pelvis examination of 60 μSv. Full-body scanning is a key feature of linear slit scanning; E from an AP full-body scan is about 14% of an AP Abdomen X-ray on a conventional X-ray machine (United Nations Scientific Committee on the Effects of Atomic Radiation, 2000).The dose reduction reported in this study for adult examinations is consistent with that reported in the previous section for paediatric examinations.

Doses for extra large patients are greater than doses for medium patients, as expected, due to higher values kV and mA required for penetration of larger patients. On average, doses for extra large patients are double those for medium-sized patients.

Thus, this section has shown that for many standard examinations Statscan offers a considerably reduced dose compared to conventional X-ray machines for adult patients. Next it is important to determine the reasons for these low doses in order to determine ways to further optimise LSSR units.

5.3 Development of reasons for low doses

This section extends the discussion of Potgieter et al. (2005) on the reasons for the low dose of linear slit scanning radiography, considering Statscan especially. The geometrical reasons for low dose particularly are discussed in depth. This discussion appeared in *Irving B, Maree G, Hering E and Douglas T. Radiation dose from a linear slit scanning X-ray machine with full body imaging capabilities. 2008; (in press).*

The low effective doses reported, for most examinations, from linear slit scanning radiography can be explained by: the use of a digital detector, the low scatter to primary ratio (SPR) of slit scanning radiography, the geometry of linear slit scanning radiography and the use of higher than usual tube voltages.

Potgieter et al. (2005) approximate the dose reduction from the use of an efficient digital detector in Statscan to be 50%, due in part to better detective quantum efficiency (DQE) of digital detectors compared to screen film. Samei et al. (2005) and Samei and Flynn (2002) confirm that flat panel digital detectors have DQE's more than 2 times higher than computed radiography. However, they noted that the optical coupling that is required in metal oxide detectors, such as that used in Statscan, means that the DQE advantage of digital detectors over screen film and CR detectors is reduced (Samei et al., 2004, 2005). This dose saving is not based on slit scanning radiography and, therefore, there will not be any substantial dose reduction due to the detector when Statscan is compared to radiography systems with digital detectors.

Slit scanning offers a greatly reduced scatter-to-primary ratio (SPR) compared to conventional radiography, making the use of an anti-scatter grid unnecessary (Barnes et al., 1985; Samei et al., 2005; Scheelke et al., 2005). The SPR from Statscan with a 20cm water phantom present was found to have a linear dependence on the precollimator slit width, with a SPR of 0.06 at 0.5mm and an SPR of 0.1 at 1.0mm (Scheelke et al., 2005). In contrast Court and Yamazaki (2004) found scatter fractions of between 0.3 and 0.7 (equivalent to an SPR of between 0.4 and 2.3) for a conventional digital radiography unit with various grids and a 15cm perspex phantom present. This considerable difference in scatter between slit scanning radiography and conventional units with a grid is confirmed in other studies. Barnes et al. (1985) found that the SPR of a slot scanning chest unit with a precollimator of 0.5mm was 0.03, which they report as 30 times lower than for conventional radiography with a grid. Samei et al. (2005) also report considerable scatter reductions from slot scanning compared to the use of a grid with conventional full-field radiography. While still having a lower SPR than conventional radiography, the use of a 1 cm wide precollimator in the Samei et al. (2005) study means that a larger SPR is reported compared to other

slit scanning radiography units such as a 0.4 mm or 1 mm wide precollimator used on Statscan (Scheelke et al., 2005), providing the postcollimator is sufficiently collimated. Linear slit scanning and slot scanning are, therefore, very effective methods for scatter reduction.

The use of an antiscatter grid means that a greater dose is required for the examination due to the attenuation of primary radiation. There is large variation in primary transmission for different grids due to the grid characteristics and the tube voltage used in the examination. Studies have found the primary transmission of radiation to vary between 45% and 75% (Chan and Doi, 1982; Court and Yamazaki, 2004; Kalender, 1982) when using a grid. On Statscan, however, no grid is necessary and the ratio between the precollimator and postcollimator is chosen so that the entire primary beam is detected (Scheelke, 2005). Thus, there is a 25% to 55% reduction in dose for slit scanning compared to full field from not using a grid.

Conventional detective quantum efficiency (DQE) is used as a measure of the performance of the detector. System (or effective) detective quantum efficiency (SDQE), however, takes into account the performance of the whole system including SPR, primary beam transmission and detector performance (Samei et al., 2005). Scheelke et al. (2005) found that for LSSR the SDQE was approximately four times higher than for conventional radiography due to the SPR, transmission and detector DQE described above.

The beam geometry of linear slit scanning radiography also contributes to a lower dose as explained later in Section 5.3.1. Figure 5.1 and 5.2 show the differences in the beam geometry for linear slit scanning X-ray machines and conventional full-field X-ray machines. In conventional radiography, increasing the distance from the source (r) increases the beam area in both X and Y direction, explaining the $1/r^2$ dose attenuation with r. For LSSR, the dose is proportional to 1/r because the beam area only increases in the non-scanning direction (Y) with increasing r (Potgieter et al., 2005). This is verified experimentally by Potgieter et al. (2005) as well as in this study. When compared to the entrance dose, the dose in air measured at the detector without a phantom present shows very good agreement to the 1/r dose attenuation of LSSR. Table 5.1 shows the entrance dose and dose at the detector (from Table 4.7) as well as the distances at which these measurements were taken. The ratio of the doses and the ratio of the distances are calculated and compared. The ratio of the distances is shown to be very similar to the ratio of the doses and thus the 1/r rule holds for LSSR (further explanation is provided in Section 5.3.1). As a result of the difference in attenuation, a higher entrance dose is required in conventional radiography in order to obtain the same beam intensity at the detector. Assuming a typical FSD of 90cm and an FFD of 130cm this leads to an entrance dose reduction of 30% and an ef-

fective dose reduction of 15% for the same patient volume exposed (see Section 5.3.1).

Table 5.1: Verification of 1/r rule for LSSR.

Procedure Name	FFD (r_2) (cm)	FSD (r_1) (cm)	Air dose at detector (d_2) (mGy)	Entrance dose (d_1) (mGy)	d_1/d_2	r_2/r_1	ratio
Full body AP	126.5	98.00	0.089	0.12	0.74	0.77	0.96
Chest AP	126.5	99.30	0.077	0.099	0.78	0.78	0.99
Chest PA	126.5	99.30	0.077	0.099	0.78	0.78	0.99
Chest Lat	126.5	72.40	0.16	0.28	0.57	0.57	1.00
Abdomen AP	126.5	98.00	0.19	0.24	0.79	0.77	1.02
Abdomen Lat	126.5	72.40	1.1	1.9	0.58	0.57	1.01
Pelvis AP	126.5	98.00	0.19	0.25	0.76	0.77	0.98
Pelvis Lat	126.5	72.40	0.23	0.39	0.59	0.57	1.03
Skull AP	126.5	93.50	0.18	0.24	0.75	0.74	1.01
Skull Lat	126.5	80.40	0.15	0.24	0.63	0.64	0.98
C Spine Lat	126.5	72.40	0.13	0.22	0.59	0.57	1.03
Full Spine Lat	126.5	72.40	0.75	1.3	0.58	0.57	1.01

Other factors that also contribute to a lower dose include higher kVs used compared to conventional examinations. There is also the possibility that more quantum mottle is being accepted by radiologists in the image quality studies because quantum mottle is difficult to identify.

Unlike the considerable dose reductions of other examinations, chest examinations show doses only slightly lower than conventional examinations. Potgieter et al. (2005) explain this in terms of much lower scatter in the chest resulting in less of a difference in SDQE between LSSR and conventional radiography. Samei et al. (2005) verify this when comparing slot scanning and conventional radiography in regions of different density in the chest. They show the denser the region, the larger difference in SDQE between slot scanning and conventional radiography. Chest examinations also generally use a much larger FSD. This results in less of a dose saving due to the beam geometry of LSSR (see Section 5.3.1). Statscan also uses a higher kV than conventional systems for most examinations except the chest where high kV examinations are common.

5.3.1 Further derivation of geometrical reasons for low dose

This section derives the geometrical reasons for low dose which have been discussed earlier. This dose reduction is due to there being no magnification in the scanning direction because the fan beam is perpendicular to the detector. This leads to greater intensity at the detector for the same entrance dose compared to conventional radiography.

As shown in figure 5.1, the cross-sectional area of the beam increases in both the X and Y directions with increasing distance from the source for conventional radiography, while for LSSR the beam only increases in the non-scanning direction (Y). The focus-to-skin distance (FSD) is the distance from the focal spot to the patient surface, the focus-to-film distance (FFD) is the distance from the focal spot to the detector plane and the table-to-film distance (TFD) is the distance from the table top to the detector plane.

As shown in Figure 5.2, the beam width at the detector is related to the width of the beam at the entrance area by

$$l_2 = \frac{FFD}{FSD} l_1 \tag{5.1}$$

where l_1 is the width at the entrance area, l_2 is the width at the detector plane, FFD is the film-focus distance and FSD is the focus-to-skin distance.

Therefore, for conventional radiography, the cross sectional area of the beam at the detector is

$$A_2 = (\frac{FFD}{FSD})^2 A_1 \tag{5.2}$$

where A_1 is the beam area at skin entrance and A_2 is the beam area at the detector.

For a linear slit scanning radiography unit, the area does not increase in the scanning direction, therefore:

$$A_2 = (\frac{FFD}{FSD}) A_1 \tag{5.3}$$

Considering only the geometry (i.e. in a vacuum), the dose-area product (DAP) remains constant at any distance from the detector. Thus, because the DAP remains constant but the area increases, the dose in air (D_{A2}) at the detector is related to the entrance dose in air (D_{A1}) by

$$D_{A2} = D_{A1} (\frac{FSD}{FFD})^2 \tag{5.4}$$

for conventional radiography and

$$D_{A2} = D_{A1} (\frac{FSD}{FFD}) \tag{5.5}$$

for LSSR because of the relationship between D_A, DAP and cross sectional beam area.

Figure 5.1: The X-ray beam geometry and exposed volume in conventional radiography and LSSR for the same exposed entrance area.

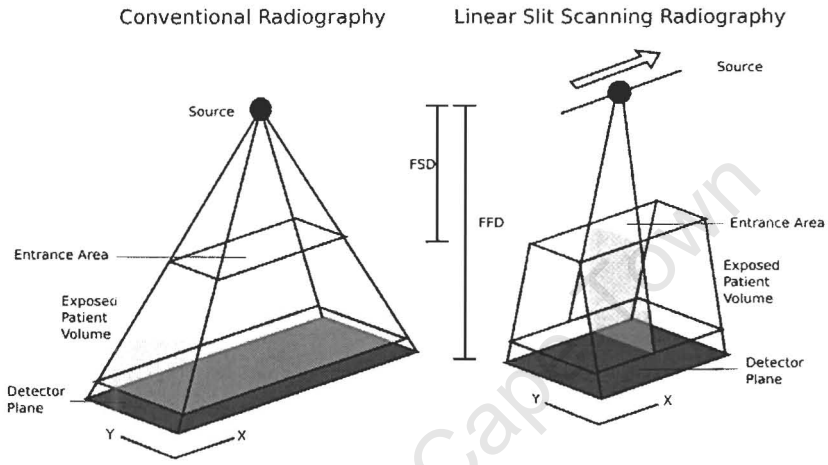

Figure 5.2: The difference in X-ray beam geometry between conventional full field radiography (where the beam width increases with distance) and LSSR in the scanning direction.

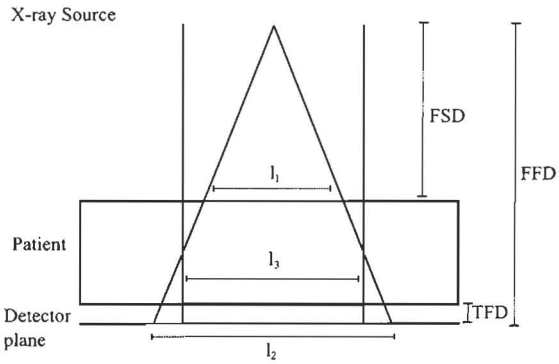

Thus, for LSSR the entrance dose in air at the patient surface can be reduced by a factor of

$$(FSD/FFD) \tag{5.6}$$

for the same D_A at the detector.

In order to calculate the effective dose saving, the same exposed patient volume must be considered (See Figure 5.2). Due to the beam geometry of LSSR, a larger entrance area needs to be exposed to obtain the same exposed patient volume and, therefore, the width of the scan needs to be increased by Δ to obtain the same volume as shown in Figure 5.2.

$$\Delta = \frac{1}{2} l_1 \left(\frac{FFD - TFD}{FSD} - 1 \right) \tag{5.7}$$

where TFD is the table-to-film distance.

Thus, the new scan length in terms of l_1 is

$$l_3 = \frac{1}{2} l_1 \left(\frac{FFD - TFD}{FSD} + 1 \right) \tag{5.8}$$

where l_3 is the scan length required by LSSR to obtain the same geometrically exposed volume as conventional full-field radiography.

The ratio between this new entrance area and the old entrance area is therefore:

$$\frac{l_3 w}{l_1 w} = \frac{1}{2} \left(\frac{FFD - TFD}{FSD} + 1 \right) \tag{5.9}$$

where w is the width of the entrance area.

If only the geometry is considered and, therefore, assuming that the effective dose weighting factors remain the same, the change in effective dose will be proportional to the change in the entrance area (Equation 5.9) as well as the change in entrance dose (Equation 5.6).

Thus,

$$E_{LSSR} = E_{conv} \left(\frac{FSD}{FFD} \right) \frac{1}{2} \left(\frac{FFD - TFD}{FSD} + 1 \right) \tag{5.10}$$

A simplification can be made by assuming that $TFD << FFD$, then:

$$E_{LSSR} = E_{conv}\left(\frac{FSD}{FFD}\right)\frac{1}{2}\left(\frac{FFD}{FSD}+1\right) \tag{5.11}$$

$$= E_{conv}\frac{1}{2}\left(1+\frac{FSD}{FFD}\right) \tag{5.12}$$

where E_{LSSR} is the effective dose for a linear slit scanning radiography unit and E_{conv} is the effective dose from a conventional full-field radiography unit.

The percentage dose saving for LSSR will then be

$$100\left(1-\frac{FSD}{FFD}\right) \tag{5.13}$$

for entrance dose and

$$100\left(\frac{1}{2}-\frac{1}{2}\frac{FSD}{FFD}\right) \tag{5.14}$$

for effective dose (which is half the dose saving of entrance dose)

Thus, the smaller the FSD and the larger the FFD, the greater the dose saving for LSSR compared to an full-field system with the same FFD and FSD. An increased TFD will also lead to a lower dose relative to conventional radiography.

Chapters 3 to 5 present and discuss dose measurements made for LSSR. The second part of this project is built on these measured doses and develops a model to predict doses. This model is discussed in the next chapters.

6 LSSR dose prediction: method

The previous chapters outlined and discussed dose measurements and calculations. Entrance dose (free-in-air) was measured directly using an ionisation chamber and E was generated using a Monte Carlo simulator. Measuring dose is time consuming and it is useful to have a model that can estimate these doses for each examination. As discussed earlier, the commercially available Monte Carlo simulators are designed to calculate E for conventional full field radiography units but can be applied to LSSR for conventional examinations. The disadvantage of a Monte Carlo simulator is that the calculation is slow. The current Monte Carlo simulators have also not been designed with LSSR in mind and therefore cannot make calculations for examinations where the technique factors are changed during the scan such as in the case of automatic technique factor control (ATFC). This chapter describes a method to model entrance dose and effective dose for LSSR, including for examinations such as ATFC where the technique factors vary during a particular examination.

6.1 Entrance dose modelling

Entrance dose (free-in-air) is simpler to model than effective dose. This is because entrance dose is a measurement of the tube output and does not depend on any of the patient characteristics.

This section discusses two ways of modelling entrance dose. Both methods have been incorporated into the dose prediction model as a cross check although only one is necessary. Verification of these methods is discussed in Section 7.1.

6.1.1 Entrance dose method 1: Spectrum generation model

The first method calculates the energy spectrum of the beam in terms of photon flux (Boone and Seibert, 1997); this spectrum is used to calculate entrance dose.

The spectrum is calculated using Equation 2.16 where the output is photon flux per unit mAs as a function of the energy of the photon; the photon energies are divided up into 1 keV wide intervals. This output needs to be multiplied by the mAs in order to obtain the total photon flux per unit energy. A typical energy spectrum output is shown in Figure 2.2.

The mAs is calculated for linear slit scanning radiography by multiplying the tube current (mA) by the effective exposure time given in Equation 2.19, i.e.

$$mAs = mA\frac{FSD}{FCD}\frac{\text{collimator width}}{\text{scan speed}} \tag{6.1}$$

The next step is to simulate attenuation of the beam through the filter. The attenuation of the X-ray spectrum is dependent on the energy of the photons, the type of material and the thickness of the material. A monochromatic X-ray beam attenuates by the following equation (Beutel et al., 2000, pg 25):

$$I = I_0 e^{-(\frac{\mu}{\rho})\rho x} \tag{6.2}$$

where $(\frac{\mu}{\rho})$ is the mass attenuation coefficient of the filter, ρ is the density of the filter and x is the thickness of the filter, as discussed in Section 2.1.3.4 (Beutel et al., 2000). This can be applied to an energy spectrum by applying this equation separately to each energy bin with its own attenuation coefficient (Beutel et al., 2000, pg 49). Usually intervals of 1 keV wide are used to model the beam i.e. the number of photons that are present between 0keV-1keV, 1keV-2keV, 2keV-3keV ... 149keV-150keV are counted separately. $(\frac{\mu}{\rho})$ for each photon energy and any element are available from NIST (2008).

The exposure can then be calculated from the photon flux by using the following equation(Beutel et al., 2000):

$$\xi(\varepsilon) = \frac{Photon flux}{Exposure} = \left[a + b\sqrt{\varepsilon}\ln(\varepsilon) + \frac{c}{\varepsilon^2}\right]^{-1} \quad (6.3)$$

where a, b and c are constants and ε is the energy of a particular bin. The derivation is described by (Beutel et al., 2000, pg 36). Therefore $1/\xi$ is multiplied by the flux and summed to give the exposure.

Exposure (X) refers to the amount of charge created from the ionisation of a mass of air and entrance dose (free-in-air) refers to the energy absorbed in a unit mass of air without backscatter (Section 2.1). Therefore, equation 2.6 is used to convert exposure to entrance dose as shown below:

$$\text{Entrance dose}(Gy) = 0.00876\ \text{X}(R) \quad (6.4)$$

This entrance dose is calculated for an FSD of 1m, which is the parameter used by Boone and Seibert (1997) to obtain the spectra. In order to correct this for the required distance, the 1/r attenuation rule for linear slit scanning is used (see Section 5.3.1). Therefore, the entrance dose is multiplied by a factor α that uses the 1/r rule to adjust the entrance dose from an FSD of 1m to the distance of interest:

$$\alpha = \frac{FSD_{1m}}{FSD_{true}} = \frac{1}{FSD_{true}} \quad (6.5)$$

Therefore, using this method, the entrance dose can be calculated from the technique factors provided for the examination. Part of Method 1 has been used to calculate entrance dose previously for Statscan (Alhamud, 2006; Scheelke, 2005).

6.1.2 Entrance dose Method 2: Polynomial exposure fit model

The second method uses an empirical formula (see equation 2.15) derived by Boone and Seibert (1997) to calculate the exposure per unit of tube current (mR/mAs) as described in Section 2.3.

$$mR/mAs = a_0 + a_1 kV^1 + a_2 kV^2 + a_3 kV^3 \quad (6.6)$$

The coefficients a_0 to a_3 are dependent on filtration and, therefore, simulation of the filter is not necessary. Exposure can then be converted to entrance dose for the correct FSD using equations 6.4 and 6.5 as described for Method 1.

6.2 Effective dose modelling

This section describes the development of a model to estimate effective dose (E) for LSSR (including ATFC). The model incorporates a number of different published methods and applies elements of theory discussed by Gkanatsios and Huda (1997), Huda and Gkanatsios (1997) and Huda et al. (1997). The model developed in this section estimates the energy spectrum, entrance dose, equivalent dose and effective dose. Organ energy absorption data are provided by Monte Carlo simulations and stored in a database in the programme. This method takes into account different patient sizes by using the relationship between energy absorbed (ϵ) and E (see equation 6.7). Energy absorbed is estimated using polynomials from Boone (1992) (see equation 6.8). This model does not perform Monte Carlo simulations, making it faster than a Monte Carlo simulator. In this section, the key concepts and theory are introduced first and then the outline of the model is provided.

6.2.1 Introduction to key concepts used in the model

6.2.1.1 Huda and Gkanatsios energy derivation and effective dose relation

Huda and Gkanatsios (1997) derived a relationship between the effective dose and the mass of the patient based on the energy absorbed in the patient. This relationship is useful because it can be used to estimate how the effective dose varies for patients of different sizes undergoing the same examination.

Energy absorbed (ϵ) is the energy transferred from a beam of ionising radiation to a volume of material. Huda and Gkanatsios (1997) showed that the relationship between ϵ and E is as follows:

$$E = \epsilon \times (E/\epsilon)_i \times \frac{M_i}{M} \tag{6.7}$$

where $(E/\epsilon)_i$ is the conversion coefficient between ϵ and E for the standard patient size and M_i is the mass of the standard sized patient. This conversion coefficient is still dependent on the energy spectrum (Φ) and the scan position. Therefore, if $(E/\epsilon)_i$ is known and the beam and scan position remain unchanged, ϵ can be generated for a different patient size and used to estimate E for that patient. This simple relationship exists because the relative radio sensitivity of any organ remains constant with age and size (Huda and Gkanatsios, 1997). Thus, the effective dose is directly proportional to the energy density (ϵ/M) of the exposed region, provided the energy spectrum is the same.

If the model described above were to be used to adjust the E for various patient sizes, then ϵ for both the initial patient size and the new patient size would have to be known.

6.2.1.2 Boone energy absorbed in the body

Boone (1992) used a Monte Carlo simulator to calculate the percentage of energy absorbed by a water phantom of various thicknesses from a range of photon energies and fitted this data to 8th order polynomials. These percentage energy absorption polynomials ($\eta(\varepsilon)$) give the percentage of energy absorbed from a monochromatic X-ray beam of energy ε in water phantoms of various thicknesses:

$$\eta(\varepsilon) = \sum_{n=0}^{8} A_n \varepsilon^n \tag{6.8}$$

where ε is the energy of the X-ray beam and A_n are coefficients that are dependent on the thickness of the phantom. A_n are provided by Boone for phantoms of 5cm to 35cm in increments of 5cm. The polynomials can be interpolated, if necessary, to obtain absorbed energies for phantom thicknesses different to those given.

The percentage energy absorption for a polychromatic energy spectrum can be derived using (Boone, 1992):

$$\eta_{Tot} = \frac{\int \Phi(\varepsilon)\eta(\varepsilon)\varepsilon d\varepsilon}{\int \Phi(\varepsilon)\varepsilon d\varepsilon} \tag{6.9}$$

where $\Phi(\varepsilon)$ is the photon flux and $\eta(\varepsilon)$ is the percentage of energy absorbed at energy ε. Therefore, the numerator is the total energy absorbed multiplied by 100, the denominator is the total energy in the beam and η_{Tot} is the percentage of energy absorbed.

Alternatively, the total energy absorbed can be calculated from the numerator

$$\epsilon = \frac{1}{100} \int \Phi(\varepsilon)\eta(\varepsilon)\varepsilon d\varepsilon \tag{6.10}$$

where the beam characteristics are taken into account by $\Phi(\varepsilon)$ and the patient thickness is taken into account by $\eta(\varepsilon)$.

Boone's percentage absorption polynomials were also used by Gkanatsios and Huda (1997) to model the change in effective dose.

Water equivalent tissue thickness of a patient needs to be included in this calculation because Boone (1992) simulated water phantoms. The water equivalence of a particular patient is the volume of water that results in the same photon flux exiting the phantom. The density of water is, however, very close to the density of most regions of the body (Theocharopoulos et al., 2006).

Therefore, the amount of energy imparted to tissue of any volume can be calculated. This can now be used to calculate how E changes for different patient sizes. In order to do this, however, patient surface areas and thicknesses need to be worked out. These can be measured but is preferable in a clinical setting to estimate them from more easily obtained patient parameters such as height and weight.

6.2.1.3 Patient dimensions

In order to obtain the patient thickness and surface area for a new patient size, a standard model of a patient is used based on height and mass. This is based on a patient model suggested by Servomaa and Tapiovaara (1998) who use the following conversion for different sized patients in their Monte Carlo simulator.

Lengths in the direction of the patient length are scaled by a factor of

$$S_z = \frac{h}{h_O} \tag{6.11}$$

where h is the new patient height and h_O is the old patient height.

Lengths in the direction of patient width or thickness are scaled by

$$S_{xy} = \sqrt{\frac{h_O M}{h M_O}} \tag{6.12}$$

where M is the new patient mass and M_O is the old patient mass.

These adjustments were used to calculate the new patient thickness (Z_2) and surface area (A_2) by scaling the reference patient values Z_1 and A_1.

$$A_2 = A_1 \frac{h}{h_O} \sqrt{\frac{h_O M}{h M_O}} \tag{6.13}$$

$$Z_2 = Z_1 \sqrt{\frac{h_O M}{h M_O}} \tag{6.14}$$

Therefore, new patient dimensions can be calculated based on the mass and height of the patient.

Equations 6.7-6.14 allow E for a particular examination on one patient to be used to calculate the E for the same examination on a different patient. This means that E only needs to be calculated for a standard sized patient and can then be used to calculate effective dose for other patient sizes. E for the standard patient is dependent on the characteristics of the examination, including the type of examination and the beam energy spectrum.

6.2.1.4 Slice dependant organ absorption coefficients

The next step is to build a model that can be used to generate effective doses (E) for a standard sized patient (mass 71 kg and height 174 cm) when the various technique factors and examination type are input. This means that the equivalent dose (H_T) to many of the organs needs to be determined; these are the organs included in the definition of E by the ICRP (1991).

The Monte Carlo simulator PCXMC can be used to generate the average energy absorbed in each of the organs from photons in each energy interval. This was used to generate a database of organ absorption coefficients ($\theta_{organ}(\varepsilon, P)$) to be used in any calculations of effective dose. The organ absorption coefficients used in this model were generated by dividing the surface area of a standard patient into 1 cm thick slices and exposing each of these slices individually to a range of photon energies. For each iteration, energy absorption coefficients were generated for all the organs in the body and stored as a database. The organ absorption coefficients from a particular organ and a particular exposed slice represent how much energy on average is absorbed by that organ from a photon of each energy (1 keV to 150 keV in bins of 1 keV). This is illustrated by an example in Figure 6.1, which shows how much energy on average is absorbed by the lungs from a photon as a function of the photon energy and the scan slice. The coefficients are over a localised area because very little radiation will be absorbed by the lungs if another region of the body other than the chest is exposed. Clearly, the highest photon absorption would take place in organs directly under the exposed area.

Figure 6.1: The energy absorption coefficients for the lung as a function of photon energy and position.

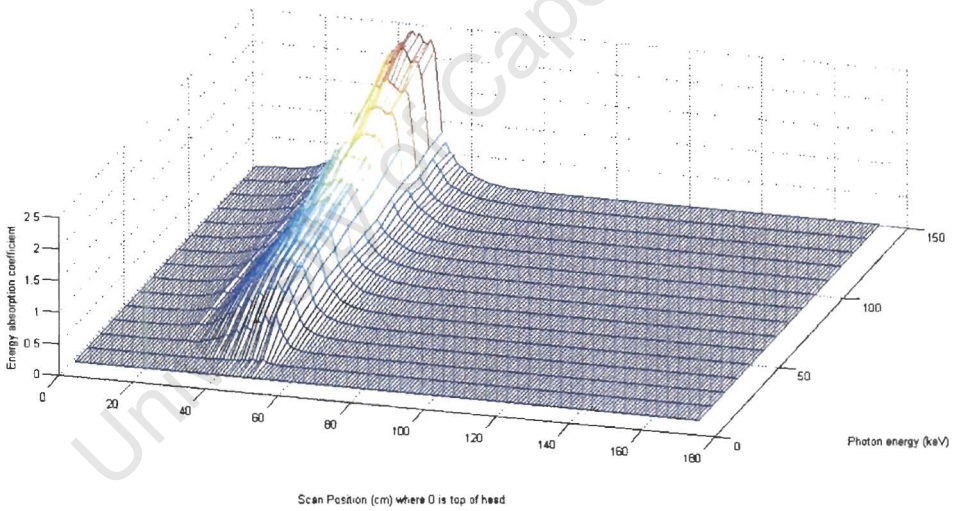

$\theta_{organ}(\varepsilon, P)$ can then be multiplied by the energy spectrum used for that particular beam slice and added up to obtain how much energy is absorbed by a particular organ in one slice. The energy absorbed by an organ in each of the slices is then added up to obtain the total energy absorbed by each organ. H_T can be calculated for each organ by dividing the energy absorbed by the mass of that organ (ICRP, 1991). The organ masses of a medium patient (71 kg and 174 cm) are shown in Table 6.1 (M Tapiovaara, STUK, email communication, 2007). Effective dose can be calculated by multiplying the dose to each organ by its weighting factor shown in Table 2.1 (ICRP, 1991).

Table 6.1: PCXMC organ masses for a standard patient.

Organ / Tissue	Mass (g)
Lungs	999
Heart	300
Breasts	302
Liver	1810
Stomach	150
Spleen	174
Kidneys	284
Pancreas	89.5
Small Intestine	1040
Gall bladder	62.9
Upper large intestine	209
lower large intestine	158
Urinary bladder	45.1
Uterus	65.4
Adrenals	15.5
Thymus	19.8
Oesophagus	39.7
Thyroid	19.6
Brain	1350
Testes	37.1
Ovaries	8.27
Skin	2860
Bone Marrow	1120
Skeleton	9516
Remainder (muscle and fat)	49304
Total	71100

Thus, the calculation of E for a standard sized patient from the energy absorption coefficients can be summarised as follows:

1. Generate energy spectrum ($\Phi(\varepsilon)$) depending on the technique factors of each particular slice.
2. Obtain flux of each photon energy interval.
3. Multiply energy absorbed in each organ by a particular photon ($\theta_{organ}(\varepsilon, P)$) by flux of that photon.
4. Sum total of energy absorbed by each photon interval to give the total organ energy.
5. Divide by mass of each organ to obtain organ doses.
6. Multiply with weighting factors and sum to obtain effective dose for a slice.
7. Sum E for all the slices exposed in the scan to obtain the total effective dose.

This algorithm can be illustrated as a formula:

$$E_{SP}(\Phi, P) = \sum_{organs} \left[\frac{\int \Phi(\varepsilon, P)\ \theta_{organ}(\varepsilon, P)\ d\varepsilon}{M_{organ}} \omega_{organ} \right] \qquad (6.15)$$

where E_{SP} refers to the effective dose for one slice to a patient of standard size, ω_{organ} is the weighting factor for each organ, M_{organ} is the mass of each organ, $\theta_{organ}(\varepsilon, P)$ is the average energy absorbed by a particular organ from a photon of energy (ε) and a beam slice of position (P). $\Phi(\varepsilon, P)$ is the photon flux; Φ is only a function of P if the ATFC procedure is used where the technique factors are varied during the scan.

The methods discussed in the previous sections can be incorporated into a programme to calculate effective dose for any patient and procedure.

6.2.1.5 The combination of these methods

The effective dose for a standard sized patient (E_{SP}) can be generated from Section 6.2.1.4. By modifying Equation 6.7 the effective dose for any sized patient can be calculated from the dose to the standard patient as shown in Equation 6.17.

Equation 6.7 is shown again as Equation 6.16 (note the distinction between ϵ which refers to the total energy imparted in a region of the body and ε which is the energy of a particular photon).

$$E = \epsilon \times (E/\epsilon)_i \times \frac{70.9}{M} \qquad (6.16)$$

Therefore, Equation 6.16 can be rewritten as:

$$E = \frac{\epsilon(\Phi, Z_j, A_j)}{\epsilon(\Phi, Z_i, A_i)} \frac{70.9}{M} E_{SP}(\Phi, \text{Scan type}) \tag{6.17}$$

where i refers to the parameters of a standard patient and j are the factors of the required patient size. ϵ is the energy imparted. Thus, the effective dose is dependent on five factors: patient thickness (Z), patient mass (M), scan area (A), energy spectrum (Φ) and scan type.

6.2.2 Method of dose prediction for LSSR including ATFC

This section outlines the structure of the whole model and shows where the elements introduced in Section 6.2.1 are incorporated. The aim of this section is to give an overview of the model without going into the mathematical and physical details that have already been outlined in Section 6.2.1.

ATFC is currently implemented by Lodox systems for the lateral full-spine examination. The scan speed and the tube voltage are varied during the examination. ATFC is particularly useful for the lateral full-spine examination due to the large changes in patient thickness and density in this examination; an example is the difference between the neck and the shoulder region. Therefore, for example, over the shoulder region the speed is decreased to obtain greater photon flux and the tube voltage is increased to obtain higher photon energies. Currently, a full body AP examination is first performed and, from this image, points of interest are selected such as the top of the shoulders. The ATFC profile is then fitted to these points of interest and the examination is performed (C De Sousa, Lodox Systems, email communication, 2007).

This model is suitable for both conventional and ATFC examinations. The model divides the beam used for the examination into 1 cm wide slices and calculates the effective dose generated by each of these slices individually before adding them up to give the effective dose for the entire examination. Considering a full body examination, for example, the examination is divided into slices moving down the body from the head to the toe. Photons scattered out of the directly exposed region are included. This approach is demonstrated in Figure 6.2, where beam slices of an exposed region are shown with one beam slice shown in bold. Beam slices are simulated next to each other so that every part of the beam surface area is covered by one of the 1cm wide beams.

Figure 6.2: A demonstration of the beam slice approach to modelling LSSR, where one of the slices is highlighted.

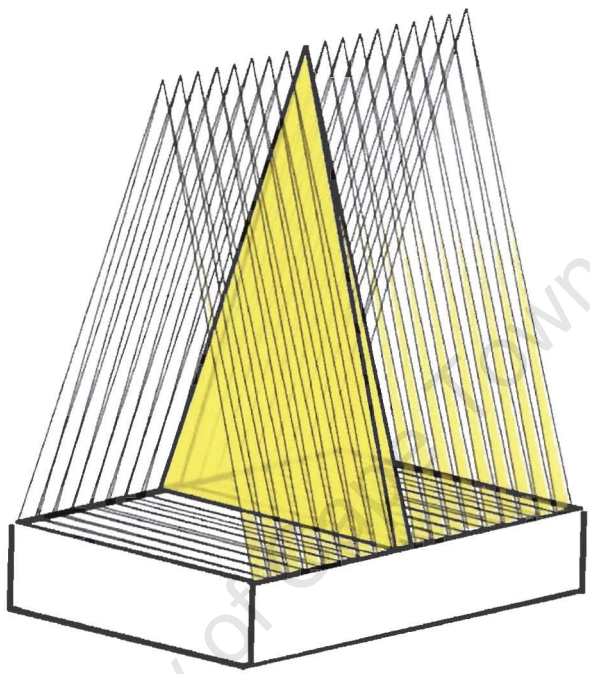

For each slice, the technique factors including tube voltage (kV), tube current (mA), scan speed, collimator width and focus-to-skin distance (FSD) are input to the model. These technique factors can be constant throughout the scan, or for ATFC, an array of data is provided which specifies how these technique factors change as the scan progresses.

The energy spectrum of the beam coming from the tube is generated from the technique factors using the method described in Section 2.3.1.3 and discussed earlier in this chapter. This is then attenuated through the defined filter (Section 6.1) to obtain the energy spectrum at the patient surface (i.e. the flux of photons of each energy at the patient surface).

The entrance dose is calculated using methods discussed in Section 6.1. Therefore, for each slice a calculated entrance dose value is generated using the input technique factors for that part of the body. As discussed in Section 6.1, two methods have been incorporated into the model for testing purposes but *Method 1* is used to calculate entrance dose

For each slice, the spectrum is multiplied with the standard sized patient energy absorption coefficients of each organ (Section 6.2.1.4) and summed to give the total amount of energy absorbed by each organ. This is divided by the mass of each organ (see Table 6.1) to give the dose to each organ. The organ doses are then multiplied by the organ weighting factors and added together to give the effective dose (E) for that slice for a standard patient (Section 6.2.1.4).

The next step is to calculate the effective dose for the patient size of interest. Two patient parameters are input, the height and the mass. These parameters are used along with standard patient dimensions to calculate the thickness and the scan area for the patient of interest for each 1cm slice (as discussed in Section 6.2.1.3). These values are used to calculate the energy imparted (ϵ) for a standard sized patient as well as the patient size of interest for the particular slice being calculated (Section 6.2.1.2). For the standard sized patient and the patient of interest particular percentage energy curves $\eta(\varepsilon)$ are generated. As discussed in Section 6.2.1.2, the polynomials specified by Boone (1992) to calculate these curves are only for certain thicknesses; weighted averages are taken of the two nearest curves to get the correct absorption curve for any thickness. Figure 6.3 shows the $\eta(\varepsilon)$ curves for a particular slice of a standard sized patient and a smaller patient. The two curves given by Boone (1992) are also shown for the two nearest thicknesses from which the $\eta(\varepsilon)$ curve for the smaller patient is calculated.

Figure 6.3: Energy absorption curve $\eta(\varepsilon)$ for a particular slice; the curve for the patient of interest is a weighted average of the Boone curves shown in the diagram.

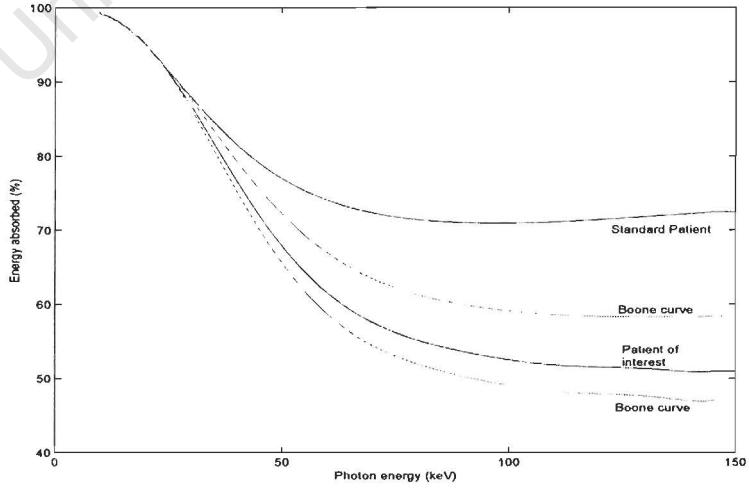

Multiplying these curves by the energy spectrum and the scan area gives the total amount of energy per photon energy transferred to a slice of a particular thickness and width of the patient. Where the volume under the curve or the integral gives the total energy imparted (ϵ) for that slice. Figure 6.4 shows the total energy absorbed in one particular slice per photon interval and the total energy entering the slice per photon interval. The difference between these curves is the energy that passes through the patient and reaches the detector.

Figure 6.4: The energy absorbed per photon bin in an example slice and the energy entering the slice per photon bin.

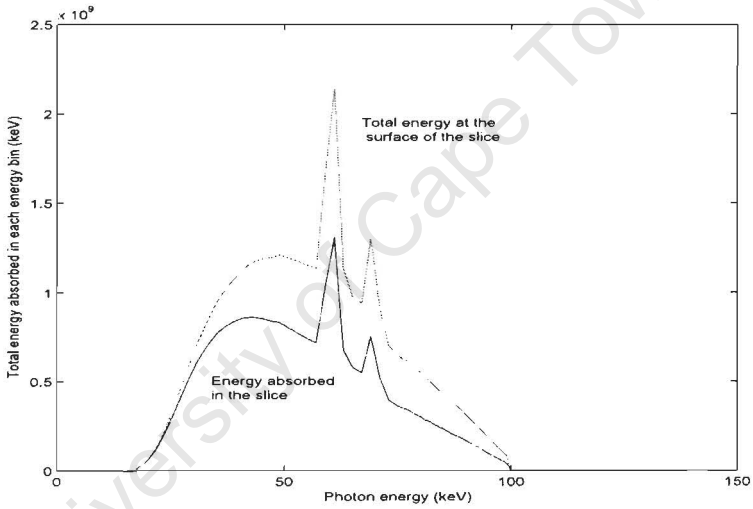

Note that the standard patient thickness throughout the body is taken into account. The ratio of ϵ for the patient of interest and the standard sized patient is then used to calculate E for the patient of interest from E for the standard sized patient (See Section 6.2.1.5). E from all the slices are then added together to give the total E for the examination.

A flow diagram of the programme is shown in Figure 6.5. The output of this model can be tested against existing programmes and measured data; this is discussed in the following chapter.

Figure 6.5: A flow diagram of the programme design for dose prediction.

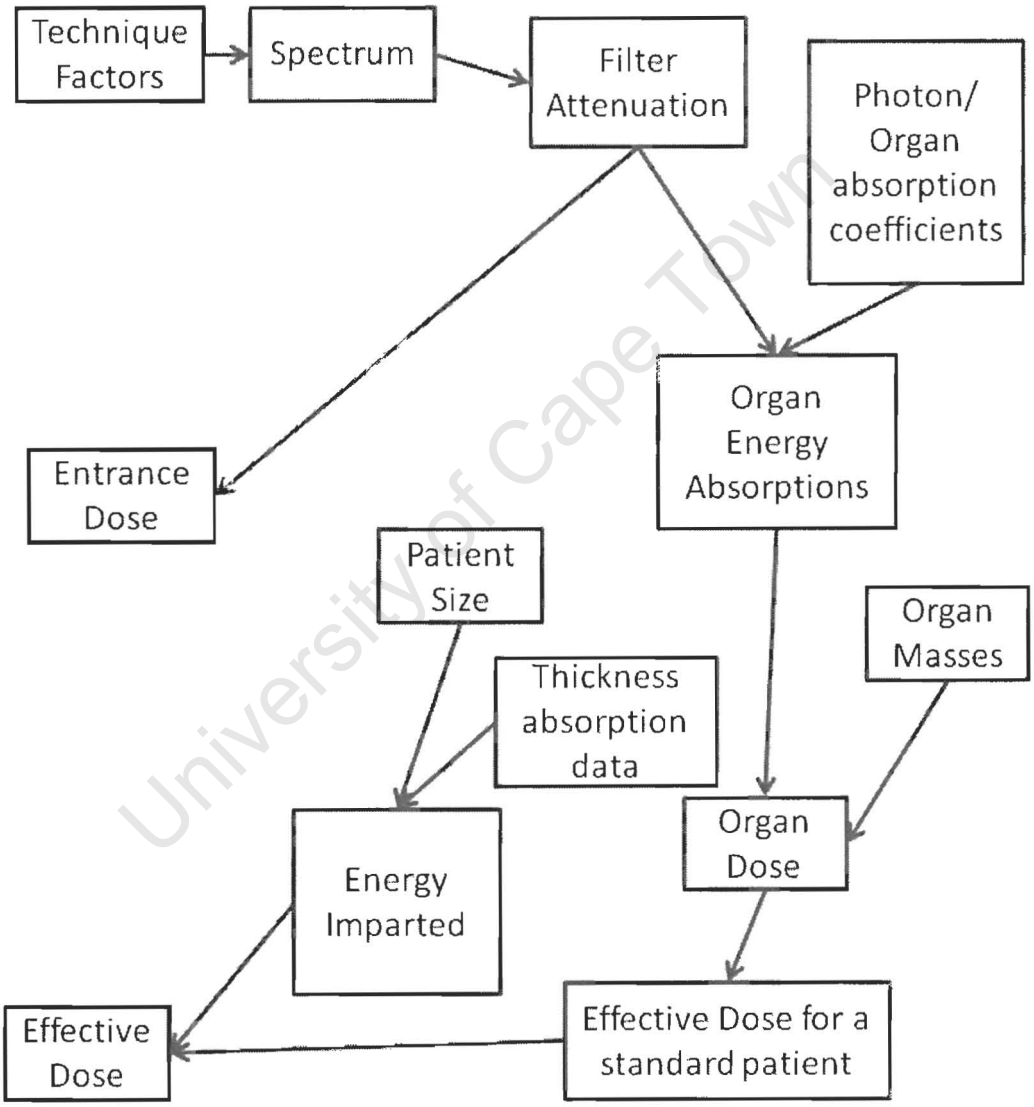

7

LSSR dose prediction: model verification and results

The last chapter developed a method to predict dose for linear slit scanning radiography units. This chapter compares the values generated using the developed method to measured data and other models.

7.1 Comparison between entrance dose models

Three entrance dose (free-in-air) prediction methods that were outlined earlier in Section 2.3.1 were compared. Two of these models (known as *Method 1*: Spectrum generation model and *Method 2*: Polynomial exposure fit model) have been included in the programme to produce alternative results and are discussed in more detail in Section 6.1. *Method 3*: Function fit model is also compared (see Section 2.3.1.1).

Briefly, from Sections 2.3.1 and 6.1, *Method 1* was developed by modelling the shape of the energy spectra (Boone and Seibert, 1997) and using these spectra to calculate dose. *Method 2* was developed by using polynomials that have been fitted to empirical X-ray tube exposure measurements by Boone and Seibert (1997). *Method 3* uses a function that includes the technique factors and two unknown parameters. These unknown parameters are fitted to entrance dose data from a particular radiography unit and in this study were fitted to previously measured entrance dose data from Statscan. All three methods have been adapted for LSSR and estimate entrance dose

(free-in-air) when the technique factors: tube voltage, tube current, filtration, scan speed, focus-to-distance and collimation width are input.

These models were built and then used to generate entrance dose (free-in-air) data using the same technique factors as the entrance dose measurements made for various patient sizes that were discussed in Chapter 4. The dose generated for each method and the measured entrance dose is shown in Table C.1 of Appendix C. The correlations between the various methods and the entrance dose data as well as the average percentage difference was found, and Bland and Altman plots (Bland and Altman, 1986) were used to compare the data.

The mean absolute percentage difference is described by equation 7.1 and is one way of determining the expected difference between any two values (Mélin et al., 2007)

$$MAPD = 100\frac{1}{N}\sum_{i=1}^{N}\frac{|y_i - x_i|}{x_i} \tag{7.1}$$

The mean absolute percentage difference between the measured data and each model was calculated as 4% for *Method 1*, 5% for *Method 2* and 14% for *Method 3*. Therefore, *Method 1* is the most accurate.

Correlations can also be performed on the measured data and the predicted data for the three methods. This yields a correlation coefficient of 0.99959 for *Method 1*, 0.99959 for *Method 2* and 0.99755 for *Method 3*. These are extremely high correlations but, as explained by Bland and Altman (1986), correlation coefficients can be misleading as they are a measure of the relationship between data sets and do not necessarily reflect differences in the measurements produced by the methods. These methods are compared graphically in Figures 7.1, 7.2 and 7.3.

The comparative plots shown in Figures 7.1, 7.2 and 7.3 plot the measured doses on the x-axis and the calculated doses on the y-axis. A line of equality is added to show where the values would fall if they were exactly equal. These graphs show that, considering the range of values, there is good agreement for all the methods between measured and predicted values. The Bland and Altman (1986) plots show the percentage difference between the measured values and the predicted values as a function of the measured values. Also included in these graphs are the mean percentage difference and the first standard deviation of the percentage difference. These graphs clearly show the deviation between measured and predicted. From the Bland and Altman plots it is clear that the first two methods have a much higher accuracy than the third, and the first method is the most accurate.

Figure 7.1: Comparison between measured data and results of Method 1.

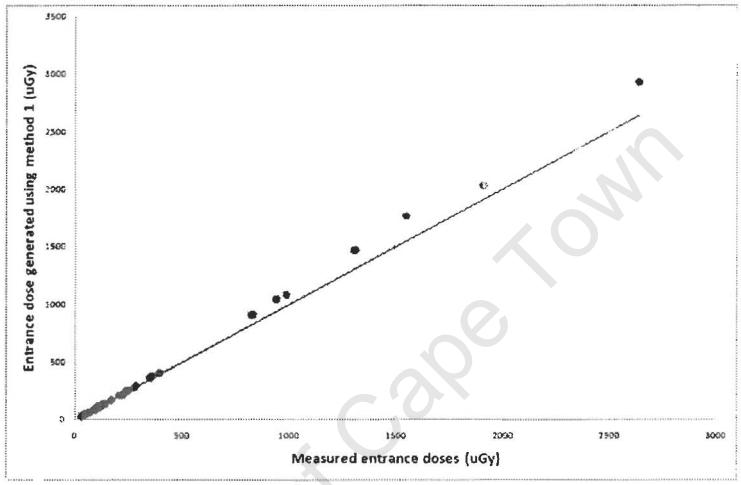

(a) Comparative plot

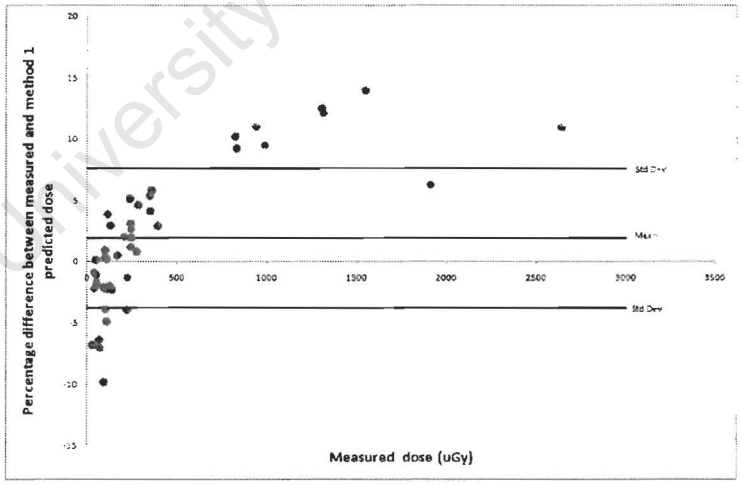

(b) Bland and Altman plot

Figure 7.2: Comparison between measured data and results of Method 2.

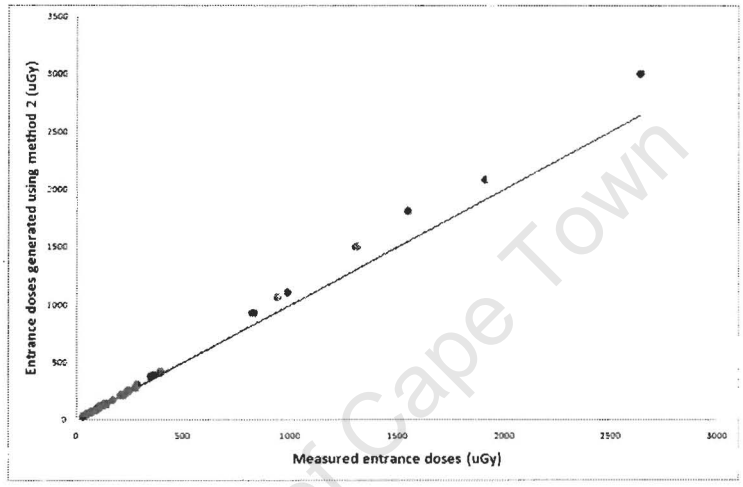

(a) Comparative plot

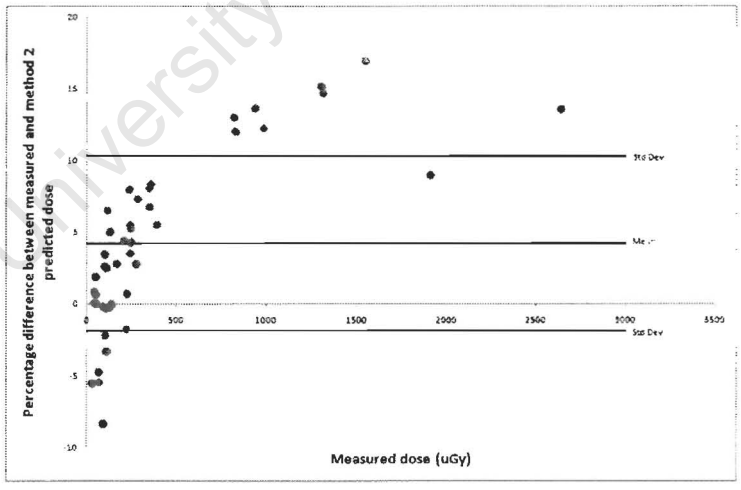

(b) Bland and Altman plot

Figure 7.3: Comparison between measured data and results of Method 3.

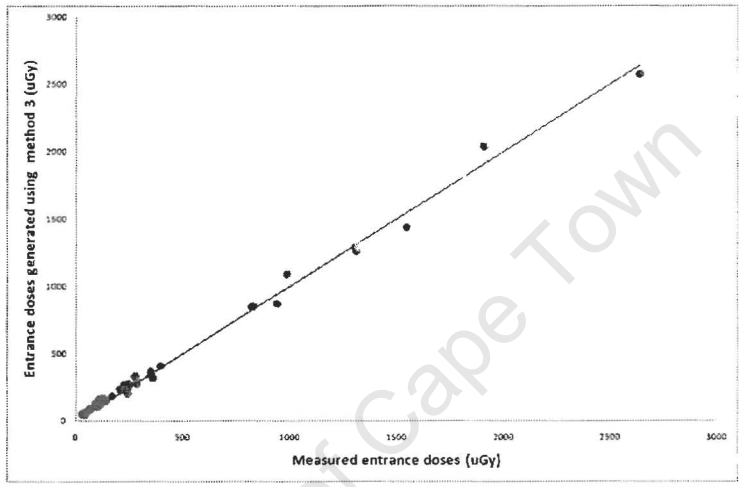

(a) Comparative plot

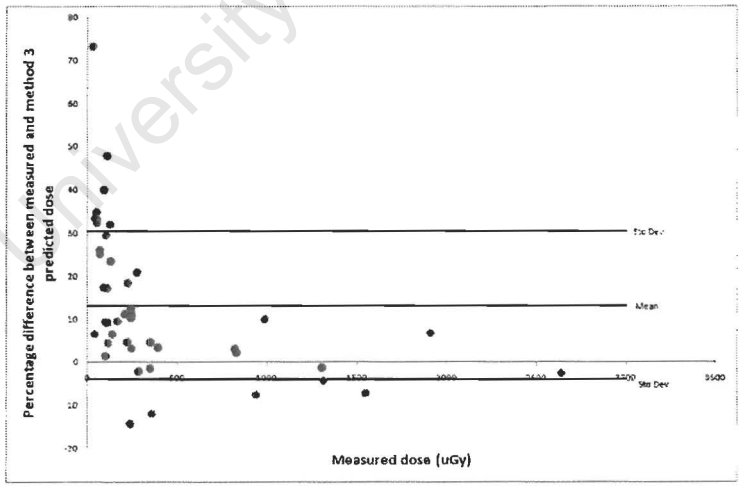

(b) Bland and Altman plot

The first two methods show the greatest difference between measured and predicted for very large values as well as for very small values, while the third method has the biggest variation for small values.

The first two methods show a fair degree of accuracy but the trend of overestimating higher doses (see Figures 7.1 and 7.2) shows that there is room to improve the model. From the technique factors used to generate these comparisons (see Table C.1 in Appendix C) it is clear that both Method 1 and Method 2 overestimate the dose at high tube voltages and underestimate the dose at low tube voltages. These two methods are both based on simulations by Boone and Seibert (1997) and, therefore, this difference could be accounted for by differences in tubes by Boone and Seibert (1997) and in Statscan. Boone and Seibert (1997) point out considerable differences exist between tubes. When developing their model they used a variable thickness of aluminium that was added to the model as a function of kV to take into account the tube differences when comparing to an existing model. This added aluminium was fitted from the output of the two models. A similar method could be used to obtain more accurate results for the model developed in this study. A small thickness of extra aluminium which increases with higher kV could be added to the model. The focal spot size is not taken into account by the new model developed in this study or by the Boone and Seibert (1997) model.

After the entrance dose (free-in-air), which only takes into account the tube output, has been verified, the effective dose (E) can be compared for different methods. E takes into account the energy spectrum of the beam and the patient parameters, as discussed in the previous chapter.

7.2 Incremental effective dose comparison

Effective dose (E) is generated, in the model developed in this study, using an incremental approach where the examination is broken into 1 cm slices for a medium sized patient (mass 71 kg, height 174 cm). This more closely approximates LSSR as discussed in Chapter 6. In order to make a comparison to equivalent data, similar increments were generated using the Monte Carlo simulator PCXMC and a key sending macro. These results were compared to increments generated by the model developed in this study. These increments for both methods were simulated using a tube voltage of 100 kV, 2mmAl filtration and an entrance dose of 10 mGy. A high entrance dose was used so that the values produced by PCXMC for each increment would have sufficient significant figures. The effective dose generated for each increment for a medium sized patient is shown in Table C.2 of Appendix C.

Figures 7.4 and 7.5 show E for each increment generated by PCXMC and the model developed in this study for a standard sized patient of height 174cm and mass 71kg. This data is for the whole body where increment 1 is the top of the head and increment 174 is the bottom of the foot. These figures show how the effective dose for each slice changes throughout the body for the same beam energy due to varying the sensitivity of the organs. This comparison was completed in order to validate the ability of the new model to calculate effective dose for each slice, and therefore the individual organ doses in each slice, accurately. The graphs show very little difference between doses generated by PCXMC and the new model. The total effective dose for sum of all the increments is 0.793 mGy and 0.802 mGy for PCXMC and the new model, respectively, for the AP projection and 0.213mGy and 0.207 mGy, respectively, for the lateral projection. Thus, the new model has 1.2% higher E for the AP projection and 2.8% less for the lateral projection than PCXMC under the simulated conditions. Only a small difference is expected because the new model uses organ energy imparted data that was originally generated by PCXMC. The main differences would arise due to differences in the spectrum generated. As discussed in Section 7.1, the energy spectrum varies for the same technique factors on different tubes. The accuracy of this model at simulating tube output is discussed in Section 7.1. PCXMC uses a different model to generate the energy spectrum which results in a slightly different E.

These simulations were also generated for extra small sized patients (mass 7 kg and height 75 cm) and extra large patients (mass 130 kg and height 200 cm) in order to verify that the dose to each slice is being appropriately scaled by the model as the patient size changes. These extreme patient sizes were used to determine the maximum error that will occur in the scaling. Figure 7.6 shows the results for extra small patients and Figure 7.7 for extra large patients for the AP projection. These graphs show a fairly good agreement between the dose predicted by PCXMC and the dose predicted by this model, especially considering the extreme patient sizes. The percentage difference for the total E of this model is 1% less for extra large patients and 11% more for extra small patients. These differences are primarily due to differences in the energy spectrum generated which is the same as for the medium patient. Further differences will arise due to the calculation of the energy imparted (ϵ) for each slice for the medium sized patient and the patient of interest as well as the adjustment of the effective dose using these ϵ values; this method is discussed in the previous chapter. This adjustment takes into how the energy density changes for the whole exposed region as the patient size is changed but does not take into account the difference in attenuation through the exposed region for different patient thicknesses i.e. deep organs of a larger patient will receive less dose relative to the energy density of the whole exposed region compared to smaller patients. This leads to a small error.

Figure 7.4: Effective dose per increment generated by PCXMC and the new model for the AP projection of a standard sized patient.

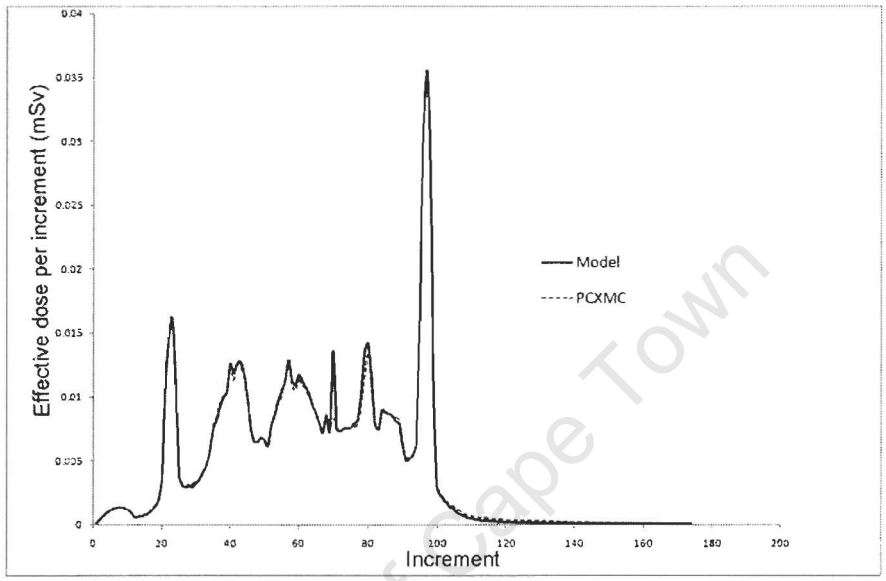

Figure 7.5: Effective dose per increment generated by PCXMC and the new model for the lateral projection of a standard sized patient.

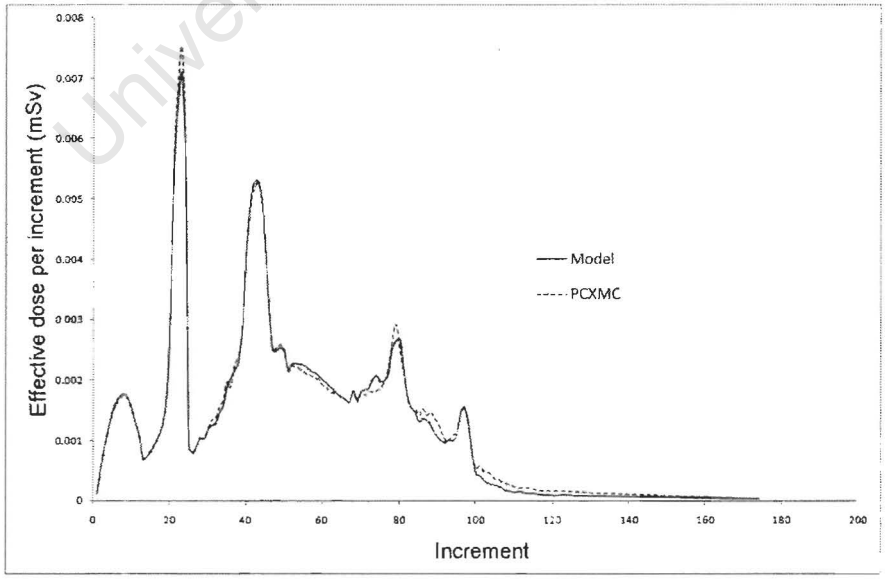

Figure 7.6: Effective dose per increment generated by PCXMC and the new model for the AP projection of a patient of mass 7kg and height 75 cm.

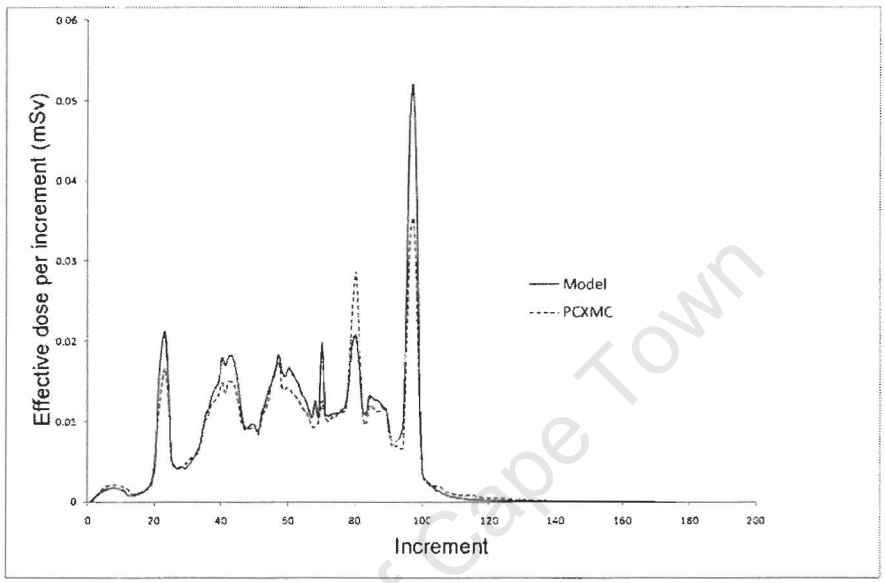

Figure 7.7: Effective dose per increment generated by PCXMC and the new model for the AP projection for a patient of mass 130kg and height 200 cm.

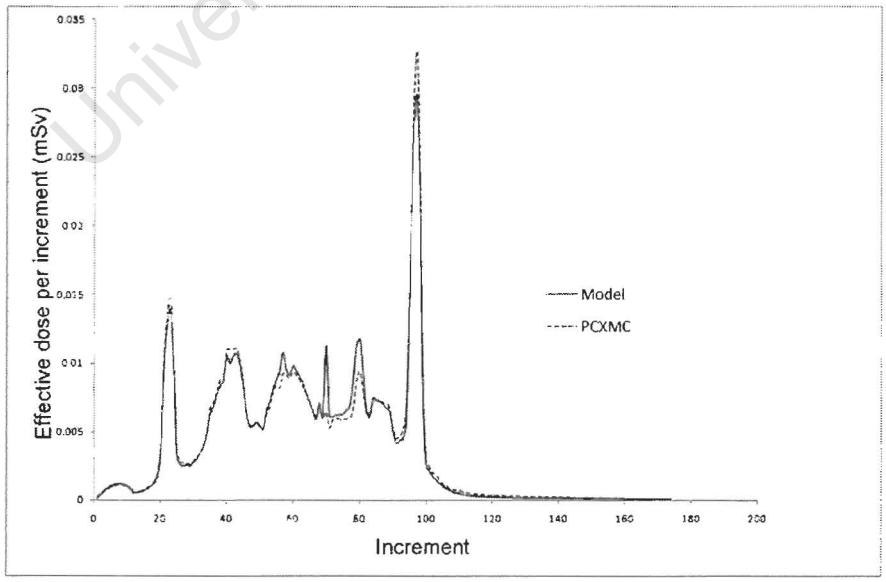

One of the key reasons for developing this model as discussed in the previous chapter is to increase the speed of the calculation when applied to LSSR. Dividing the examination up into slices and calculating each slice independently is a method of simulating LSSR and allows doses to be calculated for examinations where the technique factors vary through the examination. The difference in computational speed is shown during this comparison where effective dose slices for the whole body took over 6 hours to complete using PCXMC whereas the new model took under 10 seconds. This difference maybe partly attributed to PCXMC being a Monte Carlo simulator whereas the new model is partly based on data generated from previous Monte Carlo simulations and does not require any additional Monte Carlo simulations during the calculation. The difference in speed is also partly due to PCXMC not being designed for LSSR, which meant that a separate Monte Carlo simulation had to be performed for each slice and parameters input each time.

These comparisons verify the ability of this model to accurately calculate the effective dose for each region of the body but only considers one beam energy. Therefore, the response of this model to different beam energies must also be verified.

7.3 Effective dose as a function of beam energy

The previous section compared the model developed in this study to PCXMC in terms of patient size, organ sensitivity and scan position. As discussed earlier, Figures 7.4 to 7.7, show a comparison between PCXMC in terms of patient size, where different graphs simulated different patient sizes, organ sensitivity where similar peaks were generated for both models indicating sensitive organs; these results were related accurately to the position of the slice.

This section compares the results generated by this model for various beam energies by varying the tube voltage from 60 kV to 140 kV which is the range in which most examinations are performed on Statscan. Results for various regions of the body were generated and compared to results generated using PCXMC. The parameters used were a tube current of 100 mA, a speed of 140 mm/s, a slit width of 0.4 mm and an SSD of 95 cm. Figure 7.8 shows the results generated for the chest region and the abdomen/pelvis region. This comparison showed a similar trend for PCXMC and the new model. It is also clear from these simulations that increasing tube voltage for these examinations causes an increase in E, as expected for most examinations.

Figure 7.8: Effective dose calculated using PCXMC and the new model for different regions of the body, as a function of tube voltage for medium sized patients.

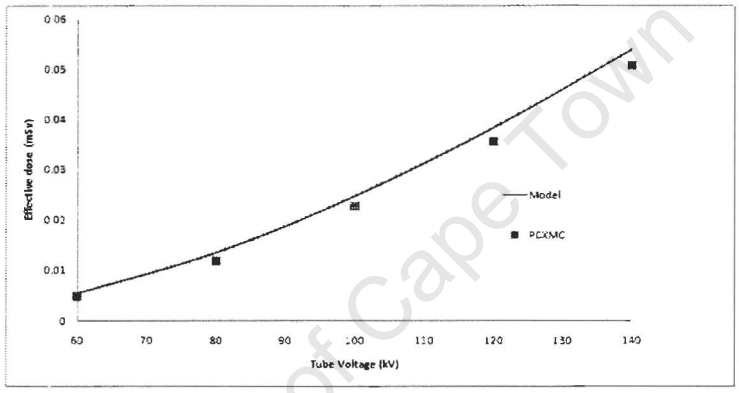

(a) Abdomen and pelvis region

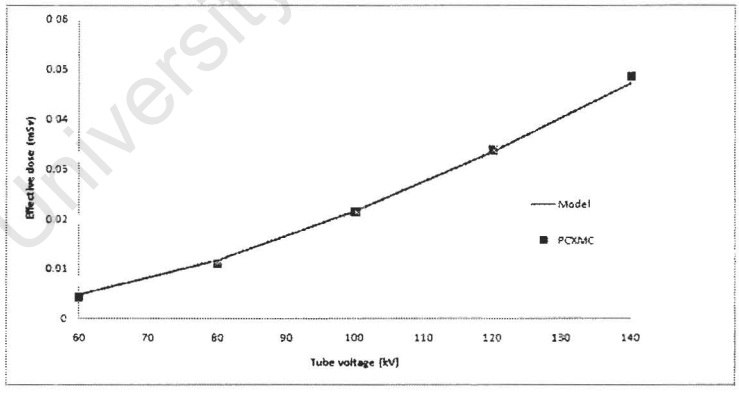

(b) Chest region

Tube current, scan speed and collimator width affect the flux of photons but not the beam energy as discussed in Section 2.1.3.3. Therefore these factors are linearly related to entrance dose and effective dose. This linear dependence was verified for the model for entrance dose and E.

A number of other comparisons and checks were also completed during the development of the code. These checks were put in place to find coding errors and to check that the theory was applied correctly at every step in the development of the new model. A number of examples are outlined here. Energy spectra generated using a variation of the Boone and Seibert (1997) where compared to published results from the Boone and Seibert (1997) study. The energy absorption curves (Section 6.2.1.2) generated using the Boone (1992) model were generated for monochromatic spectra and compared to the published results for various phantom thicknesses. The total absorbed dose from a polychromatic spectrum was also compared to data from the Boone (1992) study. The Huda and Gkanatsios (1997) model for patient thickness was compared to published data in the Gkanatsios and Huda (1997) study. The patient dimension model (Section 6.2.1.3) was compared to patient dimensions generated using PCXMC, which uses the same model. Comparisons were made at every stage of development by comparing the output of that stage to published results from the literature that the method was based on. In this manner any coding errors could be detected and corrected if the results of the new model disagreed with published results obtained using the same theory.

7.4 Additional results

This section uses the abdomen examination to demonstrate results that can be obtained using this model.

7.4.1 Standard examinations

This section simulates the standard AP abdomen examination available on Statscan for a medium sized patient with a mass of 71 kg and a height of 174 cm. The technique factors used in this section were the settings available on Lodox for the medium patient examination and are shown in Table 4.7. These are a tube voltage of 100 kV, a tube current of 200 mA, a slit width of 0.4 mm, a scan speed of 70 mm/s and a FSD of 98 cm.

This model predicted an entrance dose of 250 μGy and an E of 82 μSv compared to an entrance dose of 243 μGy measured using a dosemeter and an E of 80 μSv calculated from the measured entrance dose using PCXMC with full field parameters

(See Table 4.7). The reasons for the differences are those discussed in Section 7.2 as well as that the PCXMC values were calculated using the full field instead of the iterative approach as discussed in Section 3.2.2.

The beam energy and the dose are visualised in Figures 7.9, 7.10, 7.11 and 7.12. Figure 7.9 shows the energy spectrum that is generated for these technique factors and describes the total number of photons (in each energy bin of width 1 keV) moving through a cross sectional area of 1 mm^2 at the given FSD. Figures 7.10 and 7.11 give two views of a graph visualising the equivalent dose (H_T) to each organ per slice. H_T, as discussed in Section 2.1.4.4, is the average dose to each organ. This is calculated by dividing the energy absorbed in this organ during the examination by the mass of the organ (see Section 6.2.1.4). What these graphs describe is the energy imparted for each 1cm wide beam slice divided by the total mass of the organ. These organs are used in the calculation of effective dose ICRP (1991). A graph like this can be useful for determining which organs make the biggest contribution to effective dose in a particular examination. For example, a lead sheet could be placed in the groin region to remove the large testicular dose near the end of the scan. Figure 7.12 shows the effective dose per slice and is useful for visualising which part of the scan contributes the most to the total effective dose. The area under this graph represents the effective dose. Note the correlation between the high testicular dose near the end of the scan in Figure 7.10 and the high effective dose in Figure 7.12.

Figure 7.9: The energy spectrum for a tube voltage of 100kV, a tube current of 200mA, a slit width of 0.4mm, a scan speed of 70mm/s and an FSD of 98cm.

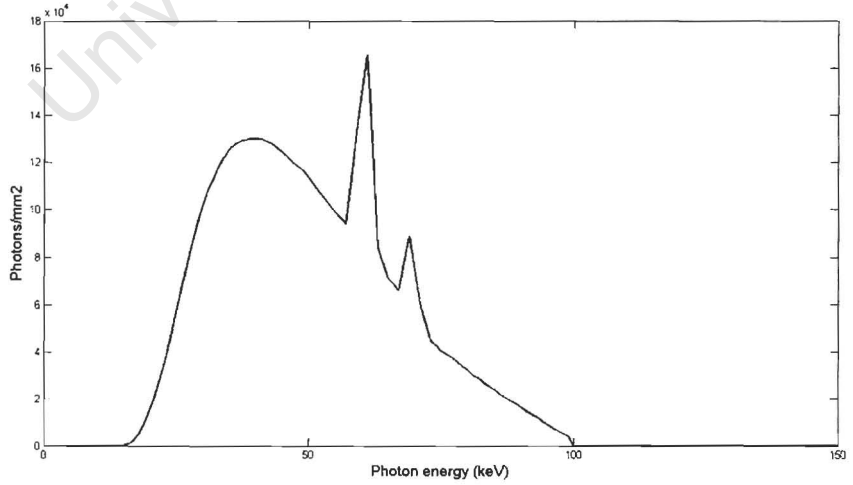

Figure 7.10: View 1 of the dose to each organ per slice simulated for a tube voltage of 100kV, a tube current of 200mA, a slit width of 0.4mm, a scan speed of 70mm/s and an FSD of 98cm.

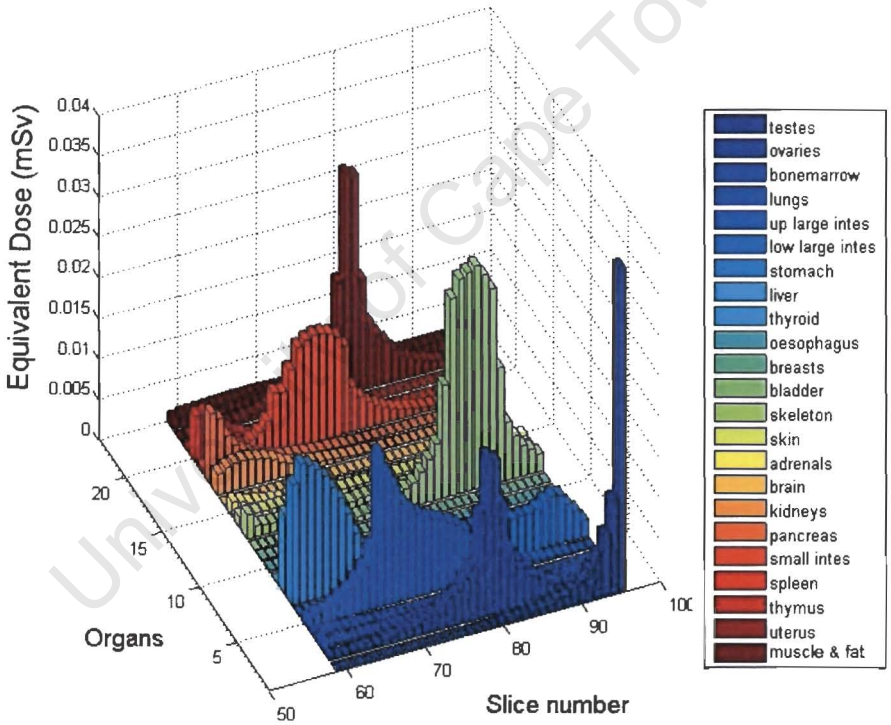

Figure 7.11: View 2 of the dose to each organ per slice simulated for a tube voltage of 100kV, a tube current of 200mA, a slit width of 0.4mm, a scan speed of 70mm/s and an FSD of 98cm.

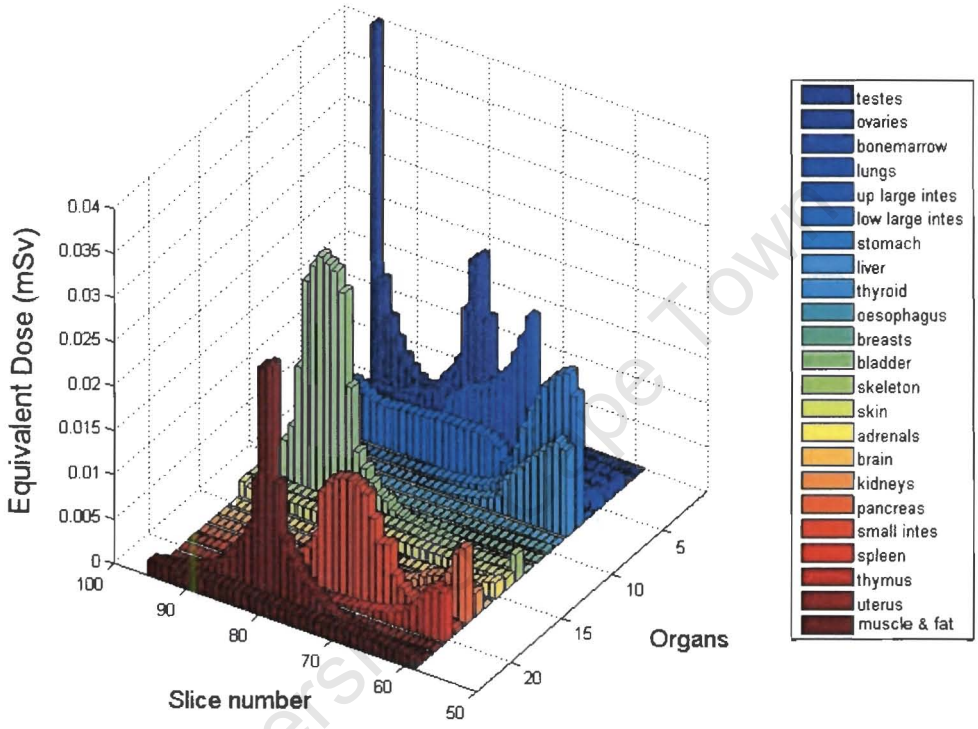

Figure 7.12: The effective dose for each slice of the examination for a tube voltage of 100kV, a tube current of 200mA, a slit width of 0.4mm, a scan speed of 70mm/s and an FSD of 98cm.

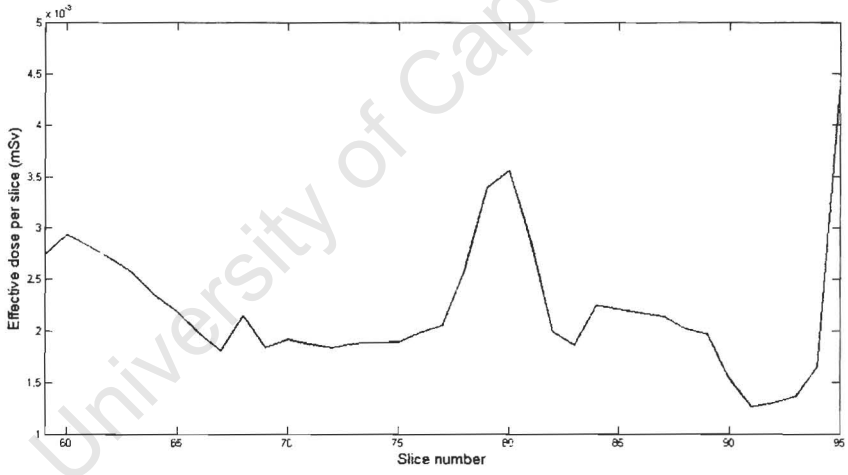

7.4.2 Automatic Technique Factor Correction (ATFC)

The model that has been developed in this study has also been designed to work with ATFC examinations. As described in the previous chapter, the model divides the scan into a large number of slices, which allows different technique factors to be used for different parts of the body simulating ATFC.

The example used in Section 7.4.1 is used as an illustration here as well. The technique factors are kept the same as the previous example except for the tube voltage which changes from 120 kV to 48 kV through the scan; the tube voltage changes by 1kV every 1cm in distance. This change in tube voltage is chosen arbitrarily to illustrate the model's ability to calculate varying technique factors. The total effective dose for the examination was 58 μSv.

Figure 7.13 shows a three dimensional plot of how the energy spectrum changes during the examination as the tube voltage is lowered. The two sharp peaks that increase with higher tube voltage are due to characteristic radiation (see Section 2.1.3). Figure 7.14 shows the entrance dose (free-in-air) and the dose-area product (DAP) during the examination. The entrance dose is specified at a point and is, therefore, reduced as the photon flux is lowered; DAP is an accumulative measurement. Figure 7.15 shows the equivalent dose to each organ at each step of the examination. Figure 7.16 shows the effective dose for each slice of the examination. It is interesting to compare Figures 7.16 and 7.12 because it is clear that having a kV gradient with the ATFC scan maintains the basic shape of the effective dose curve but raises the dose to the earlier slices and lowers the doses to the later slices.

Figure 7.13: The energy spectrum of the beam for each slice of the examination for a tube current of 200mA, a slit width of 0.4mm, a scan speed of 70mm/s, an FSD of 98cm and a tube voltage ranging from 120kV to 48kV.

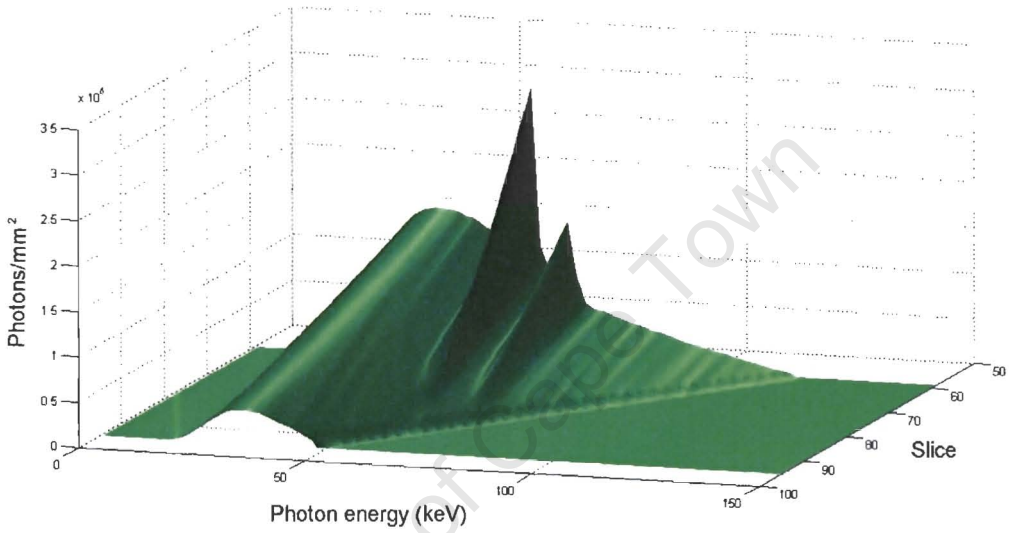

Figure 7.14: The entrance dose (free-in-air) and the dose-area product through the examination for a tube current of 200mA, a slit width of 0.4mm, a scan speed of 70mm/s, an FSD of 98cm and a tube voltage ranging from 120kV to 48kV.

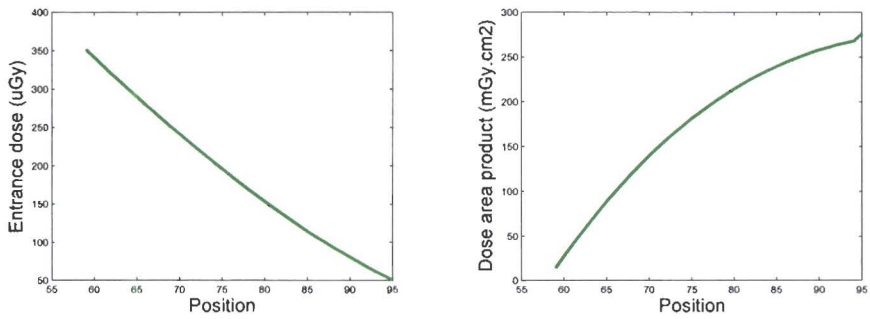

(a) Entrance dose

(b) Dose-area product

Figure 7.15: The dose to each organ per slice simulated for a tube current of 200mA, a slit width of 0.4mm, a scan speed of 70mm/s, an FSD of 98cm and a tube voltage ranging from 120kV to 48kV.

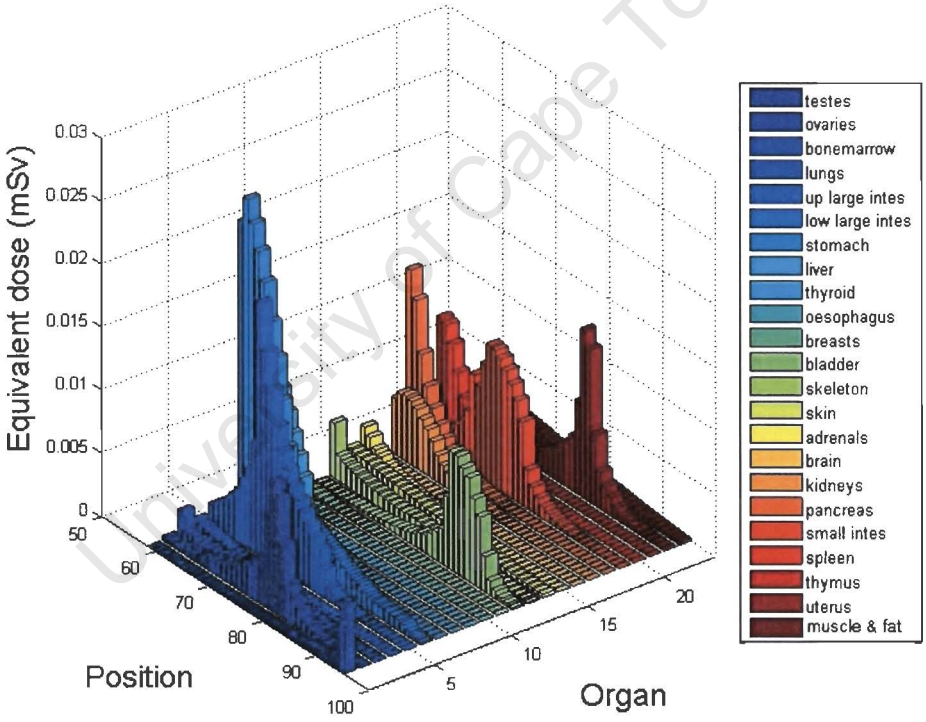

Figure 7.16: The effective dose for each step of the ATFC examination for a tube current of 200mA, a slit width of 0.4mm, a scan speed of 70mm/s, an FSD of 98cm and a tube voltage ranging from 120kV to 48kV.

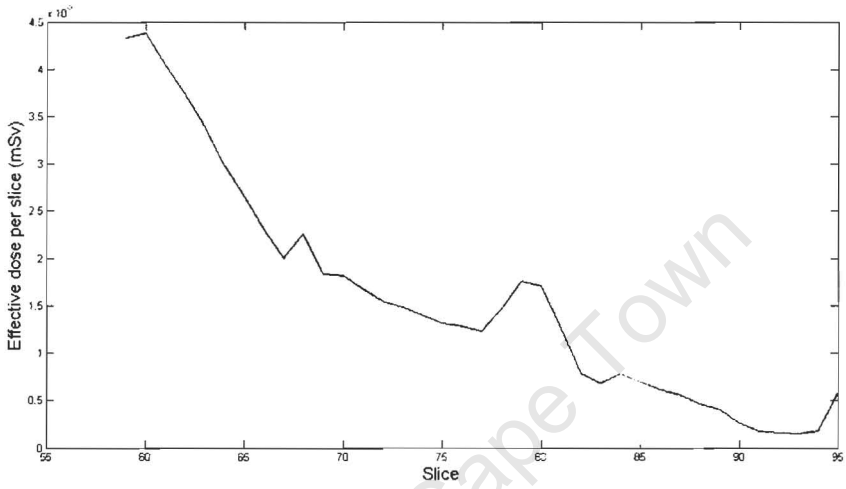

7.5 Advantages of the model and comparison with a similar model

A model has been developed by Theocharopoulos et al. (2006) to calculate effective dose for CT examinations. This model dramatically simplifies the calculation of E for CT but has certain disadvantages that are explored here. Some elements of the model described earlier in this chapter are similar to those of the Theocharopoulos et al. (2006) model so some interesting comparisons can be made.

Both models calculate E for a specific examination on a standard sized patient and from this E, calculate E to patients of various sizes. This is done by generating the ratio of the energy imparted in water phantoms of the equivalent thickness to that of the standard patient and the patient size of interest which are then used to adjust E. In the Theocharopoulos et al. (2006) model, E for the standard patient was measured directly for various regions of the body and various patient tube voltages, and then adjusted according to the patient size. The model developed in this study calculates the effective dose for the standard patient according to the input technique factors and organ absorption coefficients. The advantage of this method is that effective doses can be calculated for any tube voltage, not just those previously measured.

Another disadvantage of the Theocharopoulos et al. (2006) model is that the effective dose conversion coefficients are calculated for specific regions of the body and adjusted for different sized scans using the amount of energy imparted in that region. This, however, does not take into account sensitive organs that might be present or not present in the examination. For example, a conversion coefficient would be generated for pelvis X-ray examinations; if the size of the pelvis examination was halved then the energy imparted would halve which in turn would lead to the new calculation of E being half the effective dose of the previous calculation. In reality, the new scan might not include a highly radiation sensitive organ such as the testes anymore. This would lead to a far greater decrease than calculated in this method. The method developed in this study, however, calculates individual organ doses for 1 cm thick slices, allowing the effective dose to be calculated from the specific organs exposed to radiation by the examination.

The Theocharopoulos et al. (2006) model does, however, take into account the change in patient dimensions for paediatric patients because the patient head is generally larger relative to the rest of the body compared to adult patients. The current model developed in this study scales the patient dimensions according to the patient mass and height. If this model were to be applied to paediatric patients then a separate set of slice dependant organ absorption coefficients (see Section 6.2.1.4) should be generated for paediatric patients to give greater accuracy.

There are also a number of key advantages that this model has over current Monte Carlo simulators used in radiography (even though certain data used in this model was generated previously using a Monte Carlo simulator). Current commercial Monte Carlo simulators have been designed with full field radiography in mind, thus the beam geometry for LSSR is not taken into account. This leads to small errors (as discussed in Section 3.2.2) and means that ATFC examinations cannot be modelled directly although they can be modelled by writing a key logging script to run iterations across the body (see Section 3.2.2). This, however, can take up to 8 hours in comparison to the calculation performed using this model in under 10 seconds. In future, a Monte Carlo simulator could be developed specifically for LSSR; simulations with LSSR, however, would still be slower than this model. Current Monte Carlo simulators have not been designed to work with LSSR and, therefore, can not calculate the entrance dose from technique factors such as speed and slit width. The entrance dose must, therefore, be measured before E can be generated. This model, however, calculates entrance dose directly from the technique factors. A similar method could be included in later Monte Carlo simulators.

7.6 Summary and discussion

The framework of a model to estimate dose for LSSR is discussed in Chapter 6. Chapter 7 compared results generated by the new model to existing models and measured results. These comparisons showed the model to be accurate but there is still scope to further optimise the model. Additional estimates of the model were discussed including equivalent dose for each organ and effective dose as a function of position.

The model has been tested for the full range of tube voltages, tube currents and scan speeds and so can be used to model typical examinations on LSSR as well as any change in technique factors. What still needs to be ascertained, however, is whether the 1 cm wide slices are small enough to model sharp changes in technique factors that can be used with the ATFC examination, which is currently an available option for the full-spine examination. There might also be a lag time in the radiography unit between changing the technique factors and changing the beam energy, that might need to be included in the model if the ATFC examination is to be estimated. Direct measurements would answer these queries. However, there are difficulties associated with directly measuring effective dose for a continuously changing beam used in ATFC. Thermoluminescent dosimeters (TLDs) in a phantom cannot be used because the TLD dose to each organ is averaged to get the organ dose whereas with varying technique factors, TLDs would have to be placed at every point inside each organ in order to get an accurate dose to the organ. A measurement of the tube output such as entrance dose (free-in-air) at each point or dose-area product would provide a comparison with the tube output and would be a first step to validating the model's use with ATFC.

8 Conclusion

Dose measurements have been presented for a linear slit scanning radiography (LSSR) unit. Entrance dose measurements for standard AP and lateral examinations were made and used with the commercially available Monte Carlo simulator PCXMC to calculate effective dose (E). The procedures used to make these measurements and calculations were verified using comparisons with other measurement techniques. These results showed that for most examinations, LSSR offered a considerably lower dose than conventional radiography. The reasons for this lower dose include scatter reduction and the beam geometry of LSSR.

A model has been developed for more effective prediction of entrance and effective dose in LSSR, using a moving slice approach. This approach offered much greater computational speed than Monte Carlo simulations because any data required from Monte Carlo simulators were generated in advance and stored in a database. This model also offers better functionality and accuracy with LSSR as the model has been specifically designed with LSSR in mind. The results generated include the equivalent dose to each organ and effective dose, as the scan progresses, as well as the effective dose for the entire examination. The model has also been designed to be used with the automatic technique factor correction (ATFC) scan, available for the full-spine examination, where the technique factors change during the examination. The new model was verified by making comparisons between its results and measured results as well as comparisons with existing models. However, further verification is required before it is used with the ATFC examination. This would provide a challenging future project due to the difficulties associated with directly measuring effective dose for a

scan with a continuously changing beam energy.

Currently any lateral or AP examination can be simulated provided the width of the scanning beam is greater than or equal to the width of the patient. The flexibility of the model could be improved by using the X-ray image to determine which organs are within the exposed area. This along with the current model and an algorithm to estimate the beam scatter within the patient could be used to calculate effective dose for any exposed region.

A future project could involve combining this effective dose prediction model with an image quality prediction model. This tool could then be used to further optimise the scan parameters for each examination in terms of dose and image quality.

Bibliography

A Alhamud. System optimisation of a full body slit scan using the cascaded model methodology. Technical report, University of Cape Town, 2006.

A Aroua, R Bize, I Buchillier-Decka, JP Vader, JF Valley, and P Schnyder. X-ray imaging of the chest in Switzerland in 1998: a nationwide survey. *European Radiology*, 13:1250–1259, 2002a.

A. Aroua, I. Decka, B. Burnand, J.P. Vader, and J.F. Valley. Dosimetric aspects of a national survey of diagnostic and interventional radiology in Switzerland. *Medical Physics*, 29:2247, 2002b.

G Barnes, R Sones, and M Tesic. Digital chest radiography: performance evaluation of a prototype unit. *Radiology*, 154:801–806, 1985.

G Barnes, X Wu, and P Sanders. Scanning slit chest radiography: a practical and efficient scatter control design. *Medical Physics*, 190:525–528, 1994.

Z Begum. Entrance surface, organ and effective doses for some of the patients undergoing different types of x ray procedures in Bangladesh. *Radiation Protection Dosimetry*, 95:257–262, 2001.

S Beningfield, H Potgieter, A Nicol, S van As, G Bowie, E Hering, and E Latti. Report on a new type of trauma full-body digital X-ray machine. *Emergency Radiology*, 10:23–29, 2003.

J Beutel, J Kundel, and R van Metter. *Handbook of Medical Imaging*, volume 1. Society of Photo-Optical Instrumentation Engineers, Bellingham, Washington, 2000.

J Bland and D Altman. Statistical methods for assessing agreement between two methods of clinical measurement. *Lancet*, (i):307–310, 1986.

K Boffard, J Goosen, F Plani, E Degiannis, and H Potgieter. The use of low dosage X-ray (Lodox/Statscan) in major trauma: comparison between low dose X-ray and conventional X-ray techniques. *Journal of Trauma*, 60:1175–1183, 2006.

J Boone and J Seibert. An accurate method for computer-generating tungsten anode X-ray spectra from 30 to 140 kV. *Medical Physics*, 24:1661–1670, 1997.

JM Boone. Parametrized X-ray absorption in diagnostic radiology from Monte Carlo calculations: implications for X-ray detector design. *Medical Physics*, 19:1467–1473, 1992.

H Chan and K Doi. Investigation of the performance of antiscatter grids: Monte Carlo simulation studies. *Physics in Medicine and Biology*, 27:785–803, 1982.

G Compagnone, L Pagan, and C Bergamini. Effective dose calculations in conventional diagnostic X-ray examinations for adult and paediatric patients in a large Italian hospital. *Radiation Protection Dosimetry*, 114:164–167, 2005.

G Compagnone, M Baleni, L Pagan, F Calzolaio, L Barozzi, and C Bergamini. Comparison of radiation dose to patients undergoing standard radiographic examinations with conventional screen-film radiography, computed radiography and direct digital radiography. *British Journal of Radiology*, 79:899–904, 2006.

L Court and T Yamazaki. Technical note: a comparison of antiscatter grids for digital radiography. *British Journal of Radiology*, 77:950–952, 2004.

P Dendy and B Heaton. *Physics for Radiologists*. Blackwell Science Ltd, 1987.

T Douglas, V Sanders, R Pitcher, and A van As. Early detection of fractures with low-dose digital X-ray images in a pediatric trauma unit. *Journal of Trauma*, (in Press), 2008. doi: 10.1097/01.ta.0000198534.47134.bc.

J Geleijns, J Broerse, M. van Vliet, M Lopez, and H Zonderland. Assessment of effective dose in paediatric radiology: a survey at 14 Dutch hospitals. *Radiation Protection Dosimetry*, 90:135–140, 2000.

N Gkanatsios and W Huda. Computation of energy imparted in diagnostic radiology. *Medical Physics*, 24:571–579, 1997.

K Gogas, E Yakoumakis, I Tsalafoutas, and T Makri. Radiation dose considerations in common paediatric X-ray examinations. *Pediatric Radiology*, 33:236–240, 2003.

J Hansen, A Jurik, B Fiirgaard, and N Egund. Optimisation of scoliosis examinations in children. *Pediatric Radiology*, 33:752–765, 2003.

M Harpen. A mathematical spread sheet application for production of entrance skin exposure nomagrams. *Medical Physics*, 23:241–242, 1996.

D Hart and B Wall. *Radiation Exposure of the UK population from Medical and Dental X-ray Examinations. NRPB-W4.* National Radiologial Protection Board, Chilton, United Kingdom, 2002.

D Hart, D Jones, and B Wall. *Estimation of effective dose in diagnostic radiology from entrance surface dose and dose-area product measurements. NRPB-R262.* NRPB publications, NRPB-R262, Chilton, United Kingdom, 1994.

D Hart, D Jones, and B Wall. *Coefficients for estimating effective doses from paediatric X-ray examinations.* NRPB publications, NRPB-R279, Chilton, United Kingdom, 1996.

E Hering. *Radiation physics and protection.* University of Cape Town, 1995.

W Huda and N Gkanatsios. Effective dose and energy imparted in diagnostic radiology. *Medical Physics*, 24:1311–1316, 1997.

W Huda, J Atherton, D Ware, and W Cumming. An approach for the estimation of effective radiation dose at CT in pediatric patients. *Radiology*, 203:417–422, 1997.

ICRP. *1990 Recommendations of the ICRP. Annals of the ICRP*, volume 21. Pergamon Press, Oxford, UK, 1991.

ICRP. *ICRP Publication 103. Recommendations of the ICRP. Annals of the ICRP*, volume 37. Elsevier, 2008.

B Irving, G Maree, E Hering, and T Douglas. Radiation dose from a linear slit scanning X-ray machine with full-body imaging capabilities. *Radiation Protection Dosimetry*, (in press), 2008.

W Kalender. Calculation of X-ray grid characteristics by Monte Carlo methods. *Physics in Medicine and Biology*, 27:353–361, 1982.

B Kevles. *Naked to the Bone: Medical Imaging in the Twentieth Century.* Rutgers University Press, 1997.

F Khan. *The Physics of Radiation Therapy.* Williams and Wilkens, 2nd edition, 1994.

Lodox. Statscan critical imaging system: Product specifications and physical dimensions. Technical report, Lodox Systems, 2006.

G Maree, B Irving, and E Hering. Paediatric dose measurement in a full-body digital radiography unit. *Pediatric Radiology*, 37:990–997, 2007.

CJ Martin. Effective dose: how should it be applied to medical exposures? *British Journal of Radiology*, 80:639–647, 2007.

F Mélin, G Zibordi, and S Djavidnia. Development and validation of a technique for merging satellite derived aerosol optical depth from SeaWiFS and MODIS. *Remote Sensing of Environment*, 108:436–450, 2007.

L Miller, S Mirvis, L Harris, and J Haan. Total-body digital radiography for trauma screening: initial experience. *Applied Radiology*, 33:8–14, 2004.

K Mohamadain, L da Rosa, A Azevedo, M Guebel, M Boechat, and F Habani. Dose evaluation for paediatric chest x-ray examinations in Brazil and Sudan: low doses and reliable examinations can be achieved in developing countries. *Physics in Medicine and Biology*, 49:1017–1031, 2004.

NIST. XCOM: Photon cross sections database, July 2008. http://physics.nist.gov/PhysRefData/Xcom/Text/XCOM.html.

R Nussbaum. The linear no-threshold dose-effect relation: is it relevant to radiation protection regulation? *Medical Physics*, 25:291–299, 1998.

D Okkalides and M Fotakis. Patient effective dose resulting from radiographic examinations. *British Journal of Radiology*, 67:564–572, 1994.

D Papadimitriou, A Perris, M Molfetas, N Panagiotakis, A Manetou, G Tsourouflis, J Vassileva, P Chronopoulos, O Karapanagiotou, and S Kottou. Patient dose, image quality and radiographic techniques for common x ray examinations in two Greek hospitals and comparison with European guidelines. *Radiation Protection Dosimetry*, 95:43–48, 2001.

R Pitcher, A van As, V Sanders, N Wieselthaler, A Vlok, S Paverd, T Kilborn, H Rode, H Potgieter, and S Beningfield. A pilot study evaluating the "STATSCAN" digital X-ray machine in paediatric polytrauma. *Emergency Radiology*, 15:35–42, 2008.

G. Pollack and D. Stump. *Electromagnetism*. Addison-Wesley, 2001.

J Potgieter, M de Villiers, M Scheelke, and G de Jager. An explanation for the extremely low, but variable radiation dosages measured in a linear slit scanning radiography system. *Medical Imaging 2005: Physics of Medical Imaging (SPIE)*, 5745:1138–1145, 2005.

Ionisation Chamber Type 23361 User Manual. PTW Freiburg, Germany.

E Ron. Ionizing radiation and cancer risk: evidence from epidemiology. *Pediatric Radiology*, 32:232–237, 2002.

E Samei and M Flynn. An experimental comparison of detector performance for direct and indirect digital radiography systems. *Medical Physics*, 30:608–622, 2002.

E Samei, R Saunders, J Lo, J Dobbins, J Jesneck, C Floyd, and C Ravin. Fundamental imaging characteristics of a slot-scan digital chest radiographic system. *Medical Physics*, 31:2687–2698, 2004.

E Samei, J Lo, T Yoshizumi, J Jesneck, J Dobbins, C Floyd, H McAdams, and C Ravin. Comparative scatter and dose performance of slot-scan and full-field digital chest radiography systems. *Medical Physics*, 235:940–949, 2005.

M Scheelke. System characterisation of a full body slit scanning radiography machine: theory and experiment. Master's thesis, University of Cape Town, 2005.

M. Scheelke, J. Potgieter, and M. de Villiers. System characterization of the STATSCAN full body slit scanning radiography machine: theory and experiment. *Medical Imaging 2005: Physics of Medical Imaging (SPIE)*, 5745:1179–1190, 2005.

F Schultz, J Geleijns, F Spoelstra, and J Zoetelief. Monte Carlo calculations for assessment of radiation dose to patients with congenital heart defects and to staff during cardiac catheterizations. *British Journal of Radiology*, 76:638–647, 2003.

A Servomaa and M Tapiovaara. Organ dose calculation in medical x ray examinations by the program pcxmc. *Radiation Protection Dosimetry*, 80:213–219, 1998.

P Shikhaliev, T Xu, and S Molloi. Photon counting computed tomography: concept and initial results. *Medical Physics*, 32:427–436, 2005.

T Slovis. CT and computed radiography: the pictures are great, but is the radiation dose greater than required? *AJR*, 179:39–41, 2002.

N Theocharopoulos, K Perisinakis, J Damilakis, H Varveris, and N Gourtsoyiannis. Comparison of four methods for assessing patient effective dose from radiological examinations. *Medical Physics*, 29:2070–2079, 2002.

N Theocharopoulos, J Damilakis, A Karantanas, and N Gourtsoyiannis. Estimation of effective doses to adult and pediatric patients from multislice computed tomography: a method based on energy imparted. *Medical Physics*, 33:3846–3856, 2006.

United Nations Scientific Committee on the Effects of Atomic Radiation. *UNSCEAR 2000 Report, Sources and Effects of ionising radiation*. UNSCEAR, 2000.

A van As, T Douglas, T Kilborn, R Pitcher, and H Rode. Multiple injuries diagnosed using full-body digital X-ray. *Pediatric Surgery*, 41:E25–E28, 2006.

S Watson, A Jones, W Oatway, and J Hughes. Ionising radiation exposure of the UK population: 2005 review. HPA-RPD-001. *Health Protection Association*, 2005.

E Yakoumakis, I Tsalafoutas, D Nikolaou, I Nazos, E Koulentianos, and C Proukakis. Differences in effective dose estimation from dose area product and entrance surface dose measurements in intravenous urography. *British Journal of Radiology*, 74:727–734, 2001.

A

Additional entrance dose measurements

Additional entrance dose measurements to those published (Irving et al., 2008; Maree et al., 2007) are shown in this section. These measurements were taken at Groote Schuur Hospital in 2006 and include entrance doses for all patient sizes specified on the Statscan unit. It is important to note that the FSD for each dose is different to that discussed earlier. These results can be modified for any FSD using the 1/r rule.

Table A.1: Entrance dose measurements recorded in 2006 for all patient sizes.

	Technique Factors					Measurements			Corrected measurements	
Examination	**Tube voltage**	**Tube current**	**Speed**	**Gap Size**	**Focal Point**	**ground to dose meter**	**FSD**	**Entrance dosage**	**SSD**	**Entrance Dose**
Paediatric	**(kV)**	**(mA)**	**(%)**	**(mm)**		**(m)**	**(m)**	**(uGy)**	**(m)**	**(mGy)**
Skull	90	125	50	0.4	small	1.05	0.987	124	1.021	0.119
Chest (Lung)	60	64	50	0.4	small	1.05	0.987	30	1.052	0.028
Adomen	80	80	50	0.4	small	1.05	0.987	70	1.052	0.065
Pelvis	80	64	50	0.4	small	1.05	0.987	53	1.052	0.049
Femur	70	100	50	0.4	small	1.05	0.987	63	1.110	0.057
Knee	60	80	50	0.4	small	1.05	0.987	38	1.132	0.033
Tibia	50	80	50	0.4	small	1.05	0.987	25	1.151	0.021
Ankle	50	80	50	0.4	small	1.05	0.987	25	1.166	0.021
Foot	50	80	50	0.4	small	1.05	0.987	25	1.166	0.021
Full Body	80	160	100	0.4	large	1.05	0.987	68	1.052	0.064
Small										
Skull	100	160	50	0.4	small	1.05	0.987	189	1.033	0.180
Chest (Lung)	80	64	50	0.4	small	1.05	0.987	52	1.033	0.050
Adomen	90	160	50	0.4	small	1.05	0.987	169	1.033	0.161
Pelvis	90	160	50	0.4	small	1.05	0.987	158	1.033	0.151
Femur	80	100	50	0.4	small	1.05	0.987	81	1.061	0.076
Knee	70	100	50	0.4	small	1.05	0.987	64	1.108	0.057
Tibia	60	100	50	0.4	small	1.05	0.987	46	1.138	0.040
Ankle	60	100	50	0.4	small	1.05	0.987	47	1.163	0.040
Foot	60	100	50	0.4	small	1.05	0.987	47	1.163	0.039
Full Body	100	125	100	0.4	large	1.05	0.987	79	1.033	0.076
Medium										
Skull	110	160	50	0.4	small	1.05	0.987	221	1.007	0.217
Chest (Lung)	100	80	50	0.4	small	1.05	0.987	97	1.004	0.095
Adomen	100	200	50	0.4	small	1.05	0.987	250	1.004	0.245
Pelvis	100	200	50	0.4	small	1.05	0.987	235	1.004	0.231
Femur	90	160	50	0.4	small	1.05	0.987	160	1.052	0.151
Knee	80	160	50	0.4	small	1.05	0.987	129	1.088	0.118
Tibia	70	160	50	0.4	small	1.05	0.987	101	1.129	0.089
Ankle	70	160	50	0.4	small	1.05	0.987	101	1.146	0.087
Foot	60	160	50	0.4	small	1.05	0.987	74	1.146	0.064
Full Body	110	160	100	0.4	large	1.05	0.987	118	1.004	0.118
Large										
Skull	110	200	50	0.4	small	1.05	0.987	276	0.978	0.279
Chest (Lung)	120	160	50	0.4	small	1.05	0.987	161	0.978	0.163
Adomen	110	200	50	0.4	large	1.05	0.987	293	0.978	0.297
Pelvis	110	200	50	1	large	1.05	0.987	695	0.978	0.703
Femur	100	200	50	0.4	large	1.05	0.987	242	1.025	0.236
Knee	90	200	50	0.4	small	1.05	0.987	199	1.078	0.184
Tibia	80	200	50	0.4	small	1.05	0.987	160	1.105	0.144
Ankle	80	200	50	0.4	small	1.05	0.987	161	1.141	0.140
Foot	70	200	50	0.4	small	1.05	0.987	126	1.141	0.110
Full Body	120	160	100	0.4	large	1.05	0.987	136	0.978	0.140
Extra Large										
Skull	120	200	50	0.4	small	1.05	0.987	319	0.953	0.331
Chest (Lung)	140	160	50	0.4	small	1.05	0.987	340	0.954	0.353
Adomen	120	200	50	1	large	1.05	0.987	809	0.954	0.839
Pelvis	120	200	50	1	large	1.05	0.987	811	0.954	0.841
Femur	110	160	50	1	large	1.05	0.987	562	0.999	0.563
Knee	100	200	50	1	large	1.05	0.987	595	1.061	0.560
Tibia	90	200	25	0.4	small	1.05	0.987	413	1.102	0.374
Ankle	90	200	25	0.4	small	1.05	0.987	413	1.141	0.361
Foot	80	200	50	0.4	small	1.05	0.987	167	1.141	0.145
Full Body	145	200	100	0.4	large	1.05	0.987	229	0.954	0.241

B

Ionisation Chamber Documents

B.1 Partial volume exposure of Radcal ionisation chambers

Radcal Corporation
426 West Duarte Road (626) 357-7921
Monrovia, CA 91016 FAX (626) 357-8863
www.Radcal.com E-mail: service@radcal.com

RWTÜV USA INC.
Certified ISO 9001-2000

Advisory Note

Date: 2 April 2007
Topic: Partial Volume Exposure of Radcal ion chambers.

Radcal ion chambers have been designed for radiation exposures that completely and uniformly exposure the entire volume of the ion chamber. The only exceptions are the Radcal -CT ion chambers which were specifically designed for partial volume exposures. Partial volume exposure of other Radcal chambers will result in errors arising from variations in sensitivity and energy response over the chamber's exposed volume.

In recent years, slot-scanning radiation devices have become common and the need to measure their radiation output has become important. Radcal ion chambers can be used for this purpose without any increased uncertainties provided the following conditions are met:

1. Measurements are only made in an integrate mode (dose) and the integration period must equal or exceed the time that the beam exposes the chamber. Rate mode measurement is not suitable.

2. The scanning beam length must exceed the chamber's width. The beam must be uniform over the length of the beam that exposes the chamber.

3. The scanned area must exceed the active volume of the chamber.

4. The x-ray technique (kV, mA, sweep-speed, distance and collimation) must remain constant during the interval that the beam sweeps over the active volume of the ion chamber.

5. During the exposure, the exposure rate (mGy/s) measured at the surface of the ion chamber must not exceed the chamber's published specification.

For further information contact Radcal technical support at: (626) 357-7921.

B.2 PTW Ionisation chamber communication

Dear Mr. Maree

We can agree to this document. The basic point is that the chamber must be irradiated homogeneously and completely during the measuring process. It is of no importance for DOSE MEASUREMENT whether this happens in one moment or successively by a scanning beam.

Best regards

Christian Pychlau

—— Original-Nachricht ——
Betreff: DOSE MEASUREMENT
Datum: Mon, 02 Apr 2007 15:42:11 +0200
Von: Gert Maree Gert.Maree@uct.ac.za
An: Tobias Kremp tobias.kremp@ptw.de
CC: Herman Potgieter herman.potgieter@lodox.com ,
Egbert Hering Egbert.Hering@uct.ac.za

Dear Mr Kremp

I contacted you in August 2005 regarding the 30 cubic centimetre cylindrical chamber Ser. No. W23361-0431) and your help was very much appreciated. We would like to ask some more advice again, however.

We are using the PTW Unidos with the above-mentioned chamber to measure entrance doses (free-in-air) for patients. The X-ray unit involved is called LODOX Statscan and it is a linear slot scanner. A conventional X-ray tube is mounted on a C-arm and on the other side of the C-arm is the detector, which is made up of scintillator arrays linked to charged coupled devices (CCD's). The C-arm is able to rotate around the patient up to 100scan angles. The beam is collimated to 1 mm or less, producing a fan beam that during a scan travels across the patient with a chosen speed of 35 mm/s, 70 mm/s or 140 mm/s.

One of these units was installed recently in Switzerland. Their Regulatory body, BAG, is questioning the accuracy of our dose measurements, however. They say that the ionisation chamber that we use is not calibrated to be partially ionised. We are convinced, however, that accurate results are obtained. A very short explanation in

this regard is attached. It would be very much appreciated if you could comment on the attached document.

Yours sincerely

Gerrie Maree
Medical Physicist
University of Cape Town and Groote Schuur Hospital
CAPE TOWN
South Africa

C Dose comparison data

C.1 Entrance dose comparison data

Table C.1 contains the technique factors and scan parameters of each scan used in a comparison between the three dose prediction methods and contains the dose predicted by each method.

Table C.1: Comparison between measured and predicted entrance dose for various examinations.

Procedure Name	Tube Voltage (kV)	Slit width (mm)	Focal spot	Tube Current (mA)	Scan speed mm/s	SSD (cm)	Entrance dose (free-in-air) (µGy)				Percentage difference between actual measurement and estimation (%)		
							Measured	Method 1	Method 2	Method 3	Method 1 %	Method 2 %	Method 3 %
Paediatric Patients													
Full Body AP (2005)	80	0.4	S	100	140	98.00	41	40	41	54	-1	1	33
Full Body AP (2006)	80	0.4	L	160	140	98.00	69	65	66	87	-6	-5	26
Chest (lung) AP supine	100	0.4	S	64	140	99.30	41	40	41	43	-2	0	7
Chest (lung) AP supine	60	0.4	S	64	70	99.30	30	28	28	51	-7	-6	73
Chest (lung) LAT	110	0.4	S	100	140	72.40	101	101	104	102	1	3	1
Chest (lung) LAT	100	0.4	S	64	70	72.40	108	109	111	118	0	3	9
Abdomen AP	80	0.4	S	125	140	98.00	51	51	51	68	0	2	35
Abdomen AP	80	0.4	S	80	70	98.00	70	65	66	87	-7	-5	25
Abdomen Lumbar Lat	100	0.4	S	200	140	72.40	169	170	174	185	0	3	9
Abdomen Lumbar Lat	90	0.4	S	200	70	72.40	275	277	283	332	1	3	21
Pelvis AP	80	0.4	S	125	140	98.00	51	51	51	68	-1	1	33
Pelvis AP	80	0.4	S	64	70	98.00	53	52	53	70	-2	0	32
Pelvis / Hip LAT	100	0.4	S	160	140	72.40	139	136	139	148	-2	0	6
Pelvis / Hip LAT	90	0.4	S	64	70	72.40	91	89	90	106	-2	0	17
Skull AP	90	0.4	S	200	140	93.50	110	107	109	129	-2	0	17
Skull AP	90	0.4	S	125	70	93.50	130	134	137	161	3	5	23
Skull LAT	80	0.4	S	200	140	80.40	103	99	100	133	-4	-2	29
Skull LAT	80	0.4	S	125	70	80.40	126	123	125	166	-2	0	32
C Spine LAT	70	0.4	S	200	140	72.40	92	83	84	129	-10	-8	40
C Spine LAT	70	0.4	S	125	70	72.40	109	104	105	161	-5	-3	48
Full Spine LAT	100	0.4	S	125	70	72.40	221	212	217	231	-4	-2	5
Full Spine LAT	100	0.4	S	125	70	72.40	208	212	217	231	2	4	11
Medium patients													
Full body	110	0.4	S	160	140	98.00	115	120	123	120	4	6	4
Chest ap	100	0.4	S	80	70	99.30	99	99	101	108	0	3	9
chest lat	120	0.4	S	125	70	72.40	284	298	305	278	5	7	-2
ab ap	100	0.4	S	200	70	98.00	243	251	257	273	3	6	12
ab lat	110	1.0	L	200	35	72.40	1910	2029	2081	2038	6	9	7
pelvis ap	100	0.4	S	200	70	98.00	246	251	257	273	2	4	11
pelvis lat	110	0.4	S	200	70	72.40	394	406	416	408	3	6	3
skull ap	110	0.4	S	160	70	93.50	245	251	258	252	3	5	3
skull lat	100	0.4	S	160	70	80.40	242	245	250	267	1	4	10
c spine lat	90	0.4	S	160	70	72.40	225	222	226	266	-1	1	18
full spine lat	135	1.0	L	200	70	72.40	1312	1470	1505	1255	12	15	-4
Extra large patients													
Full body	145	0.4	L	200	140	95.00	240	252	259	206	5	8	-14
Chest ap	140	0.4	S	160	70	95.00	361	382	391	317	6	8	-12
chest lat	140	1.0	L	125	70	68.00	938	1041	1066	866	11	14	-8
ab ap	120	1.0	L	200	70	95.00	831	907	930	848	9	12	2
ab lat	130	1.0	L	200	35	68.00	2641	2929	2999	2571	11	14	-3
pelvis ap	120	1.0	L	200	70	95.00	823	907	930	848	10	13	3
pelvis lat	130	1.0	L	200	70	68.00	1302	1465	1500	1286	12	15	-1
skull ap	120	0.4	L	200	70	93.50	350	369	378	345	5	8	-1
skull lat	110	0.4	L	200	70	80.40	351	365	375	367	4	7	5
c spine lat	110	1.0	L	200	70	68.00	987	1080	1108	1085	9	12	10
full spine lat	145	1.0	L	200	70	68.00	1548	1763	1810	1436	14	17	-7

C.2 Effective dose comparative data

Table C.2 contains the effective dose data generated using the commercially available Monte Carlo simulator PCXMC and the model developed in this study. This data was generated for a patient of height 174 cm and mass 71 kg. This data was generated for 1 cm increments over the whole body where 1 represents the top of the head and 174 represents the base of the foot. These simulations were generated for AP and lateral examinations. The parameters used for the AP examination was a tube voltage of 100kV, a total filtration of 2mmAl and a SSD of 95cm. An entrance dose of 1mGy was input into PCXMC. For the new model developed in this study a tube current of 300mA, a scan speed of 70mm/s and a slit with of 0.4mm was also input. This generated an entrance dose of 388.1uGy. Thus, the model data was scaled by the $\frac{1000}{388}$ so that both examinations used the same entrance dose. The entrance dose was scaled because PCXMC cannot generate entrance dose from the technique factors for LSSR and it must be provided. Similarly for the lateral examinations, the parameters used were a tube voltage of 100kV, a total filtration of 2mmAl and a SSD of 90cm. An entrance dose of 1mGy was input into PCXMC and for the new model, developed in this study, a tube voltage of 300mA, a scan speed of 70mm/s and a slit with of 0.4mm was also input. The entrance dose generated was 409.7 uGy which was used to scale the effective dose.

Table C.2: Effective dose (mSv) for each 1cm increment generated for PCXMC and the model developed in this study.

Iteration	AP Projection		Lateral Projection	
	PCXMC effective dose (mSv)	Model effective dose (mSv)	PCXMC effective dose (mSv)	Model effective dose (mSv)
1	9.70E-05	1.06E-04	1.15E-04	1.25E-04
2	4.47E-04	4.39E-04	5.48E-04	5.44E-04
3	7.28E-04	7.13E-04	9.13E-04	9.19E-04
4	9.51E-04	9.48E-04	1.22E-03	1.23E-03
5	1.10E-03	1.14E-03	1.46E-03	1.49E-03
6	1.24E-03	1.25E-03	1.60E-03	1.64E-03
7	1.31E-03	1.33E-03	1.69E-03	1.73E-03
8	1.33E-03	1.36E-03	1.76E-03	1.77E-03
9	1.27E-03	1.30E-03	1.67E-03	1.70E-03
10	1.16E-03	1.17E-03	1.49E-03	1.54E-03
11	1.00E-03	9.85E-04	1.31E-03	1.29E-03
12	6.00E-04	6.13E-04	1.09E-03	1.07E-03
13	6.50E-04	6.27E-04	7.15E-04	6.85E-04
14	7.31E-04	6.60E-04	7.38E-04	7.26E-04
15	7.87E-04	7.59E-04	8.45E-04	7.96E-04
16	9.68E-04	8.87E-04	9.33E-04	9.26E-04
17	1.10E-03	1.12E-03	1.07E-03	1.06E-03

continued on next page

continued from previous page

	PCXMC effective dose (mSv)	Prog effective dose (mSv)	PCXMC effective dose (mSv)	Prog effective dose (mSv)
18	1.38E-03	1.41E-03	1.27E-03	1.23E-03
19	1.82E-03	1.92E-03	1.66E-03	1.62E-03
20	3.48E-03	3.55E-03	2.92E-03	2.78E-03
21	1.12E-02	1.10E-02	5.70E-03	5.44E-03
22	1.45E-02	1.47E-02	6.90E-03	6.57E-03
23	1.62E-02	1.61E-02	7.49E-03	7.07E-03
24	1.14E-02	1.12E-02	5.80E-03	5.60E-03
25	3.89E-03	3.82E-03	9.12E-04	8.73E-04
26	3.28E-03	3.10E-03	7.87E-04	7.99E-04
27	2.99E-03	2.90E-03	9.05E-04	9.05E-04
28	3.21E-03	3.05E-03	1.07E-03	1.04E-03
29	3.18E-03	2.92E-03	1.03E-03	1.02E-03
30	3.36E-03	3.25E-03	1.21E-03	1.17E-03
31	3.59E-03	3.58E-03	1.35E-03	1.25E-03
32	4.09E-03	4.11E-03	1.38E-03	1.28E-03
33	4.62E-03	4.65E-03	1.56E-03	1.46E-03
34	5.78E-03	5.75E-03	1.67E-03	1.58E-03
35	7.68E-03	7.53E-03	1.98E-03	1.87E-03
36	8.43E-03	8.15E-03	1.89E-03	2.03E-03
37	9.52E-03	9.22E-03	2.27E-03	2.16E-03
38	1.01E-02	9.95E-03	2.38E-03	2.29E-03
39	1.02E-02	1.04E-02	2.82E-03	2.83E-03
40	1.24E-02	1.26E-02	3.97E-03	4.11E-03
41	1.13E-02	1.19E-02	4.80E-03	4.90E-03
42	1.24E-02	1.26E-02	5.14E-03	5.27E-03
43	1.24E-02	1.27E-02	5.26E-03	5.31E-03
44	1.15E-02	1.18E-02	5.00E-03	5.06E-03
45	9.82E-03	9.99E-03	4.32E-03	4.26E-03
46	7.38E-03	7.56E-03	3.19E-03	3.21E-03
47	6.42E-03	6.52E-03	2.52E-03	2.49E-03
48	6.45E-03	6.48E-03	2.54E-03	2.48E-03
49	6.74E-03	6.82E-03	2.59E-03	2.54E-03
50	6.54E-03	6.59E-03	2.48E-03	2.49E-03
51	6.24E-03	6.16E-03	2.16E-03	2.19E-03
52	7.62E-03	7.76E-03	2.24E-03	2.26E-03
53	8.36E-03	8.58E-03	2.22E-03	2.27E-03
54	9.47E-03	9.69E-03	2.20E-03	2.26E-03
55	9.94E-03	1.04E-02	2.14E-03	2.25E-03
56	1.13E-02	1.13E-02	2.11E-03	2.20E-03
57	1.24E-02	1.29E-02	2.09E-03	2.15E-03
58	1.09E-02	1.14E-02	2.04E-03	2.12E-03
59	1.05E-02	1.09E-02	2.02E-03	2.07E-03
60	1.12E-02	1.17E-02	1.93E-03	2.01E-03
61	1.09E-02	1.12E-02	1.90E-03	1.96E-03
62	1.06E-02	1.08E-02	1.81E-03	1.89E-03
63	9.91E-03	1.02E-02	1.79E-03	1.84E-03
64	9.34E-03	9.34E-03	1.76E-03	1.76E-03
65	8.64E-03	8.71E-03	1.73E-03	1.72E-03
66	7.94E-03	7.89E-03	1.69E-03	1.68E-03
67	7.20E-03	7.19E-03	1.67E-03	1.64E-03
68	8.58E-03	8.56E-03	1.77E-03	1.83E-03
69	7.26E-03	7.32E-03	1.64E-03	1.67E-03
70	8.24E-03	1.36E-02	1.79E-03	1.81E-03
71	7.65E-03	7.47E-03	1.75E-03	1.84E-03

continued on next page

continued from previous page

	PCXMC effective dose (mSv)	Prog effective dose (mSv)	PCXMC effective dose (mSv)	Prog effective dose (mSv)
72	7.42E-03	7.32E-03	1.82E-03	1.88E-03
73	7.42E-03	7.48E-03	1.81E-03	2.01E-03
74	7.54E-03	7.54E-03	1.83E-03	2.07E-03
75	7.53E-03	7.56E-03	1.87E-03	1.98E-03
76	7.54E-03	7.92E-03	1.98E-03	1.99E-03
77	7.90E-03	8.20E-03	2.20E-03	2.09E-03
78	9.04E-03	1.04E-02	2.64E-03	2.52E-03
79	1.14E-02	1.35E-02	2.93E-03	2.64E-03
80	1.34E-02	1.42E-02	2.51E-03	2.68E-03
81	1.05E-02	1.14E-02	2.12E-03	2.19E-03
82	7.72E-03	7.95E-03	1.72E-03	1.73E-03
83	7.49E-03	7.42E-03	1.54E-03	1.55E-03
84	8.67E-03	8.97E-03	1.54E-03	1.46E-03
85	8.77E-03	8.81E-03	1.43E-03	1.32E-03
86	8.66E-03	8.65E-03	1.53E-03	1.37E-03
87	8.57E-03	8.53E-03	1.42E-03	1.34E-03
88	8.40E-03	8.06E-03	1.48E-03	1.27E-03
89	8.14E-03	7.86E-03	1.39E-03	1.14E-03
90	6.36E-03	6.11E-03	1.31E-03	1.05E-03
91	5.37E-03	5.03E-03	1.14E-03	9.84E-04
92	5.18E-03	5.19E-03	1.00E-03	9.61E-04
93	5.51E-03	5.43E-03	1.00E-03	1.02E-03
94	6.61E-03	6.59E-03	1.09E-03	9.96E-04
95	1.74E-02	1.73E-02	1.15E-03	1.10E-03
96	3.09E-02	3.17E-02	1.45E-03	1.47E-03
97	3.47E-02	3.55E-02	1.53E-03	1.55E-03
98	2.64E-02	2.74E-02	1.25E-03	1.31E-03
99	9.28E-03	9.93E-03	8.03E-04	7.92E-04
100	3.06E-03	2.94E-03	5.46E-04	4.47E-04
101	2.50E-03	2.33E-03	5.77E-04	4.16E-04
102	2.10E-03	1.92E-03	4.96E-04	3.51E-04
103	1.79E-03	1.66E-03	4.77E-04	2.93E-04
104	1.51E-03	1.32E-03	4.32E-04	2.70E-04
105	1.39E-03	1.20E-03	3.57E-04	2.52E-04
106	1.17E-03	9.32E-04	3.54E-04	2.35E-04
107	1.03E-03	8.01E-04	3.11E-04	1.98E-04
108	8.49E-04	6.55E-04	2.85E-04	1.61E-04
109	7.31E-04	5.58E-04	2.59E-04	1.54E-04
110	7.01E-04	5.25E-04	2.36E-04	1.35E-04
111	6.48E-04	4.32E-04	2.14E-04	1.48E-04
112	5.82E-04	3.99E-04	2.19E-04	1.39E-04
113	5.52E-04	3.40E-04	2.12E-04	1.19E-04
114	5.16E-04	3.16E-04	2.18E-04	1.17E-04
115	4.81E-04	3.08E-04	1.93E-04	1.16E-04
116	4.45E-04	2.78E-04	1.78E-04	1.07E-04
117	4.20E-04	2.69E-04	1.72E-04	9.45E-05
118	4.13E-04	2.27E-04	1.67E-04	8.73E-05
119	3.85E-04	2.26E-04	1.64E-04	9.14E-05
120	3.61E-04	2.16E-04	1.61E-04	8.46E-05
121	3.50E-04	2.04E-04	1.61E-04	8.38E-05
122	3.39E-04	2.04E-04	1.62E-04	8.81E-05
123	3.35E-04	1.80E-04	1.60E-04	9.37E-05
124	3.42E-04	1.85E-04	1.55E-04	8.82E-05
125	3.29E-04	1.83E-04	1.51E-04	8.69E-05

continued on next page

continued from previous page

	PCXMC effective dose (mSv)	Prog effective dose (mSv)	PCXMC effective dose (mSv)	Prog effective dose (mSv)
126	3.16E-04	1.76E-04	1.48E-04	8.02E-05
127	3.08E-04	1.69E-04	1.43E-04	7.76E-05
128	2.94E-04	1.62E-04	1.41E-04	7.83E-05
129	2.97E-04	1.58E-04	1.38E-04	7.29E-05
130	2.91E-04	1.52E-04	1.36E-04	7.25E-05
131	2.83E-04	1.47E-04	1.32E-04	7.14E-05
132	2.79E-04	1.45E-04	1.30E-04	7.09E-05
133	2.70E-04	1.42E-04	1.27E-04	7.02E-05
134	2.65E-04	1.41E-04	1.25E-04	6.98E-05
135	2.55E-04	1.40E-04	1.22E-04	6.85E-05
136	2.53E-04	1.38E-04	1.21E-04	6.75E-05
137	2.45E-04	1.35E-04	1.18E-04	6.69E-05
138	2.41E-04	1.34E-04	1.15E-04	6.56E-05
139	2.28E-04	1.31E-04	1.13E-04	6.43E-05
140	2.22E-04	1.29E-04	1.11E-04	6.39E-05
141	2.16E-04	1.24E-04	1.10E-04	6.30E-05
142	2.09E-04	1.22E-04	1.06E-04	6.20E-05
143	2.04E-04	1.20E-04	1.04E-04	6.12E-05
144	1.96E-04	1.18E-04	1.02E-04	5.99E-05
145	1.90E-04	1.15E-04	1.00E-04	5.85E-05
146	1.85E-04	1.13E-04	9.70E-05	5.79E-05
147	1.82E-04	1.11E-04	9.50E-05	5.77E-05
148	1.75E-04	1.08E-04	9.20E-05	5.61E-05
149	1.69E-04	1.05E-04	8.90E-05	5.49E-05
150	1.65E-04	1.03E-04	8.80E-05	5.42E-05
151	1.60E-04	1.00E-04	8.60E-05	5.37E-05
152	1.53E-04	9.73E-05	8.40E-05	5.26E-05
153	1.48E-04	9.51E-05	8.00E-05	5.16E-05
154	1.43E-04	9.25E-05	7.80E-05	5.07E-05
155	1.38E-04	9.08E-05	7.60E-05	4.97E-05
156	1.34E-04	8.83E-05	7.40E-05	4.88E-05
157	1.30E-04	8.53E-05	7.20E-05	4.75E-05
158	1.24E-04	8.33E-05	6.90E-05	4.69E-05
159	1.19E-04	8.01E-05	6.70E-05	4.54E-05
160	1.14E-04	7.82E-05	6.50E-05	4.43E-05
161	1.10E-04	7.62E-05	6.20E-05	4.32E-05
162	1.04E-04	7.34E-05	6.00E-05	4.24E-05
163	9.90E-05	7.04E-05	5.80E-05	4.06E-05
164	9.50E-05	6.84E-05	5.60E-05	3.96E-05
165	9.10E-05	6.50E-05	5.40E-05	3.85E-05
166	8.60E-05	6.28E-05	5.20E-05	3.77E-05
167	8.20E-05	6.01E-05	5.00E-05	3.61E-05
168	7.70E-05	5.79E-05	4.70E-05	3.49E-05
169	7.30E-05	5.56E-05	4.50E-05	3.42E-05
170	6.80E-05	5.28E-05	4.30E-05	3.31E-05
171	6.40E-05	5.05E-05	4.10E-05	3.18E-05
172	5.90E-05	4.75E-05	3.80E-05	3.06E-05
173	5.50E-05	4.48E-05	3.50E-05	2.84E-05
174	5.30E-05	4.69E-05	3.50E-05	3.05E-05

D

Code explanation

D.1 Files

This programme is built in Matlab and, therefore, the programme files have the extension *.m*. The files that make up the dose prediction programme are listed below along with their function.

Predic.m
The main programme file; all other files are called by this file. The technique factors and patient dimensions are input into this file and run to generate the doses.

spectrum.m
This file generates the energy spectrum of the beam from the inputted technique factors using the Boone and Seibert (1997) TASMIP model (see Section 2.3.1.3).

aln.txt
This file contains the mass attenuation coefficients $(\frac{\mu}{\rho})$ of aluminium used to simulate the attenuation of the beam through the filter in *spectrum.m* (see Equation 6.2). These coefficients are available from NIST (2008). The units of $(\frac{\mu}{\rho})$ used in this file are cm^2/g. Other filters besides Aluminium could be simulated by changing these coefficients to the $\frac{\mu}{\rho}$ of the material of interest.

coffs.dat
This file contains the coefficients used in the Boone and Seibert (1997) TASMIP

model to generate X-ray spectra in *spectrum.m* (see Equation 2.16). These coefficients published by Boone and Seibert (1997) are available from the ftp site *ftp://ftp.aip.org/epaps/medical_phys/E-MPHYA-24-1661/*.

HVL.m and *HVL2.m*
These files contain two methods of calculating the half value layer of the beam in terms of exposure.

boone.m
This file is used to calculate the ratio between the energy imparted for a standard sized patient and the patient of interest from the patient thicknesses of a particular increment (see Section 6.2.1.2).

dose_a.m
This file calculates the entrance dose (free-in-air) using *method 1* (see Section 6.1).

dose_b.m
This file calculates the entrance dose (free-in-air) using *method 2* (see Section 6.1).

effer.m
This file calculates the effective dose for the standard sized patient at the current increment on the body (see Section 6.2.1.4). It uses the technique factors, the generated spectrum, and the position and orientation of the scan.

mass.mat
This file contains the organ masses used in by the file *effer.m* (see Table 6.1). When loaded, this file generates the variable *masses*.

OOORRR3.mat
This files contains the database of organ absorption coefficients ($\theta_{organ}(\varepsilon, P)$) for AP and lateral examinations in increments of 1cm used by *effer.m* (see Section 6.2.1.4). When loaded, this file generates the variables *Organ_En* for AP and *Organ_En_Lat* for lateral which are 3 dimensional arrays of dimension $23 \times 16 \times 174$ denoting 23 organs, 16 photon energy levels and 174 increments.

plot_out.m
This file plots the relevant graphs and data.

There are two versions of this code. The first version is designed for standard examinations and the second version is designed to work with ATFC examinations. These two programmes can be combined at a later stage. The differences in the programmes are due to different inputs being sent for each iteration and different outputs displayed, and are found in the main file of each programme, *Predic.m*. All the subfiles are identical.

D.2 Running the programme

The current version of this programme does not have a user interface. The scan orientation, scan position, technique factors (tube voltage, tube current, scan speed, source to skin distance, collimator width, filter thickness), patient dimensions (mass and height) are input where the term *MODIFY* appears in the code in the file *Predic.m*. The scan position is input in terms of 1cm iterations where the top of the head is 1 and the bottom of the foot is 174. For example, a typical abdomen examination is selected by making the *sstep* variable equal to "59:96". Figure D.1 shows the position of each iteration accross the body. The file *Predic.m* is then run in *Matlab* to obtain the dose results.

Figure D.1: The position of each increment and positions of common landmarks